

**Enhancing Image Resolvability in Obscured Environments Using 3D Deconvolution and a Plenoptic Camera**

by

Jeffrey Thomas Bolan

A thesis submitted to the Graduate Faculty of  
Auburn University  
in partial fulfillment of the  
requirements for the Degree of  
Master of Science

Auburn, Alabama  
May 10, 2015

Keywords: Plenoptic, Light field, Flame imaging, 3D Deconvolution, Occlusions, SFR

Copyright 2015 by Jeffrey Thomas Bolan

Approved by

Brian S. Thurow, Chair, Associate Professor of Aerospace Engineering  
Stanley J. Reeves, Professor of Electrical Engineering  
Roy J. Hartfield, Professor of Aerospace Engineering

## **Abstract**

Light field imaging with a plenoptic camera is an emerging flow diagnostic technique capable of capturing three dimensional information about a given volume or flow from a single plenoptic image. Translucent occlusions such as flames often partially obscure and degrade features of interest in many imaging environments. The plenoptic camera is a promising tool for investigating such flows, yet its application to imaging in partially occluded environments or imaging flames is largely unexplored. This thesis explores this application by first explaining the fundamentals of light field imaging with a plenoptic camera. The focus then shifts to imaging in environments containing translucent occlusions. Tests to characterize the general performance of the plenoptic refocusing algorithm were conducted. Separate experiments were performed to quantify the improvements from the enhancement technique of 3D deconvolution. Qualitative examples of the deconvolution algorithm as applied to various types of flames are shared with direction towards future work.

## **Acknowledgments**

The author would like to thank his family and friends for their constant encouragement over the past six years here at Auburn University. The author would also like to thank his advisor, Dr. Brian Thurow, for providing a very meaningful two years of graduate study and research and especially for always being willing to talk through the myriad questions that inevitably come up during research. The author would like to also thank Dr. Stanley Reeves and Dr. Roy Hartfield for serving as committee members and for teaching engaging graduate school classes. The author would like to thank the entire Advanced Flow Diagnostics Lab group for their friendship and support, as well as for their helpful attitudes. Specifically, the author would like to thank Kyle Johnson for his extensive assistance over the past two years in helping program the Light Field Imaging Toolkit, setting up countless experiments, and his general aid with this research. The author would also like to thank Paul Anglin for the MATLAB implementation of the deconvolution algorithm used in this work and for the discussions regarding various challenges in applying the technique. The author would like to thank the United States Department of Defense for their provision of the Science, Mathematics, And Research for Transformation Scholarship. The author would also like to thank his church families at First Baptist Church of Meridianville and First Baptist Church of Opelika for their friendship, support, and prayers. Finally, the author would like to thank the Lord and Savior, Jesus Christ, for His marvelous, infinite, matchless grace. To God be the glory!

## Table of Contents

I.	Introduction and Background .....	1
II.	Light Field Imaging .....	7
A.	The Light Field .....	7
B.	Plenoptic Camera Fundamentals.....	8
C.	Prototype Plenoptic Camera .....	11
D.	Typical Experimental Procedure.....	13
III.	The Light Field Imaging Toolkit .....	20
A.	Introduction.....	20
B.	Initial Steps .....	20
C.	Calibration.....	21
D.	Interpolation of Microimage Data .....	22
E.	Formation of 4D Radiance Array .....	25
1.	Radiance Array.....	25
2.	Coordinate System Definitions .....	25
F.	Graphic User Interface.....	27
G.	Perspective Shifts.....	28
H.	Refocusing .....	31
1.	Overview .....	31
2.	Alpha Scaling in Refocusing Equation .....	33

3.	Pixels to Millimeters Scaling on the Aperture Plane .....	39
4.	Further Discussion and Demonstration .....	40
I.	PIV Processing.....	41
IV.	Resolving Depth Information .....	44
A.	Computational Refocusing.....	44
B.	Deconvolution.....	50
1.	Introduction .....	50
1.	Two-Dimensional Deconvolution Techniques.....	51
2.	Three-Dimensional Deconvolution Techniques.....	52
3.	Point Spread Function .....	55
V.	Characterizing Refocusing Performance.....	59
A.	Motivation.....	59
B.	Spatial Frequency Response as a Resolution Metric .....	59
C.	Experimental Arrangement.....	62
1.	Overview and Procedure .....	62
2.	Target Selection.....	65
D.	Results.....	70
1.	Processing Procedure .....	70
2.	Selected Plots and Discussion .....	71
3.	Nyquist and Supersampling Effects .....	81
VI.	Occlusion Testing .....	86

A.	Introduction.....	86
B.	Experimental Arrangement.....	86
C.	Quantitative Approach.....	89
1.	Inadequacy of Slanted Edge Method .....	89
2.	Root Mean Square Error Metric.....	91
D.	Results.....	91
VII.	Example Deconvolution Results as Applied to Flames.....	99
A.	Introduction.....	99
B.	Torch and Bunsen Burner Experiment .....	99
C.	Flame Sheet and USAF Target .....	101
D.	Target Plate and Bunsen Burner .....	102
1.	Description and Results.....	102
2.	Influence of Number of Slices on Deconvolution Quality.....	104
E.	Other Qualitative Results.....	108
VIII.	Conclusions and Future Work .....	110
	References.....	114
	Appendices.....	119
A.	Derivation of Aperture Matching Relationship .....	119
B.	Effect of Averaging on Calibration Images .....	122
C.	Circular Aperture and (u,v) Supersampling Effects on (s,t) Sampling Grids .....	125
D.	Further Supersampling Discussion and Examples.....	127

## List of Tables

Table 1: Single calibration image versus averaged calibration image.....	122
--	-----

## List of Figures

Figure 1: The two plane parameterization for a 4D light field .....	7
Figure 2: Simplified diagram of imaging with a conventional camera (not to scale).....	8
Figure 3: Simplified diagram of imaging with a plenoptic camera (not to scale) .....	9
Figure 4: Two plane parameterization of the light field inside a plenoptic camera (not to scale)	11
Figure 5: Imperx Bobcat ICL-B4820 CCD image sensor (left), microlens mount and array (center), and assembled camera body (right).....	12
Figure 6: Microlens array alignment procedure.....	14
Figure 7: Sample scene for experimental procedure demonstration.....	15
Figure 8: Raw plenoptic image from sample experiment (scaled down) with zoomed inset .....	16
Figure 9: Effect of aperture setting on microimage size (left: too large, center: correct, right: too small).....	17
Figure 10: Cropped portion of an averaged calibration image .....	19
Figure 11: LFIT pre-processing GUI window .....	21
Figure 12: Known (u,v) coordinates and desired uniform (u,v) coordinates for microimage interpolation .....	22
Figure 13: Comparison of known microlens centers with assumed (s,t) grid .....	24
Figure 14: Coordinate system definitions for a given microimage.....	26
Figure 15: Coordinate system definitions for the raw image.....	27
Figure 16: LFIT graphic user interface for image generation.....	28
Figure 17: Simplified diagram of perspective view generation.....	29



Figure 18: Two example perspective views of the sample lab scene with reference line .....	30
Figure 19: Schematic depicting process of computational refocusing .....	32
Figure 20: Direct implementation of refocusing equation with far focus $\alpha = 0.75$ (left) and close focus $\alpha = 1.55$ (right) .....	34
Figure 21: Diagram of image formation process when computationally refocusing.....	34
Figure 22: Direct implementation sampling grid for (s,t) coordinates in computational refocusing at $\alpha = 0.75$ .....	35
Figure 23: Direct implementation sampling grid for (s,t) coordinates in computational refocusing at $\alpha = 1.55$ .....	36
Figure 24: Modified implementation of refocusing equation with far focus $\alpha = 0.75$ (left) and close focus $\alpha = 1.55$ (right).....	37
Figure 25: Shift-invariant sampling grids used in computational refocusing for alpha = 0.75 (left) and 1.55 (right).....	38
Figure 26: Pixels to millimeters scaling on the (u,v) aperture plane .....	39
Figure 27: Sample refocused image at alpha = 0.95 (left) and alpha = 1.06 (right).....	41
Figure 28: Example of plenoptic PIV behind a hemisphere .....	43
Figure 29: Variation of alpha with focal plane depth for varying magnifications.....	46
Figure 30: Depth of field variation with magnification for different f-numbers .....	48
Figure 31: Representative (stopped-down) aperture diagram and resulting image with wide DOF .....	49
Figure 32: Representative (full) aperture diagram and resulting image with narrow DOF.....	49
Figure 33: Vertical cross section of real 3D PSF for a magnification of 0.375.....	57
Figure 34: Intensity profile of PSF with respect to depth.....	58

Figure 35: Experimental setup for refocus performance testing.....	63
Figure 36: Plot of refocusing performance experiment data capture points.....	64
Figure 37: Slanted edge selection reference image for case 1, magnification of 0.250 .....	67
Figure 38: Slanted edge selection reference image for case 2, magnification of 0.375 .....	68
Figure 39: Slanted edge selection reference image for case 3, magnification of 0.500 .....	69
Figure 40: Slanted edge selection reference image for case 4, magnification of 1.000 .....	70
Figure 41: Curve-fitted variation of SFR with target position at a magnification of 0.500 .....	72
Figure 42: Edge and SFR comparison at magnification = 0.500 and multiple positions .....	73
Figure 43: Curve-fitted variation of SFR with target position at a magnification of 0.250 .....	74
Figure 44: Curve-fitted variation of SFR with target position at a magnification of 0.375 .....	75
Figure 45: Curve-fitted variation of SFR with target position at a magnification of 1.000 .....	76
Figure 46: SFR for DOF x -03 and magnification = 1.000 with Gaussian curve fit .....	77
Figure 47: SFR for DOF x 01 and magnification = 1.000 with Gaussian curve fit.....	78
Figure 48: SFR50 as a function of magnification for refocus testing.....	79
Figure 49: Non-supersampled edge with corresponding SFR at magnification of 0.500 and target at -1 DOF .....	83
Figure 50: Supersampled 4x (s,t) edge with corresponding SFR at magnification of 0.500 and target at -1 DOF .....	84
Figure 51: Experimental setup for occlusion testing .....	87
Figure 52: Root mean square error between occluded refocused images and clean reference images .....	92
Figure 53: Qualitative results for magnification 0.250 case occlusion testing .....	93

Figure 54: Root mean square error between occluded deconvolved images and clean reference images .....	95
Figure 55: Percent change between the RMSE results for deconvolution and refocusing .....	96
Figure 56: Qualitative comparison of deconvolved results with refocusing results at a magnification of 1.000 .....	97
Figure 57: Experimental setup for torch and Bunsen burner testing .....	99
Figure 58: Example flame and torch image comparing deconvolution to refocusing alone .....	100
Figure 59: Experimental setup for target occluded by flame sheet .....	101
Figure 60: Example flame sheet obscuring a target for comparing deconvolution to refocusing alone .....	101
Figure 61: Flame obscuring 1951 USAF target experimental setup .....	103
Figure 62: Bunsen burner and USAF target refocusing and deconvolution slice comparison ...	104
Figure 63: Comparison of (low) number of slices on deconvolved quality .....	106
Figure 64: Comparison of (high) number of slices on deconvolved quality .....	107
Figure 65: Several examples of (non-occluded) flames comparing refocusing and deconvolution .....	108
Figure 66: Geometric relationships in the plenoptic camera to permit f-number matching .....	120
Figure 67: Surface plot of calibrated microlens X position error in pixels .....	123
Figure 68: Surface plot of calibrated microlens Y position error in pixels .....	123
Figure 69: Effect of enforcing a circular aperture on (s,t) sampling grid used in refocusing .....	125
Figure 70: Sampling grid for (s,t) with supersampling x2 (left) and x4 (right) in (u,v) with an enforced circular aperture .....	126
Figure 71: Sample refocused lab scene of clock (without supersampling) .....	127

Figure 72: Supersampling and upscaling qualitative comparison ..... 128

## List of Symbols

<i>1D</i>	one dimensional
<i>2D</i>	two dimensional
<i>3D</i>	three dimensional
<i>4D</i>	four dimensional
<i>5D</i>	five dimensional
<i>A</i>	main lens aperture diameter
<i>AFDL</i>	Advanced Flow Diagnostics Laboratory
<i>ALFA</i>	Auburn Light Field Analyzer
<i>CCD</i>	charge coupled device
<i>D</i>	diameter of aperture
<i>DOF</i>	depth of field
<i>e-SFR</i>	edge-based spatial frequency response
<i>f</i>	blurred/real image(s)
<i>f<sub>main lens</sub></i>	focal length of main lens
<i>FFT</i>	fast Fourier transform
<i>FOV</i>	field of view
<i>g</i>	hypothetical in focus image(s)
<i>GUI</i>	graphic user interface
<i>h</i>	point spread function
<i>ISO</i>	International Organization for Standardization

$K$	regularization parameter
$LIF$	laser induced fluorescence
$LFIT$	Light Field Imaging Toolkit
$LFM$	light field microscopy
$M$	magnification
$M$	image width (pixels) in context of RMSE
$MART$	multiplicative algebraic reconstruction algorithm
$mm$	millimeters
$MP$	megapixel
$MTF$	modulation transfer function
$mW$	milliwatts
$N$	f-number
$N$	image height (pixels) in context of RMSE
$N_{ideal}$	ideal main lens f-number for maximum microimage size
$N_{microlens}$	f-number of the microlenses
$nm$	nanometers
$P$	number of pixels across each microlens
$PIV$	particle image velocimetry
$PSF$	point spread function
$RMSE$	root mean square error
$ROI$	region of interest
$s'$	synthetic sensor (film) plane
$s_i$	image distance

$s_i'$	new image distance
$s_o$	object distance
$s_o'$	new object distance
$s\text{-}SFR$	sine-based spatial frequency response
$SFR$	spatial frequency response
$SFR50$	frequency at which the SFR drops to a 0.5 response
$TIFF$	Tagged Image File Format
$USAF$	United States Air Force
$\alpha$	refocusing factor
$\delta$	sampling rate of the imaging system
$\eta$	noise term
$\omega$	frequency

## I. Introduction and Background

TRADITIONAL flow diagnostic techniques can be difficult to apply to chemically reacting flows. Limited optical access, typically high heat, and three-dimensional (3D) flow structures all conspire to make analysis of reacting flows a challenging endeavor. These types of flows are of great importance to not only the aerospace community but other disciplines as well. Whether it is improving the combustion efficiency of an engine or investigating the performance of an industrial furnace, understanding and characterizing reacting flow structures is a vital area of research in many fields.

Generalizing the problem, imaging in chemically reacting flow environments can often be described as imaging through a series of translucent occlusions. These translucent occlusions, as their name suggests, may be flames, fog, or other non-opaque structures that partially degrade and obscure attempts to image features of interest in a volume. A translucent occlusion such as smoke, fog, or large smooth flames will be largely uniform in appearance and cause an overall contrast reduction in captured images. In a more chaotic flow environment, flames or other chemically reacting flows may be highly unsteady and create many edges and visible flow structures in output images. If the translucent occlusion is uniform, the goal may be to image some target of interest behind the smooth occlusion. In the second case with spatially varying structures visible in the flow, the target could be the flames themselves. Both of these types of translucent occlusions can complicate efforts to image in chemically reacting flow environments.

The unsteady and 3D nature of many of these flows necessitates the use of 3D techniques to fully capture the flow behavior. However, many 3D flow diagnostics are ill-suited for many flame or combustion environments due to practical considerations like limited optical access. Many methods have been developed to characterize such flows, including one-dimensional (1D),



two-dimensional (2D), and 3D techniques. Reflecting the breadth of the field of optical flame diagnostics, these various techniques are often designed to measure different quantities in the flow: velocities, concentrations, or general flow structure development. Focusing on the 3D techniques, several possible methods emerge.

Particle image velocimetry (PIV) methods are commonly used for flow field determination. By measuring particle displacements in a seeded flow, PIV allows computation of instantaneous velocity vectors across the imaged flow [1]. The technique of PIV is well-established in 2D flows and has been successfully extended to 3D flows as well [2]. The most basic extension to PIV is known as stereoscopic PIV, which uses a two camera arrangement to measure depth-wise displacements. However stereoscopic PIV is not a full 3D technique as the 3D velocity data it obtains is limited to a narrow 2D measurement plane. Tomographic PIV improves upon stereoscopic PIV by obtaining 3D velocity data throughout a 3D volume. This is done by adding additional cameras to form an array, with each camera imaging the same volume from different angles. These additional cameras, while effective at obtaining a true 3D measurement, increase the optical access requirements.

Laser induced fluorescence (LIF) is a laser-based diagnostic technique used to excite chemical species in a flow to determine species concentrations. Additional flow parameters have been measured via LIF, including temperature, pressure, and velocity [3]. LIF has been extended to 3D to measure the 3D concentration field [4] and the 3D velocity field [5]. These 3D LIF techniques rely on scanning mirrors to rapidly scan the laser illumination through the volume. The scan must be of sufficient speed relative to the flow, otherwise the flow may evolve a meaningful amount during the scanning process.

A relatively new 3D diagnostic technique to emerge is light field imaging with a plenoptic camera. This technique uses a plenoptic camera to capture the light field—the spatial and angular information associated with the distribution of light rays in a volume [6]. A plenoptic camera is identical in most respects to a conventional camera; the key difference lies in the addition of a microlens array. This planar array of microlenses is inserted inside the camera a short distance in front of the image sensor. As light rays enter the main lens of the camera, they are focused onto the microlens array. Depending on the incident angle of a given light ray on the main lens, the ray will be focused by the microlens it strikes onto a different pixel on the image sensor. In this way, both the angular and spatial information in a scene is sampled. This combined spatial and angular data can be computationally processed to generate new, unique images of the volume from a single raw plenoptic image.

Light field imaging with a plenoptic camera holds several advantages over other 3D flow diagnostic techniques. While other 3D methods often require additional cameras to resolve depth information, this technique only requires a single plenoptic camera to capture 3D measurements of a flow. Other techniques capture depth information via complex optical setups and scanning mirrors; in contrast, the plenoptic camera has no moving parts. Calibration is also simplified as there is no need to align multiple cameras. Despite being a single camera technique, the tightly packed microlens array allows for a dense sampling of the angular information in a scene. The minimal optical access requirements of the plenoptic camera make it uniquely suited for imaging chemically reacting flows. From a single image, the plenoptic camera can capture an instantaneous measurement of a rapidly evolving flow field.

While the technology necessary to facilitate practical implementations of the plenoptic camera is still relatively new, the fundamental concepts undergirding the technique are surprisingly old.

Gabriel Lippmann posited the idea of the light field and a method for capturing it in a paper at the turn of the 20<sup>th</sup> century [7]. With the advent of modern digital imaging, Adelson and Wang were able to describe the plenoptic camera [8] before it was physically realized in a compact form by Ng at Stanford University [9]. Work by Lumsdaine and Georgiev to create the focused plenoptic camera [10] bears mention here as well. Over the past several years, the Auburn University Advanced Flow Diagnostic Laboratory (AFDL) has been exploring various applications of the plenoptic camera. The primary research effort in this area by the AFDL has been towards developing 3D plenoptic PIV techniques [11] [12]. While light field imaging with a plenoptic camera remains a novel technique, it is increasingly being used by other labs and research groups as the tools and technology mature.

All of the above techniques have been used to image flames or other reactive flows in 3D. For example, Weinkauff et al. captured 3D measurements of a seeded jet burner flow via tomographic PIV [13]. Recently Li and Ma used similar tomographic techniques with a camera array to image unseeded turbulent reactive flows via the chemiluminescence of the flames [14]. A 3D LIF technique was used by Cho et al. to capture the combustion of droplets [15].

The continued novelty of the plenoptic camera means that little published research exists regarding imaging in translucent environments or more specifically imaging reactive flows via a plenoptic camera. A paper by Greene and Sick [16] used a commercially available Raytrix plenoptic camera to examine flames emanating from a soldering torch and acetone-seeded nitrogen jets. In contrast to the camera used in this research, Greene and Sick used a focused plenoptic camera in which the measurement of spatial and angular information is interrelated. This complicates the analysis compared to our camera which independently measures the position and angle of light rays. Greene and Sick were able to estimate the depth of the front

surface of the soldering torch flames and nitrogen jets but were unable to reliably identify the rear surface of the flames or jets. Several factors limited their experiment, including a non-monochromatic sensor, small pixel size, and small microlens aperture. It also appears that neither deconvolution nor tomographic techniques were employed. Our plenoptic camera implementation improves upon each of the above limitations. A fellow research group at Auburn recently laid the groundwork for a deconvolution framework with a plenoptic camera from a signal processing perspective [17]. This was extended in a recent conference paper by this author and lab [18].

This thesis has several goals. First, this thesis aims to provide a solid understanding of light field imaging with a plenoptic camera from a practical perspective. A detailed description of the concepts behind light field imaging with a plenoptic camera is given with example images illustrating the versatility of the technique. Secondly, this thesis explores the specific application of the plenoptic camera to imaging in environments containing translucent occlusions or more specifically flames. Many real world imaging scenarios involve translucent occlusions or flames, yet the plenoptic camera's application to this regime is largely unexplored. While the plenoptic camera is fully capable of imaging in such environments unaided, the technique of 3D deconvolution is described as a method for recovering additional detail at distinct depth planes in such a volume. The choice of a point spread function for the deconvolution process is explained. Two sets of experiments were conducted to quantify both the performance of the plenoptic camera and the improvements realized by the deconvolution algorithm. Results from these experiments are presented and discussed. Finally, several qualitative examples of the deconvolution technique as applied to flames are shared to show the power and potential of

imaging these types of flows with the plenoptic camera and deconvolution. Conclusions are drawn and several directions for future work are given.

## II. Light Field Imaging

### A. The Light Field

To understand the technique of light field imaging with a plenoptic camera, it is important to understand what the light field actually is. The light field is a means of describing the distribution of light rays in a volume in terms of their spatial and angular coordinates. While the idea of treating light as a field can be traced as far back as Faraday [6], the light field as discussed here has its roots in Adelson and Bergen's description of the plenoptic function [19]. Their definition of the plenoptic function described how one may parameterize the distribution of light rays in a volume. Levoy and Hanrahan later showed [20] that the five-dimensional (5D) representation of the light field can be reduced to only a four-dimensional (4D) representation by assuming that the intensity (radiance) along a given light ray is constant. It is this representation that is implemented in the processing algorithms for the plenoptic camera used in this paper.

While there a number of ways of representing this 4D function, perhaps the most useful is the two plane parameterization. Adopting the notation commonly used in the literature by Levoy and Ng, a typical representation of the two plane parameterization is given below in Figure 1, modeled after [20].

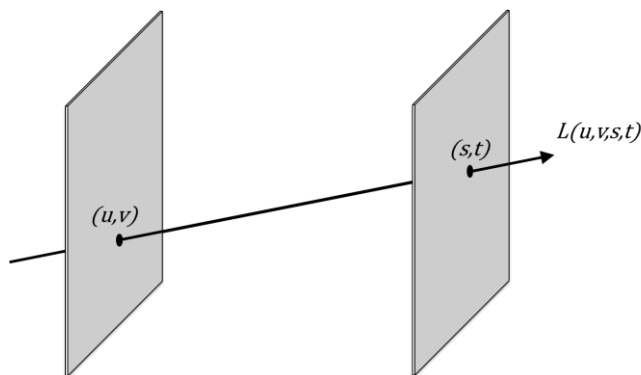
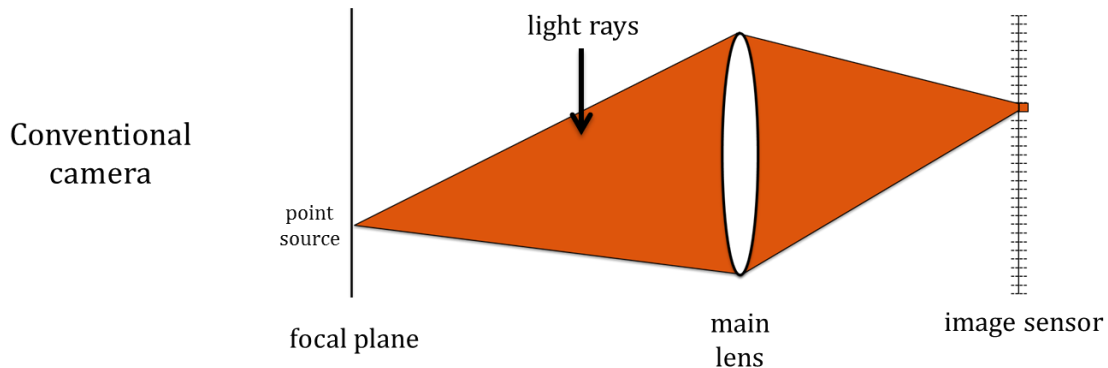


Figure 1: The two plane parameterization for a 4D light field

As seen in the figure, a given ray of light can be described by four dimensional coordinates. A given light ray intersects the first plane at some  $(u, v)$  coordinate location before intersecting the second plane at some  $(s, t)$  coordinate location. The intensity of a given light ray is then given by the 4D function,  $L(u, v, s, t)$ . This notation will prove useful later in the following discussion of the plenoptic camera.

## B. Plenoptic Camera Fundamentals

Put simply, the plenoptic camera is a device capable of sampling a portion of the 4D light fields described above. A single image captured by a plenoptic camera records both spatial and angular information associated with the distribution of light rays in a scene. From a practical perspective, a plenoptic camera is largely similar in both form and function to a conventional camera. The key difference lies in the insertion of an array of microlenses a short distance in front of the image sensor. To understand the implications of this addition, it is helpful to first consider the representative diagram of a conventional camera shown below in Figure 2.



**Figure 2: Simplified diagram of imaging with a conventional camera (not to scale)**

Examining Figure 2, the propagation of light through a simplified model of a conventional camera can be seen. A conventional camera will have an image sensor, a main lens (reduced to a

single element here), and a focal plane located at some nominal depth in the world. Consider a point source of light located at the focal plane of this conventional camera. The light rays from this point source that strike the main lens are shown in orange. Assuming a fully open aperture and ignoring any diffraction effects, all the light rays shown in orange are focused down to a single pixel on the image sensor. This is expected since the point source is located at the focal plane of camera. The image sensor then records the sum of all the light rays striking that pixel in a given time (exposure) before saving the data to a digital image file. This is a simplified representation of how a conventional camera images a scene.

Now consider the case of a plenoptic camera. A representative diagram for a plenoptic camera is given below in Figure 3.

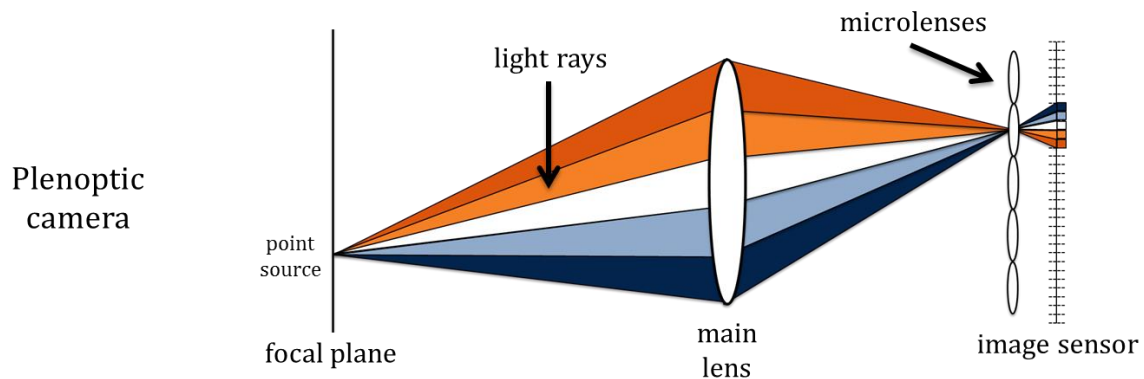


**Figure 3: Simplified diagram of imaging with a plenoptic camera (not to scale)**

For the plenoptic camera, all of the components from the conventional camera are still present. There is still a main lens with a nominal focal plane and an image sensor. Note however that the image sensor was shifted away from the main lens to accommodate the addition of a microlens array. The image sensor now resides at the focal plane of the microlens array.

Consider again the case of a point source located at the focal plane of the main lens. As the light rays enter the main lens of the plenoptic camera, they are focused directly onto the



microlens array. In the figure, the light rays are color coded into groups depending on their incoming angle relative to the optical axis. Recall that for the conventional camera, all the light rays were focused onto a single pixel, regardless of their incident angle on the main lens. However here in the plenoptic camera, depending on what angle a given subset of light rays entered the camera, the light rays are focused onto different pixels on the image sensor.

In this way both the spatial and angular information about light rays in a scene is recorded. The spatial data is recorded by noting which microlens a given light ray strikes. The angular information is recorded by noting which pixel behind a given microlens is illuminated by a light ray. In a conventional camera, the angular data is effectively lost as a given pixel sums the intensity contributions from light rays at many angles. In the plenoptic camera, the addition of the microlens array allows this angular information to be separated and captured.

While the plenoptic camera captures the 4D light field, in practice a plenoptic camera still uses a standard 2D image sensor. The additional dimensional information is essentially encoded into the 2D output image by the positional relationships between groups of pixels in the output image. Returning to the two plane parameterization discussed earlier helps illustrate this concept. As noted by Ng [21], one only needs to consider the light field inside the camera itself, as it is this light field that is actually captured by a plenoptic camera. As far as the plenoptic camera is concerned, the light field of interest begins at the aperture of the main lens inside the camera. To illustrate this, a diagram of the light field inside the plenoptic camera is shown below in Figure 4.

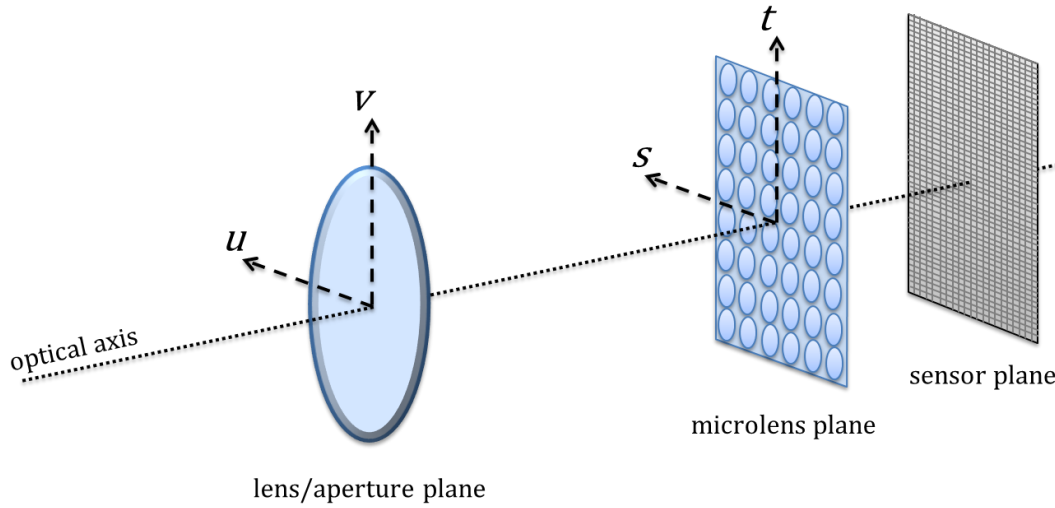


**Figure 4: Two plane parameterization of the light field inside a plenoptic camera (not to scale)**

The key components of the plenoptic camera are shown above with the two plane parameterization of the light field overlaid. The  $(u, v)$  plane coincides with the aperture of the main lens of the camera. The  $(s, t)$  plane coincides with the array of microlenses located in front of the image sensor. Each microlens is actually imaging the aperture of the main lens from its respective point of view inside the camera. The images produced by each microlens are formed on the image sensor and recorded. Each microlens will form a microimage on the image sensor; this microimage will have a specific  $(s, t)$  value associated with it and different  $(u, v)$  values for each pixel. As stated earlier, the geometric relationships between the microlenses will allow a given raw 2D plenoptic image to be processed and structured into a 4D array corresponding to the above parameterization. This will become clearer in the next section when considering a prototype plenoptic camera built in our lab at Auburn University.

### **C. Prototype Plenoptic Camera**

To facilitate the exploration and development of light field imaging techniques, the Auburn University AFDL constructed a prototype plenoptic camera. The prototype camera, used in this

research, is based on a 16 megapixel (MP) Imperx Bobcat ICL-B4820 camera body. The CCD image sensor has square pixels 7.4 microns in size and supports triggered capturing of image pairs as is common in PIV. The monochromatic raw output resolution is 4904 x 3280 with 14-bit grayscale depth. This conventional camera was modified into a plenoptic camera by the addition of a microlens array. A custom mount to hold the microlens array was designed and fabricated in house. The microlens array itself was manufactured by Adaptive Optics Associates, Inc. The array consists of square microlenses in a rectilinear grid, with a microlens pitch of 125 microns. The focal length of the microlenses is 500 microns. The CCD sensor, the microlens array sitting in the mount, and the assembled camera can be seen below in Figure 5.

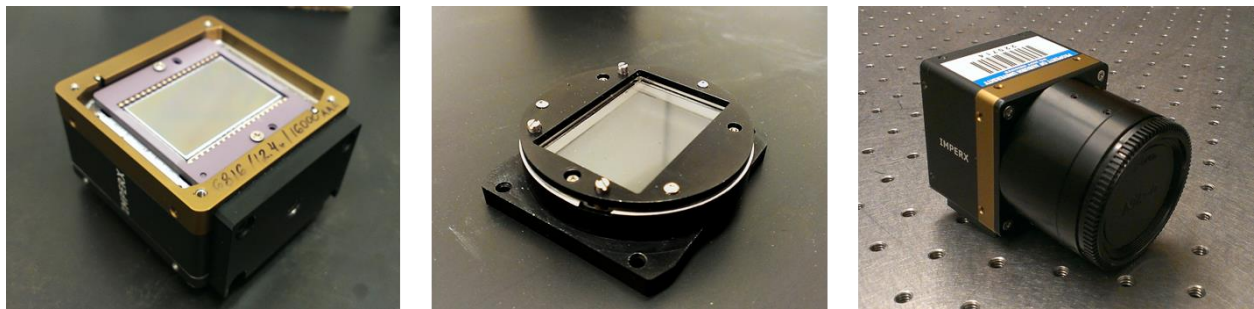


**Figure 5: Imperx Bobcat ICL-B4820 CCD image sensor (left), microlens mount and array (center), and assembled camera body (right)**

The sensor seen above at left has dimensions of 36.1 mm by 24.0 mm. The microlens array mount attaches directly above the image sensor. To ensure that the microlens array is positioned exactly at the focal length of the microlenses, three screws in the mount permit fine adjustments to the positioning of the array. This is achieved via a calibration procedure to be described shortly. The mount itself was anodized black to reduce the possibility of internal reflections.

This particular model of the Imperx Bobcat uses a standard Nikon F-mount for mounting lenses. The F-mount is the black barrel that attaches on top of the custom microlens mount when

the camera is fully assembled, as seen in the right of Figure 5. The F-mount itself has a threaded mechanism by which the distance between the main lens and image sensor can be slightly adjusted. This is necessary to compensate for the change in the optical path length due to the insertion of the glass microlens array.

Because our prototype plenoptic camera is based on a standard 2D CCD image sensor, the image capture procedure is identical to that of any other conventional scientific camera. Either a trigger signal or a software command sent via the standard CameraLink interface is used to capture an image. The key usage differences between conventional and plenoptic cameras are manifested in the post-processing stage to be described. Before discussing the processing of plenoptic images however, it is worthwhile to first consider the capturing procedure itself.

#### **D. Typical Experimental Procedure**

The following discussion describes key steps in the set up and execution of an experiment with a plenoptic camera. The exact parameters corresponding to the specific experiments performed for this paper are to be described later; this section is simply intended to give a general overview of the experimental procedure associated with a plenoptic camera. This discussion will provide context for the post-processing section to follow.

Ideally, the first step in any set of experiments involving a plenoptic camera will be to verify that the microlens array is properly aligned with respect to the image sensor. Earlier it was stated that the microlens array was mounted such that the image sensor is located at the focal plane of the microlenses. While the microlens array mount places the microlens array at approximately the correct distance, in practice the array is typically out of alignment. Additionally, the microlens array itself can become misaligned with respect to the image sensor; that is, rather than the planes being parallel to one another, the microlens plane can become tilted with respect to a

given axis of the image sensor. To address these problems, the microlens array mount was specifically designed to permit fine adjustments to the position of the microlens array inside the mount. The procedure for aligning the microlens array is illustrated below in Figure 6.

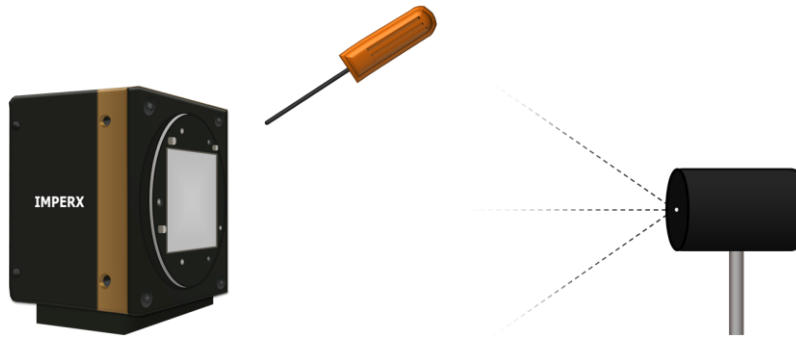


**Figure 6: Microlens array alignment procedure**

A collimated light source, positioned at a distance far from the camera in a dark room, illuminates the microlens array. Three screws in the mount control changes to the position and angle of the microlens array. The camera itself is meanwhile connected to a computer with a live preview of the output displayed. The output from the camera shows the images formed by each microlens of the light source. The screws are adjusted until the images formed by the microlenses are small points. This is an iterative process in practice, as adjustments to one screw will non-uniformly affect the output image; each screw controls the mounted position of one part of the array. This microlens adjustment mechanism used here is identical to the mechanism used by Ng [21]. He observed that an accuracy of 10 microns was achievable in this manual adjustment process. For the prototype camera used by our lab, the accuracy required to correctly focus the microlens array is approximately 60 microns. While this procedure may sound somewhat tedious, after the initial alignment, the array typically moves very little between experiments, speeding up the alignment process. Our lab recently began investigating the

feasibility of locking the microlens array permanently in place using glue after this alignment procedure.

Once the microlens array alignment is verified, the experiment can be set up. The exact configuration will of course depend on the nature of the experiment. To help illustrate the procedure described here, a sample experimental scene in the lab was set up and imaged. This nominal experimental setup is pictured below in Figure 7.



**Figure 7: Sample scene for experimental procedure demonstration**

An appropriate lens is mounted to the camera to yield the desired field-of-view (FOV) of the scene. If conducting PIV or an experiment with a similar requirement for a synchronized laser or other light source, the trigger cable input can be used on the camera. In the above sample setup, a 50mm Nikkor lens was used (with an extension tube to reduce the minimum focus distance).

The live preview functionality of the Imperx software aids in the positioning and focusing of the camera. When looking at this output from a zoomed out view (as on a typical computer

monitor), the image will appear much like a conventional camera image, albeit with some slight aliasing patterns (see Figure 8 below for example). This view is useful when adjusting the physical focus of the camera lens to move the nominal focal plane. When satisfied with the location of the nominal focal plane (and other parameters such as exposure), a plenoptic image or series of images can be captured. The aforementioned CameraLink interface permits triggering of the camera from the attached computer, or an external trigger can be used when configured appropriately. In any case, following the capture of an image, a digital image file is created on the computer.

A raw plenoptic image from the sample experiment is shown below in Figure 8. Note that the original 16 MP image was scaled down to fit on the page. Unless otherwise noted, the intensities of the following images were adjusted for clarity.

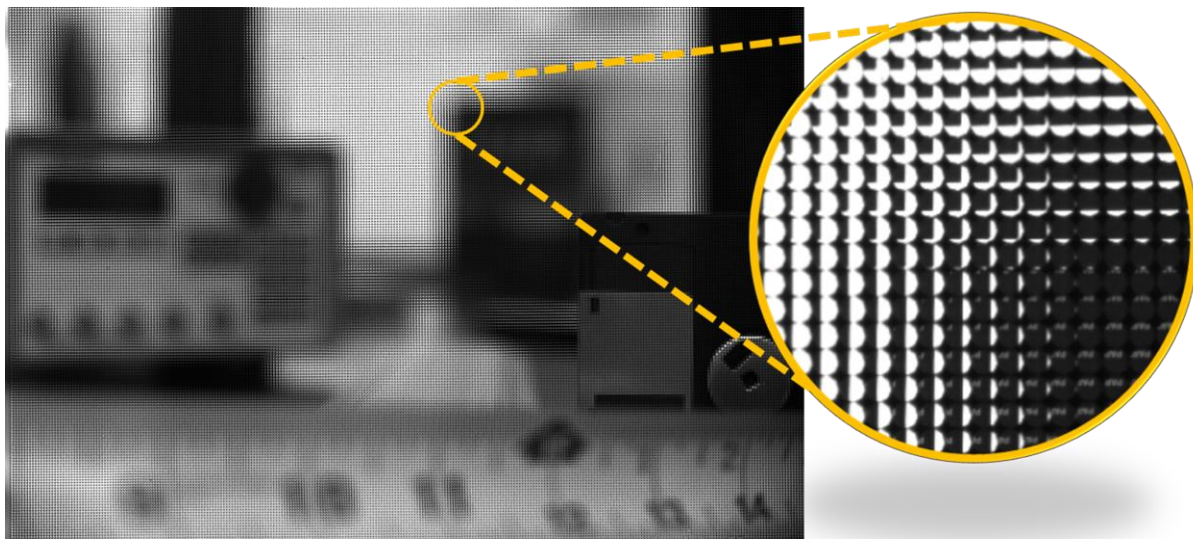


**Figure 8: Raw plenoptic image from sample experiment (scaled down) with zoomed inset**

As seen in the above raw image, the nominal focal plane is on the floppy disk. The other objects in the scene are out of focus to varying degrees. Examining the enlarged inset above reveals that the image is composed of thousands of small microimages formed by each microlens. These

microimages appear circular because each (square) microlens is imaging the circular aperture of the main lens from their respective positions inside the camera body. Virtually all commercially available lenses have a circular aperture. Hypothetically, if one were to construct a lens with a square aperture, the above microimages would be square instead of circular.

Care must be taken to ensure that these microimages are the correct size. Because the microlenses form images of the aperture of the main lens, changing the aperture (f-number) of the main lens will affect the size of the microimages. Three different aperture settings are shown below in Figure 9.

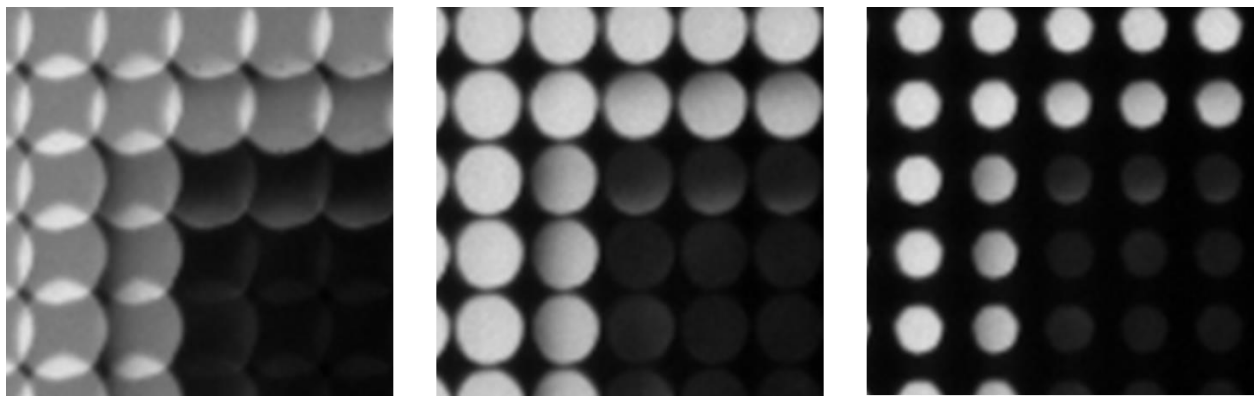


**Figure 9: Effect of aperture setting on microimage size (left: too large, center: correct, right: too small)**

If the aperture of the main lens is too large as in the leftmost image above, the images formed by each microlens will overlap on the image sensor. This leads to ambiguity in the post-processing stage, as it is unclear which recorded intensities correspond to which microlens; the signals are no longer separate. The far right image in the above figure shows the effect of too small of a main lens aperture. A significant portion of the image sensor is not illuminated. This wastes a portion of the active image sensor area while limiting the captured angular data. The center image in Figure 9 shows the ideal aperture size where each microimage is the maximum possible



size without overlap. The ideal aperture f-number  $N_{ideal}$  is given by Eq. (1), where  $M$  is the (positive) magnification:

$$N_{ideal} = \frac{N_{microlens}}{1 + M} \quad (1)$$

A derivation of this relationship is given in Appendix A. For our prototype camera,  $N_{microlens} = 4$ . One of the advantages of imaging with a plenoptic camera is that it uses this maximum useable aperture size when capturing raw images, as the aperture can always be digitally stopped down (reduced) in the post-processing to be discussed. For example, if performing 1:1 imaging with a magnification of 1.000, using our plenoptic camera with f/4 microlenses would require the main lens to have an f/2 aperture setting.

After capturing the desired experimental images, a set of calibration images must be captured. This is necessary for the post-processing stage where the microimages associated with each microlens are extracted and structured. These calibration images record the center of each microlens and thus serve as a necessary reference map for the processing algorithms to be discussed. Without these calibration images, the exact location of each microimage in the scene would be ambiguous.

If the nominal focus of the main lens of the camera is physically adjusted during the experiment, a calibration data set must be captured for every nominal focus position used. The camera and lens are permitted to be moved during an experiment (thus moving the nominal focal plane) without re-calibrating; it is only when physically adjusting the focus ring of the main lens that another calibration is required. Obviously, switching the lens used during an experiment would likewise require its own calibration set.

The actual procedure for capturing a calibration image set is surprisingly straightforward. The aperture of the main lens of the camera is physically stopped down to the minimum value the

lens permits. A solid white object (surface) is placed in front of the main lens of the camera to fill the FOV. No consideration is given to whether or not the white surface is in focus. The exposure may be increased to ensure that the calibration images are sufficiently bright. At least one image is needed of this white surface with a minimum aperture. In practice, approximately one hundred calibration images are captured then averaged together to reduce the influence of noise on the calibration. See Appendix B for a brief justification of this averaging. A cropped portion of an averaged calibration image is given below in Figure 10.

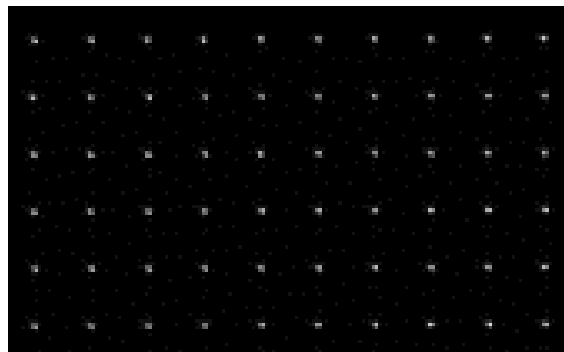


**Figure 10: Cropped portion of an averaged calibration image**

The microimages in Figure 10 no longer appear as large circles but are now spots only a few pixels in diameter. Again, this is due to the microlens array imaging the now tiny circular aperture of the main lens. This calibration image will provide the basis for locating the individual microlens positions in the post-processing, which can now be discussed in detail.

### **III. The Light Field Imaging Toolkit**

#### **A. Introduction**

With the experimental images captured, the raw plenoptic images must now be processed in order to take advantage of the camera's unique capabilities. Whereas in a conventional camera, most post-processing is largely optional, raw plenoptic images require significant post-processing to be of any use. The author of this thesis has served as the lead developer in writing and assembling a collection of functions in MATLAB called the Light Field Imaging Toolkit (LFIT) for the purpose of processing raw plenoptic data.

The development of LFIT began by combining many of the algorithms from a personal light field code written by Kyle Johnson with much of the structure of this author's personal code. Over the past year and a half, LFIT has been improved, fixed, and extended across a number of versions. Today, LFIT is composed of dozens of functions and several thousand lines of code, with a fully functioning graphic user interface (GUI). The plenoptic image processing to be discussed takes place primarily within the context of this tool.

#### **B. Initial Steps**

LFIT first requires that several basic parameters be defined before processing any images. These parameters are defined in the first GUI window, shown below in Figure 11.

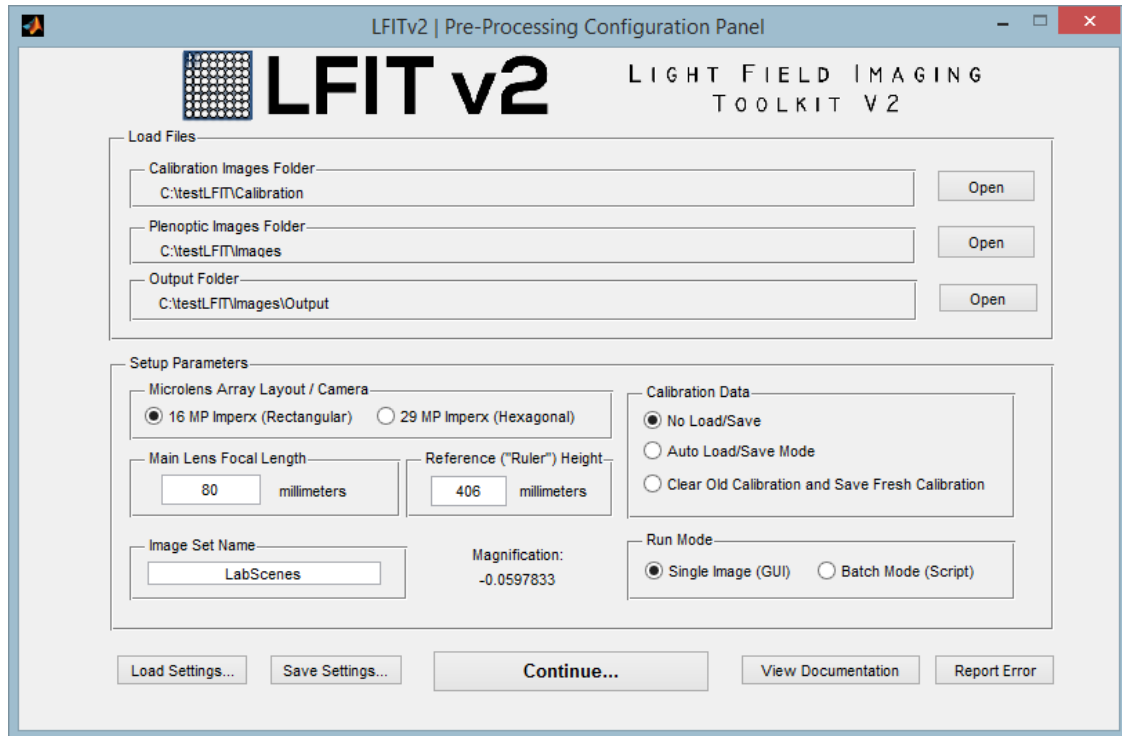


**Figure 11: LFIT pre-processing GUI window**

Specifically, a directory containing calibration image(s) associated with the raw plenoptic image(s) to be processed is defined. The raw plenoptic image directory and output file paths are also specified. The magnification at the nominal focal plane is input by the user, along with the focal length of the main lens. Other parameters such as the focal length of the microlens array are automatically loaded when specifying the plenoptic camera used in the experiment.

### **C. Calibration**

After the above parameter definitions, the first step in post-processing a plenoptic image is the calibration step. LFIT first averages the calibration images in the previously defined directory to reduce the influence of noise on the calibration. Once this averaging process is complete, the user is prompted to identify three calibration points according to a specified pattern. The spatial relationship between these points is used to initiate the primary calibration algorithm. This

algorithm marches through each microimage in the scene, identifying the centroid of each spot (as in Figure 10). These centroids define the centers of each microlens.

#### D. Interpolation of Microimage Data

With the calibration complete, the next step is to interpolate the data behind each microlens onto a uniform  $(u, v)$  grid. Recall that each microlens is imaging the aperture of the main lens. Therefore, the images formed by each microlens will have  $(u, v)$  coordinates associated with each pixel therein. The pixels in each microimage constitute an angular sampling while each microimage itself corresponds to a spatial sample.

It is important to perform this interpolation onto a uniform  $(u, v)$  grid because the microlens array is not perfectly aligned with the image sensor. From an algorithmic perspective, it is computationally more efficient to have the sampled  $(u, v)$  data lie on a uniform grid. Otherwise, it would be later necessary to perform scattered data interpolation, a comparatively slow process. Below in Figure 12, known  $(u, v)$  coordinates are overlaid with the desired uniform grid for a single microimage.

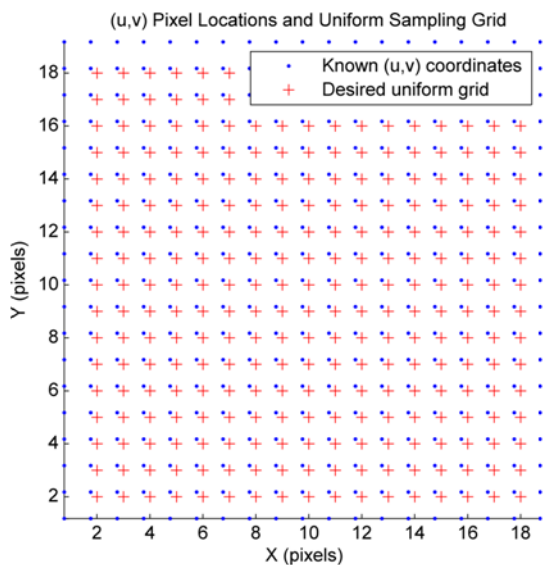
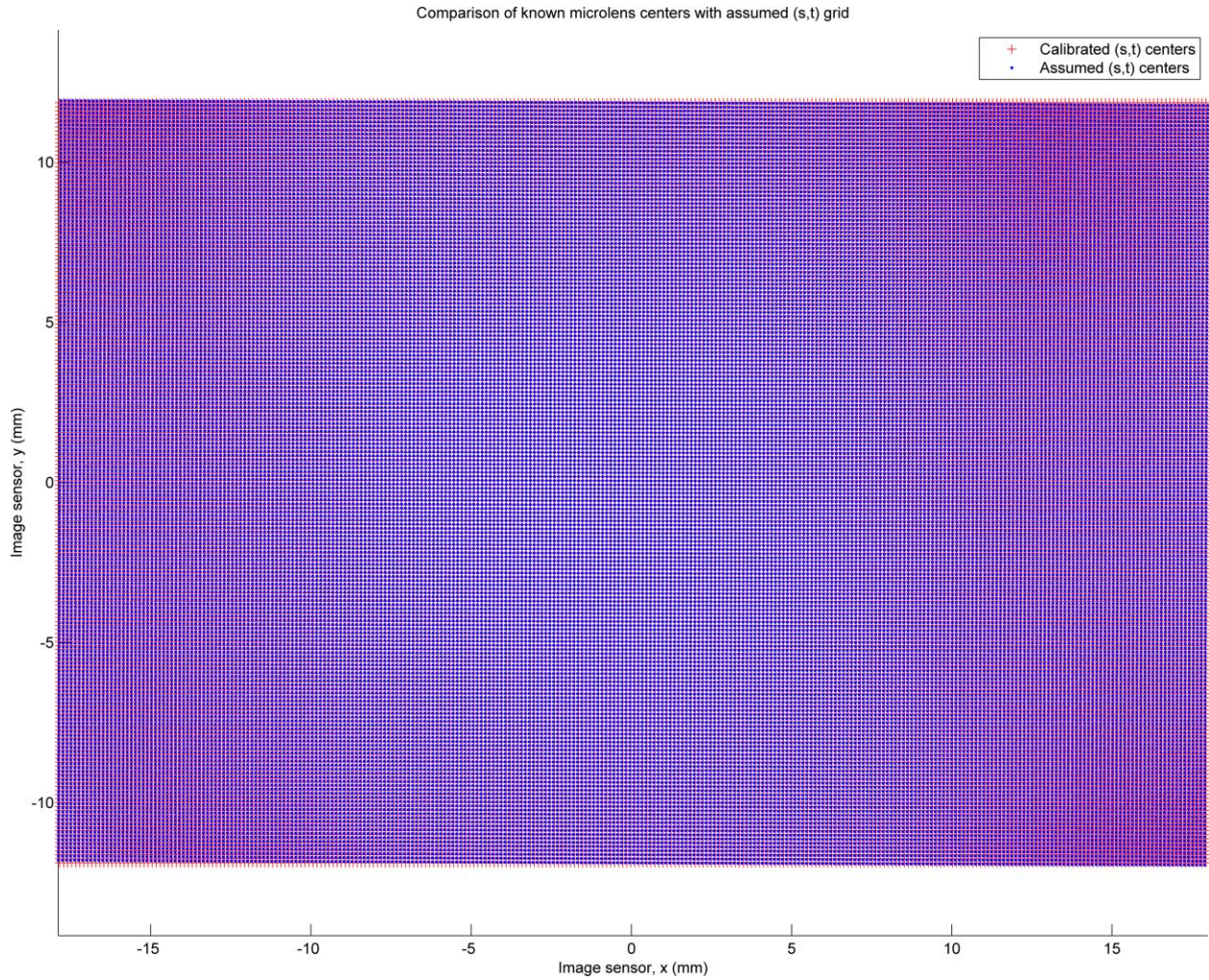


Figure 12: Known  $(u, v)$  coordinates and desired uniform  $(u, v)$  coordinates for microimage interpolation

The known coordinates are derived from the calculated center of the microlens in the calibration step. In  $(u, v)$  coordinates, the microlens center will be located at  $(0,0)$ . However, it is unlikely that the calculated center of the microlens perfectly aligns with a pixel in image coordinates. Because of this, the imaged pixels correspond to a sampling of slightly offset  $(u, v)$  coordinates, marked by blue dots above. Thus, the known offset  $(u, v)$  values are associated with the microimage data.

Using this, a new microimage can be created by interpolating for new values of  $(u, v)$  on a uniform integer (not offset) grid. This process is repeated for every microimage in the raw plenoptic image, as each microimage will be non-uniformly offset relative to the center of its respective microlens. Note that above in the figure, a padded region of known  $(u, v)$  values is used for interpolation purposes. Also, observe that the  $(s, t)$  coordinates are determined by assuming a non-rotated  $(s, t)$  grid centered on the center microlens in the slightly rotated real array.

Ideally, the microlenses are uniformly spaced and perfectly aligned with the image sensor. However, in reality the microlens array in the prototype 16 MP camera is slightly rotated with respect to the image sensor. In LFIT, the  $(s, t)$  grid is assumed to be uniformly spaced and not rotated. During the  $(u, v)$  interpolation step where every microimage is interpolated onto a uniform grid, the microlenses are indexed and assumed to lie on a non-rotated grid. That is, although the entire array is slightly rotated in the actual camera, in practice, LFIT assumes each interpolated microimage would fall neatly on a non-rotated grid. In Figure 13, the known microlens center  $(s, t)$  coordinates are plotted with the assumed  $(s, t)$  grid.



**Figure 13: Comparison of known microlens centers with assumed  $(s,t)$  grid**

From this zoomed out perspective, both grids appear largely aligned. A closer look at the grid reveals small but increasing offsets between the calibrated and assumed  $(s,t)$  centers as one moves away from the center of the sensor. The decision to make this assumption is not because of any difficulty in using the calibrated  $(s,t)$  centers. Rather, this choice was made in large part because it is computationally much more inexpensive to simply assume a uniform  $(s,t)$  grid versus resampling from the calibration  $(s,t)$  centers via a scattered data interpolation. In any case, this assumption is expected to have little to no impact on the present work. Applications

like PIV that rely on precise particle positioning could perhaps attain slightly more accurate results by accounting for this difference.

## **E. Formation of 4D Radiance Array**

### *1. Radiance Array*

Having determined the correct  $(u, v, s, t)$  values for the pixels in each microimage, these pixel intensities can be formed into a 4D radiance array. This array uses the same structure and notation as in the earlier discussion of the light field, albeit with indices  $(i, j, k, l)$  standing in for  $(u, v, s, t)$ .

### *2. Coordinate System Definitions*

The coordinate systems used in LFIT are defined as follows. For the microimage behind a given microlens, there is a constant  $(s, t)$  value associated with the entire microimage. Each pixel will have a different  $(u, v)$  value associated with it. Because of the interpolation of the microimage data onto a uniform  $(u, v)$  grid, these values will be integers in pixel coordinates. Below in Figure 14, the coordinate systems are displayed for a given microimage.



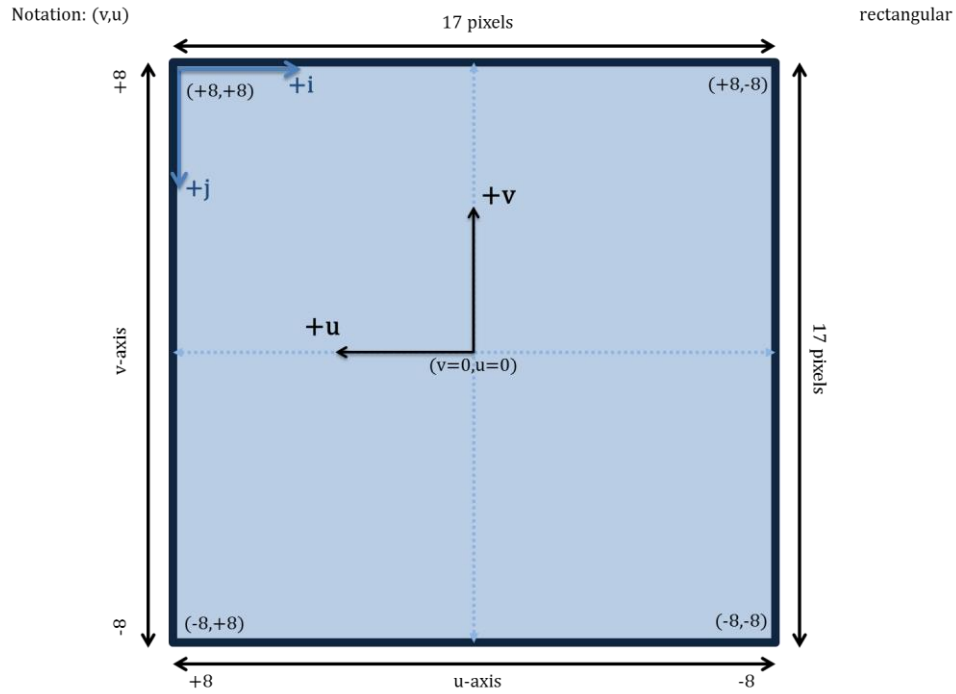


**Figure 14: Coordinate system definitions for a given microimage**

Note the presence of the  $(i, j)$  coordinate definitions in the upper left corner of the microimage. These are the indices used in the radiance array.

Looking at the entire raw image, the  $(s, t)$  coordinates can be defined. Each  $(s, t)$  coordinate pair is associated with a specific microlens in the camera and thus a specific microimage in the raw plenoptic image file. A graphical representation of the coordinate systems applicable to the entire raw image is given below in Figure 15.

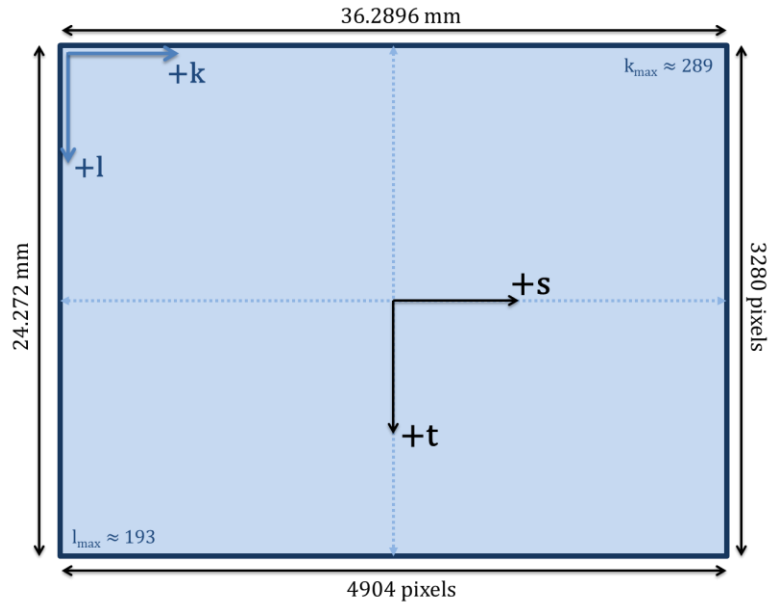


**Figure 15: Coordinate system definitions for the raw image**

The above figure shows the index coordinate vectors for the radiance array as well. Thus, accessing the radiance array at  $(i = 1, j = 1, k = 1, l = 1)$  would return the intensity of the top left pixel from the top left microimage in the scene. With the raw plenoptic image fully processed, it is now possible to computationally form new images from the structured raw data.

## F. Graphic User Interface

The primary graphic user interface (GUI) presents virtually all of the options available in LFIT in an easy to use format without requiring any MATLAB coding ability. This interface, pictured below in Figure 16, facilitates the rapid processing of previously acquired plenoptic images.

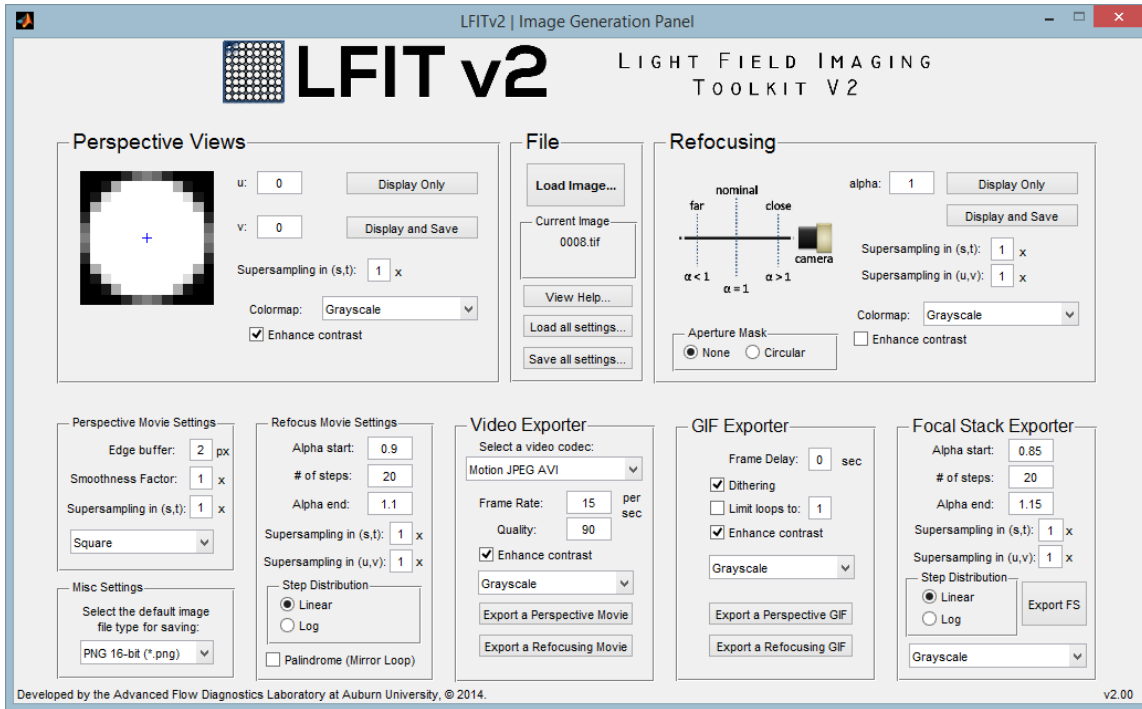


**Figure 16: LFIT graphic user interface for image generation**

A batch mode is also available to run LFIT without this GUI window. The batch mode is useful for repetitive calculations without user interaction, while the GUI streamlines the process of quickly checking experimental data. Two main types of images can be formed from this interface—perspective shifts and refocused images. Both of these types of images and their formation processes are discussed in detail below.

## G. Perspective Shifts

Perspective shifted images are an algorithmically simple type of image to form from a processed plenoptic image. Recall that each microimage consists of a series of angular samples as each microlens images the aperture of the main lens. Thus, different pixels in a microimage will correspond to different angular sets of light rays entering the camera. To create a perspective view, a  $(u, v)$  value is first chosen. A pixel corresponding to that  $(u, v)$  value is then read from

every microimage in the image and stitched together to form an output image. To illustrate this, a diagram of a simplified plenoptic camera image is given below in Figure 17.

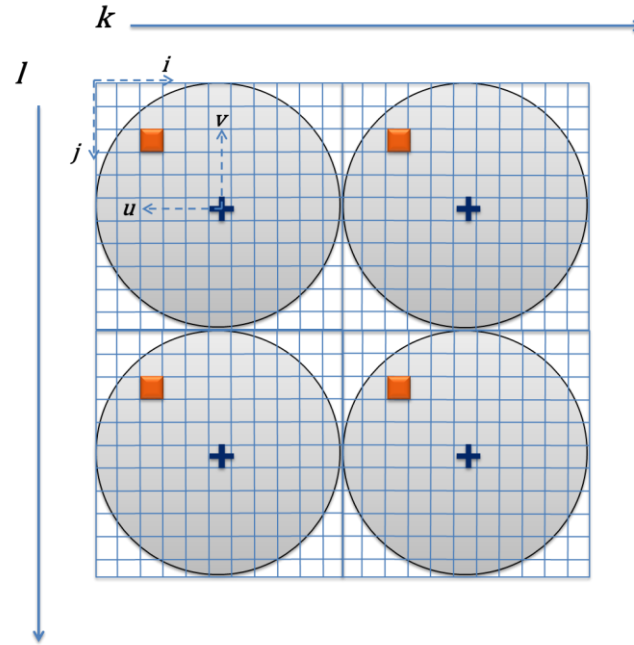


**Figure 17: Simplified diagram of perspective view generation**

Figure 17 above shows a simplified raw image with four microlenses. The circular microimages formed by each microlens are represented by the circles above, with a condensed pixel sampling grid overlaid. From a computational point of view, it is straightforward to form a perspective image. A single pixel from each microimage, highlighted in orange above, is selected and stitched together to form a new output image. For this diagram's 2x2 array of microlenses, the output image size would likewise be a 2x2 pixel image. Neglecting the circular nature of the microimages, the 11x11 grid of pixels over each microlens in the figure would equate to a total of 121 unique perspective views.

To phrase it more generally, each microlens corresponds to a spatial sample of the scene while a given pixel in a microimage corresponds to a single angular sample of the scene. By choosing the same relative pixel from every microimage, one angular sample is pulled from

every spatial sample to form a new output image. Two examples of perspective views are given below in Figure 18.

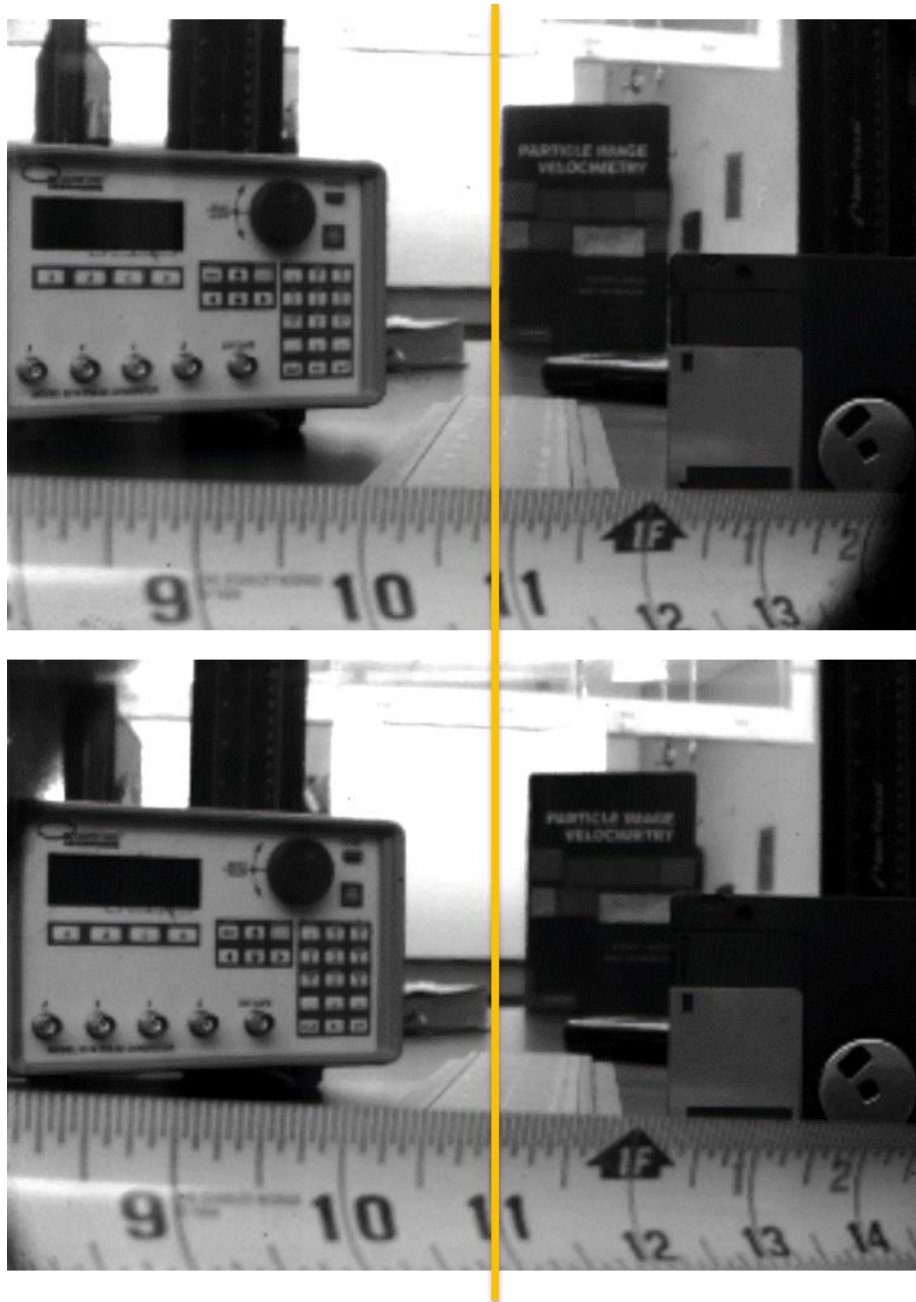


**Figure 18: Two example perspective views of the sample lab scene with reference line**

While the change in perspective can be more clearly seen in animated form on the computer, a close examination of Figure 18 above reveals two separate perspectives. The topmost image in

the figure is viewed from the top left of the aperture. The edge the PIV textbook visually coincides with the reference line drawn over the two perspective views. Inspecting the lower image in Figure 18 at the bottom right of the aperture, the PIV textbook is now significantly separated from the reference line. A similar divergence relative to the reference line can be seen on the tape measure.

For the prototype 16 MP plenoptic camera used in this research, 185 unique perspective views are available, given a main lens with a circular aperture. As alluded to above, perspective animations can be created via LFIT by forming an image sequence composed of discrete perspective views. LFIT supports interpolating for additional views in order to obtain more aesthetically pleasing animations.

## **H. Refocusing**

### *1. Overview*

While perspective shifts are a natural application of the angular data captured by the plenoptic camera, perhaps the most striking application of this information is seen in the ability to computationally refocus a plenoptic image after its initial capture. That is, a single raw plenoptic image can be refocused to new arbitrary focal planes via post-processing.

Consider the original raw plenoptic image (as in Figure 8). The camera lens (and thus the raw image) is physically focused on some nominal focal plane in the scene. In the case of Figure 8, the nominal focal plane is on the floppy disk. It is possible to leverage the angular information recorded by the plenoptic camera to define a new focal plane at some distance offset from the nominal one. A schematic of this concept is presented below in Figure 19. Note that  $A$  is the aperture of the main lens and  $f_{main\ lens}$  is the focal length of the main lens.

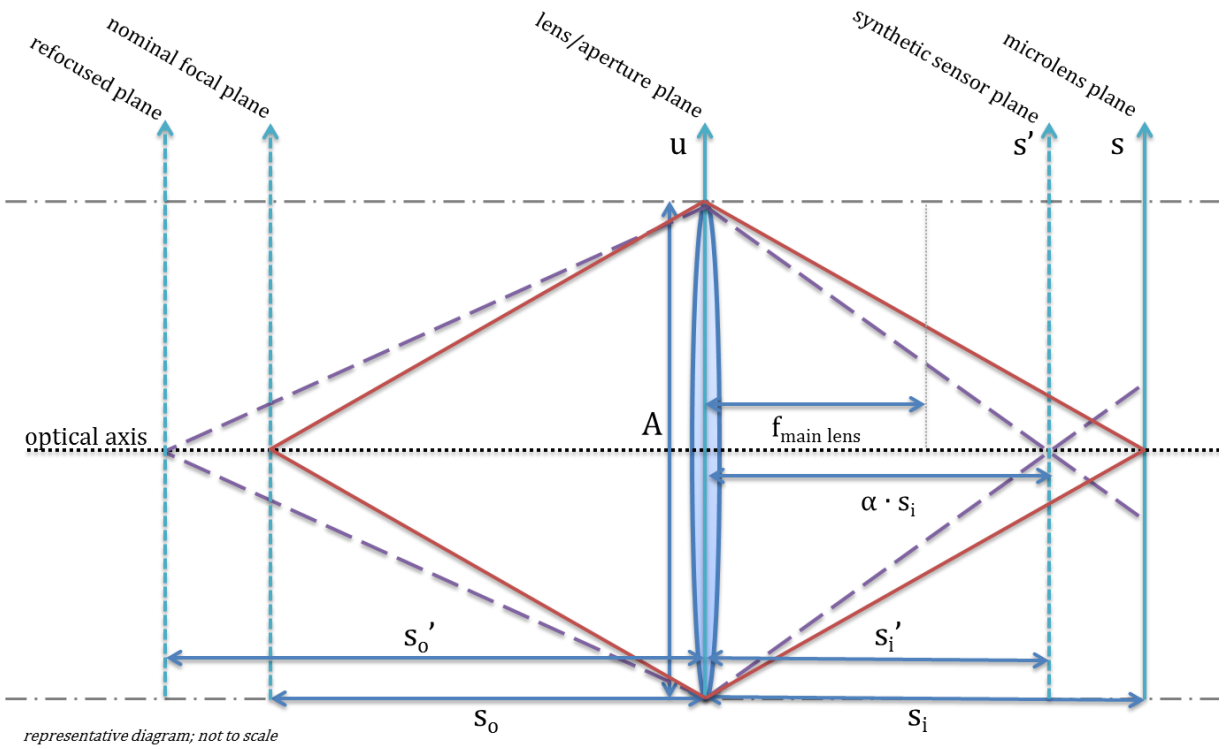


**Figure 19: Schematic depicting process of computational refocusing**

Consider a point source located at the nominal focal plane of the plenoptic camera and on the optical axis. The distance from this point to the main lens is the object distance, given by  $s_0$ . Light rays from such a source are indicated by the solid red line in the figure above. As seen in the diagram, these rays from the point source will converge onto the microlens array at the  $s$  plane where the point source is in-focus. The distance between the main lens and the location of the converged rays is the image distance  $s_i$ .

Now assume a point source located on the optical axis but at some depth beyond the nominal focal plane of the plenoptic camera. Rays from this point source are marked with the dashed purple line above. These rays will converge inside the plenoptic camera some distance in front of the microlens array. The rays have diverged by the time that they strike the microlens plane such that the point source is out of (nominal) focus.

By defining a new synthetic sensor plane  $s'$  at the location inside the camera where the dashed purple rays converge at  $s'_i$ , a new computationally refocused image can be formed. The previously out of focus point source at  $s'_o$  will now be in-focus in the refocused image. The depth of the refocused plane relative to the nominal focal plane is controlled by the depth parameter  $\alpha$ .

## 2. Alpha Scaling in Refocusing Equation

In practice, a modified version of the refocusing equation from Ng is used in LFIT to generate refocused images. The digital refocusing equation as described in [9] is given below in Eq. (2):

$$\bar{E}(s', t') = \iint L\left(u', v', u' + \frac{s' - u'}{\alpha}, v' + \frac{t' - v'}{\alpha}\right) du' dv' \quad (2)$$

Given a light field  $L(u, v, s, t)$ , generated from a raw plenoptic image via LFIT, the above relationship can be implemented in MATLAB. A sample raw plenoptic image consisting of two small LEGO® figures at different depths was selected and loaded into LFIT for this discussion. Note that due to the narrowness of the depth of field and distance between the figures, neither figure will be entirely sharp after refocusing. However, the relatively extreme depths and corresponding disparate  $\alpha$  values of the figures in this scene help illustrate the scaling effects discussed here.

As stated earlier, the depth parameter  $\alpha$  is used to define the location of a new focal plane. Using Eq. (2), two refocused images were generated. Both are shown in Figure 20 below, with the  $\alpha = 0.75$  case at left and the  $\alpha = 1.55$  case at right.



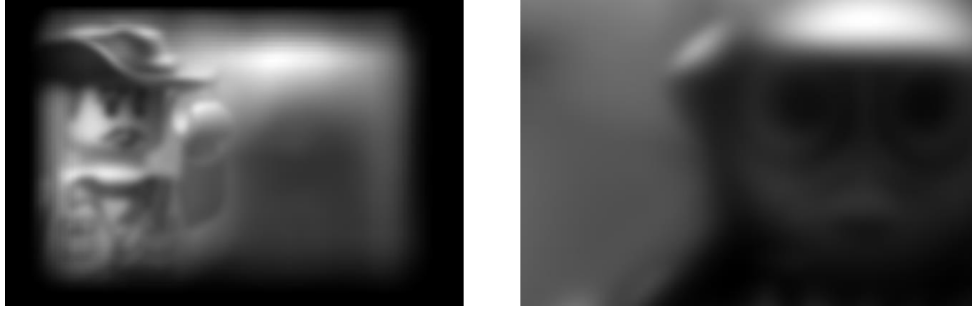


**Figure 20: Direct implementation of refocusing equation with far focus  $\alpha = 0.75$  (left) and close focus  $\alpha = 1.55$  (right)**

Observe that in the above left image, the extent of the rendered image does not fill the output frame. While not immediately apparent, the opposite holds true for the close focused image in the above right image; that is the refocused image is essentially cropped. This occurs because of the change in the location of the synthetic sensor plane. A diagram below in Figure 21 illustrates some of these issues as they relate the image formation process in the context of refocusing.

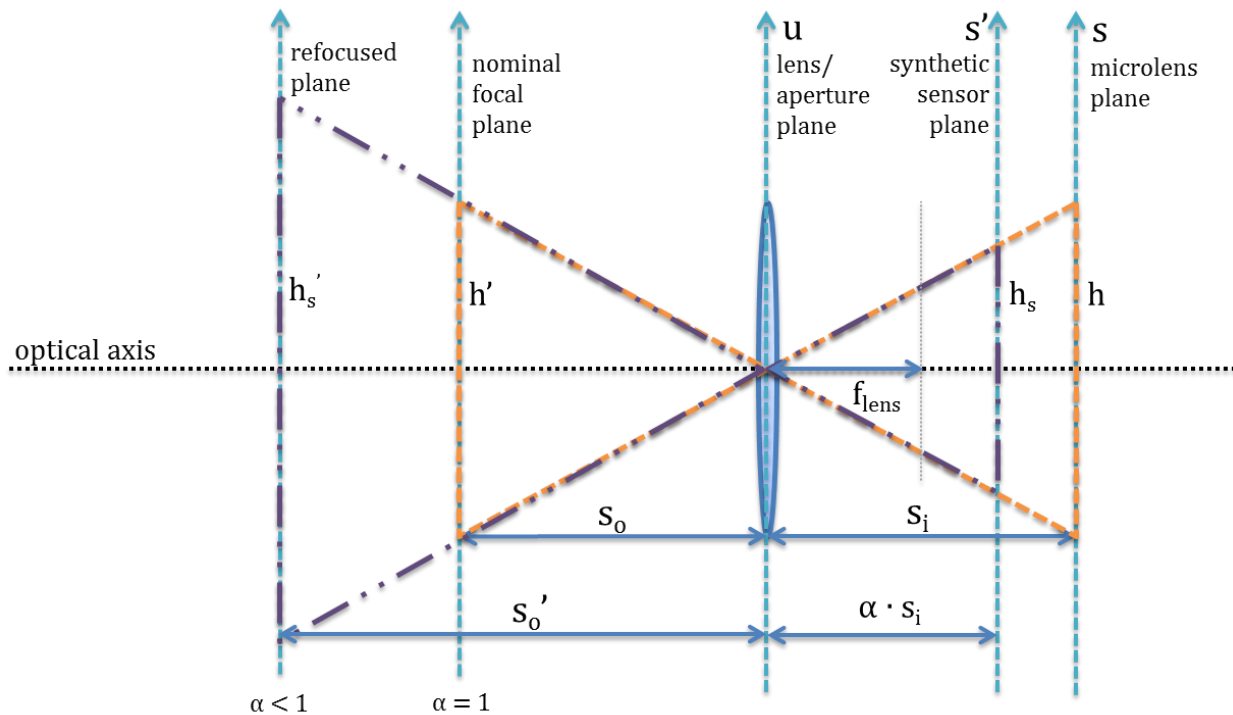


**Figure 21: Diagram of image formation process when computationally refocusing**

The orange dashed lines in the above figure correspond to the nominal focus case where  $\alpha = 1.00$ . The nominal focal plane is imaged onto the microlens plane with a 1:1 magnification as drawn, although the following discussion applies for other nominal magnifications. To computationally refocus onto a more distant object, a value less than 1 should be selected for  $\alpha$ . This far (re)focus case corresponds to the purple dotted line above. As seen in the figure, the image formed on the synthetic, or virtual, sensor will be smaller in size than the size of the initial  $\alpha = 1.00$  image. Directly incorporating Eq. (2) fails to account for this change in size; thus, when refocusing beyond the nominal focal plane, the refocused image only falls on a center part of the sampling grid. The sampling grid is larger than the actual image formed. This can be clearly seen when inspecting the extent of the sampling grid for the  $\alpha = 0.75$  case below in Figure 22.

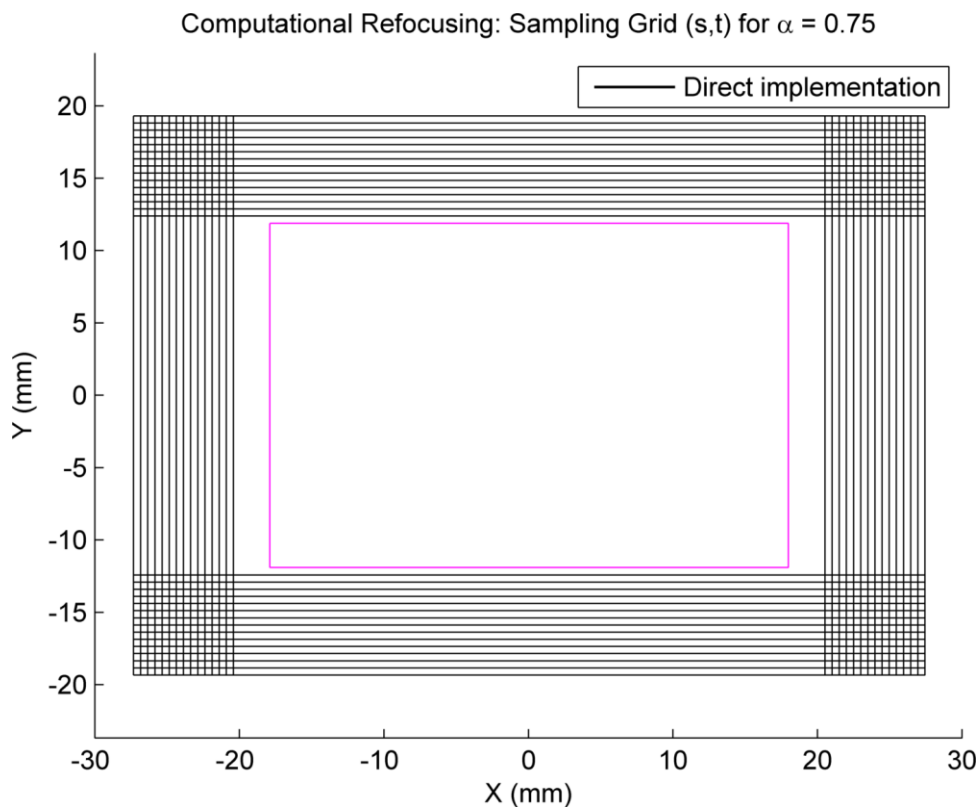


**Figure 22: Direct implementation sampling grid for (s,t) coordinates in computational refocusing at  $\alpha = 0.75$**

Recall that Eq. (2) is a double integral for a range of  $u$  and  $v$  values. For each  $u$  and  $v$  value, a rectangle is plotted above showing the extent of the sampling grid. The grids will shift for different values of  $u$  and  $v$ , leading to the series of overlapping rectangles above in Figure 22. The direct implementation of Eq. (2) results in a sampling grid that is larger than the existing  $(s, t)$  grid of known microlens locations, the extent of which is plotted in the magenta rectangle in the center. Conversely, computationally refocusing in front of the nominal focal plane will cause the image formed to exceed the size of the sampling grid as in Figure 23.

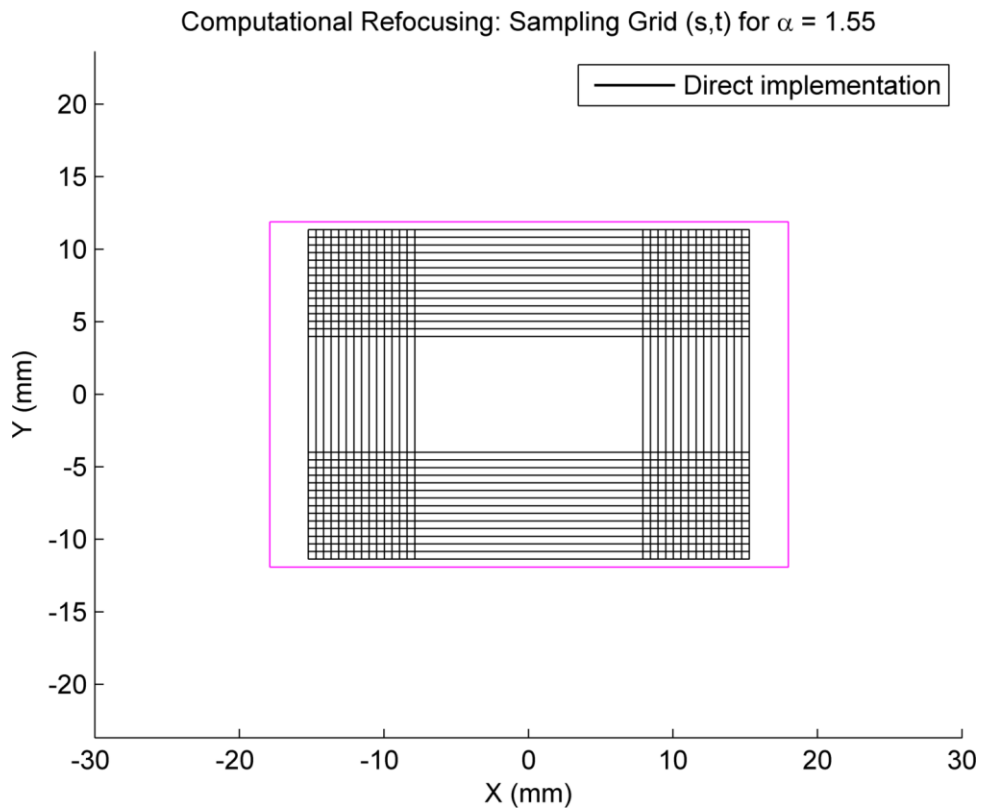


**Figure 23: Direct implementation sampling grid for  $(s,t)$  coordinates in computational refocusing at  $\alpha = 1.55$**

Above in Figure 23, the direct implementation sampling grid only occupies a small region within the existing data set of known  $(s, t)$  positions. This leads to the cropping effect in Figure 20.

To adjust for this variation, the sampling grid that constitutes the synthetic sensor plane can be scaled by  $\alpha$  to account for the varying image size. Revisiting Eq. (2), the  $(s, t)$  sampling in the equation is scaled as follows in Eq. (3).

$$\begin{aligned}\bar{E}(s', t') &= \iint L\left(u', v', u' + \frac{s' - u'}{\alpha}, v' + \frac{t' - v'}{\alpha}\right) du' dv' \\ \bar{E}(s', t') &= \iint L\left(u', v', u' \left(1 - \frac{1}{\alpha}\right) + s', v' \left(1 - \frac{1}{\alpha}\right) + t'\right) du' dv'\end{aligned}\quad (3)$$

Note that above, only  $s'$  and  $t'$  are re-scaled by  $\alpha$ . After making this adjustment, the previous refocused images can be recomputed with Eq. (3). The results of this rescaling are shown below in Figure 24.

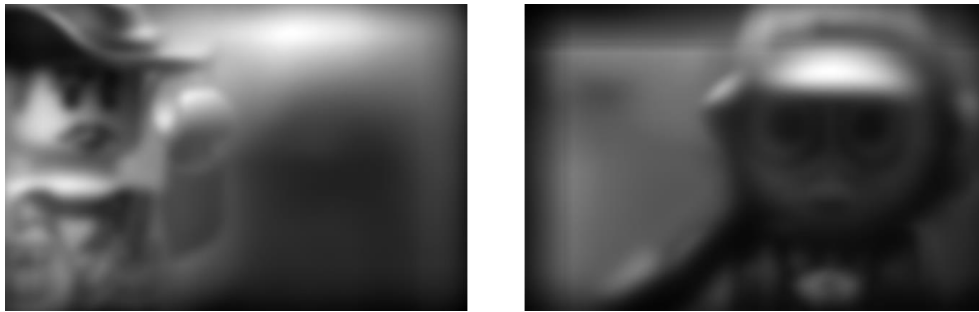


**Figure 24: Modified implementation of refocusing equation with far focus  $\alpha = 0.75$  (left) and close focus  $\alpha = 1.55$  (right)**

Comparing the left image of Figure 20 with the left image of Figure 24, it can be seen that scaling the  $(s', t')$  terms effectively scales the sampling grid to produce refocused images which utilize the full extent of the frame. Examining the right most images from their respective figures, the modified refocusing equation is seen to now fully capture the image formed on the synthetic sensor plane.

It is worth noting here that Eq. (3) is not the equation implemented in LFIT for refocusing. Eq. (3) is a shift-variant equation as noted by Anglin [17]. The above plots in Figure 22 and

Figure 23 show this plotted implementation as shift-variant. While this has only subtle effects on conventional scenes, this shift-variance is a major obstacle to implementing a deconvolution model. However, this can be easily remedied by simply scaling the other terms in Eq. (3) as shown below in Eq. (4).

$$\bar{E}(s', t') = \iint L(u', v', u'(\alpha - 1) + s', v'(\alpha - 1) + t') du' dv' \quad (4)$$

The above equation is now shift-invariant [17], allowing the use of the deconvolution model. Sampling grids analogous to Figure 22 and Figure 23 for this shift-invariant implementation of Eq. (4) are plotted below in Figure 25.

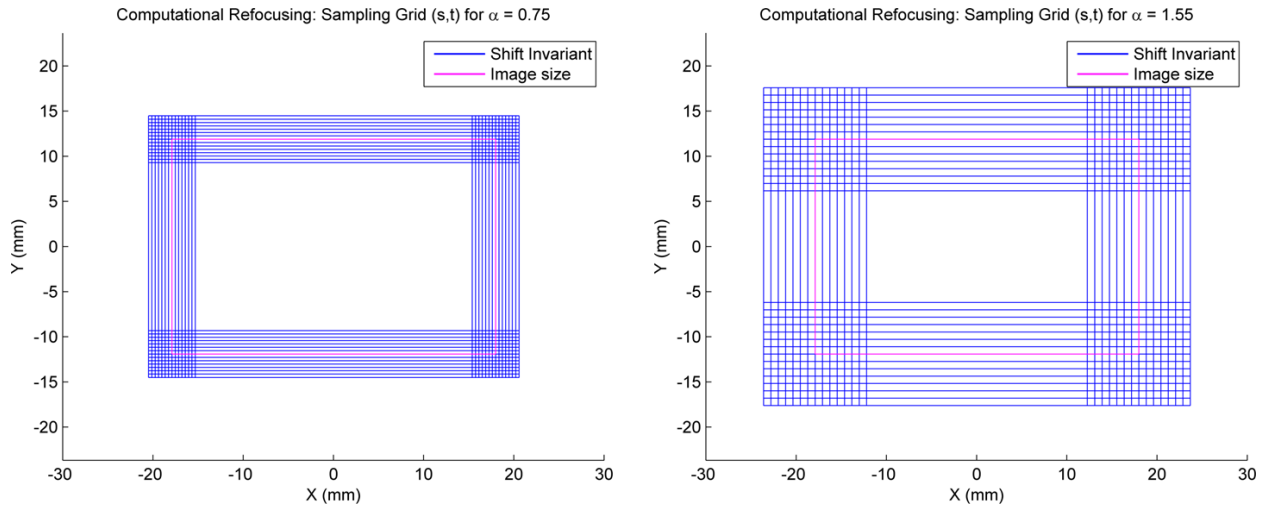


**Figure 25: Shift-invariant sampling grids used in computational refocusing for alpha = 0.75 (left) and 1.55 (right)**

In contrast to the direct implementation, these sampling grids are centered about the extent of the image size. This modification slightly changes the  $\alpha$  values necessary to refocus onto different planes. Finally, note that Eq. (4) is the basis of the refocusing algorithm in LFIT.

The double integral over  $u'$  and  $v'$  is implemented as two for loops in MATLAB to compute the refocused image  $\bar{E}$ . In pixel coordinates,  $u'$  and  $v'$  are between +8 and -8 as each microimage is approximately 17 pixels in diameter, although these values are internally converted to millimeters in LFIT as explained below.

### 3. Pixels to Millimeters Scaling on the Aperture Plane

For consistency in the equations implemented in LFIT, millimeters were chosen as the standard unit to be used. While it is straightforward to convert  $(s, t)$  coordinates from pixels to millimeters given knowledge of the microlens pitch and image sensor size, some thought must be given to the appropriate conversion between pixels and millimeters on the  $(u, v)$  aperture plane. The necessary equations become clear, however, when examining the schematic below in Figure 26.

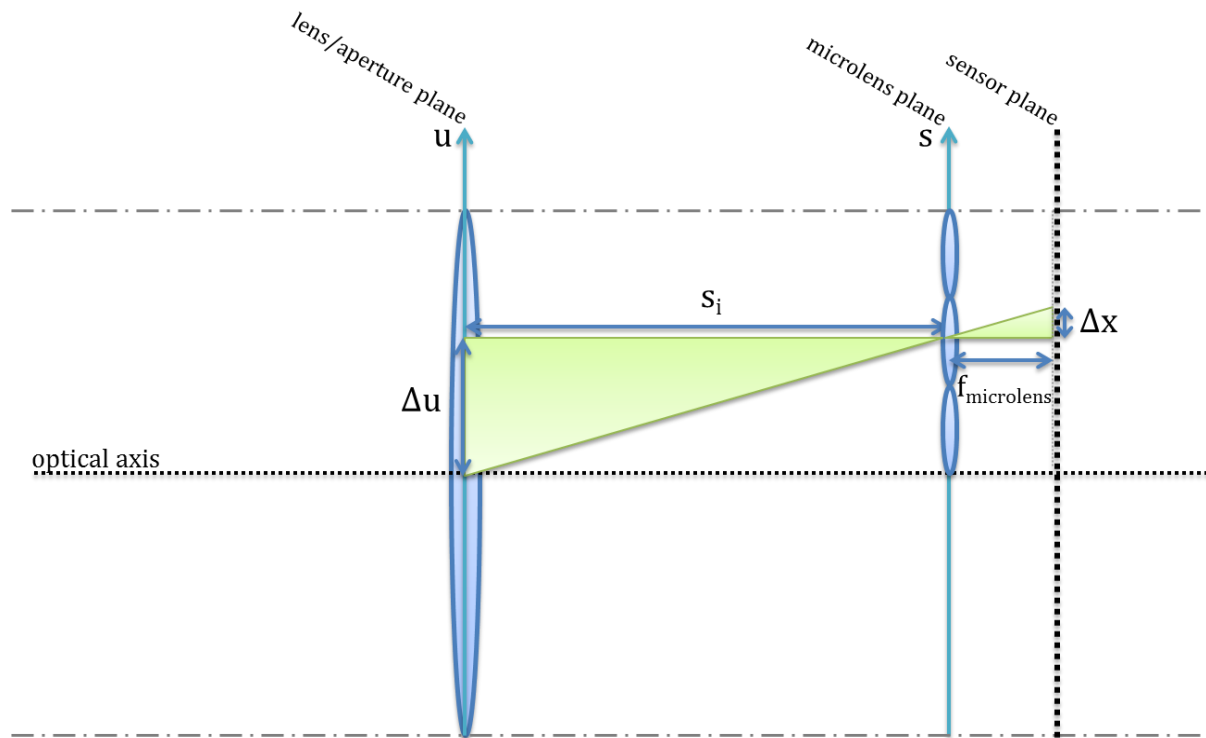


Figure 26: Pixels to millimeters scaling on the  $(u, v)$  aperture plane

Via similar triangles, a displacement in the aperture plane  $\Delta u$  can be related to a displacement on the sensor plane  $\Delta x$  as in Eq. (5).

$$\Delta u = \Delta x \frac{s_i}{f_{\text{microlens}}} \quad (5)$$

In terms of pixels and millimeters, this becomes Eq. (6).

$$\Delta u|_{\text{millimeters}} = \left( \Delta x|_{\text{pixels}} \cdot (\text{pixel pitch}|_{\text{millimeters}}) \right) \left( \frac{s_i|_{\text{millimeters}}}{f_{\text{microlens}}|_{\text{millimeters}}} \right) \quad (6)$$

In this way,  $(u, v)$  coordinates can be appropriately scaled from pixel coordinates to millimeters.

#### 4. Further Discussion and Demonstration

Note that when  $\alpha = 1$ , the  $(s, t)$  terms in the 4D light field  $L(u, v, s, t)$  above become simply  $(s', t')$ , and the resulting image is focused on the nominal focal plane. Different values of  $\alpha$  will change the values of  $(s, t)$  being evaluated. Values of  $\alpha < 1$  move the refocused focal plane to distances beyond the nominal focal plane, whereas values of  $\alpha > 1$  move the refocused focal plane closer to the camera. Typically a circular aperture is assumed to increase the speed of data processing and remove the influence of noise or other artifacts in the spaces between the microimages. As an aside, it is also possible to supersample the images by increasing the fineness of either the  $(s, t)$  or  $(u, v)$  grids. This results in smoother, more visually pleasing output images with the tradeoff of additional processing time. For additional discussion on the assumption of a circular aperture as well as the influence of supersampling on the sampling grid, refer to Appendix C.

Again returning to the sample lab scene pictured in Figure 7, the raw plenoptic image shown in Figure 8 can be refocused via LFIT according to the discussion above. Below in Figure 27, a far refocused and close refocused image are both depicted.

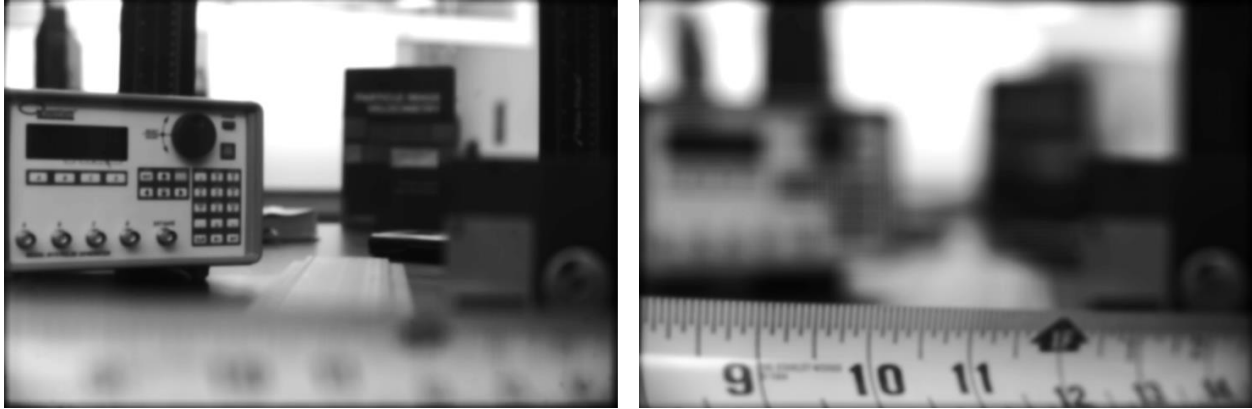


**Figure 27: Sample refocused image at  $\alpha = 0.95$  (left) and  $\alpha = 1.06$  (right)**

The leftmost image shows a refocused image for  $\alpha = 0.95$ . The pulse generator is now in focus in the left of the frame, while objects at distances different from the generator are now out of focus. Examining the rightmost image, the pulse generator is now seen to be out of focus while the previously blurred tape measure is now in focus. The rightmost image corresponds to  $\alpha = 1.06$ . This simple demonstration illustrates the power of plenoptic imaging. From a single raw plenoptic image, new photographs can be formed computationally.

## **I. PIV Processing**

While the previous applications of perspective shifts and refocusing demonstrate the plenoptic camera's capabilities in the context of general photography, this technology has also been applied in a more quantitative fashion in the realm of particle image velocimetry (PIV). Although not a part of LFIT currently, other software developed by our lab is used for plenoptic PIV processing. PIV is a technique for obtaining the velocity distribution in a given flow field [1]. PIV uses a pair of images, taken in rapid succession, of a particle-seeded flow to determine displacements (and thus velocities) of discrete groupings of particles as they translate between the two images.



In a conventional 2D PIV experiment, the flow is first seeded with particles. These particles are of sufficient size to be resolved by the camera, without being so large that they do not follow the flow. A laser is directed with appropriate optics to form a laser sheet in a 2D portion of the volume, such that the sheet intersects with the flow in the plane desired for imaging. A single camera is positioned to view the laser sheet so that the optical axis of the camera is orthogonal to the planar laser sheet. The laser is usually double-pulsed, with the camera capturing frames of the volume at these pulses over a very short time frame (on the order of microseconds).

Comparing a pair of captured images visually shows the displacement of particles from the first frame to the second frame. Many algorithms have been developed and implemented to process these images to build up a velocity field. By correlating the two images, the particles in one image can be computationally matched to the particles in the second image. Then, measuring the pixel displacements between the two frames allows for the calculation of the velocity vector for a given particle location if the experimental parameters are known (time between pulses, volume size/magnification, etc.). In this way, the entire velocity field at the laser sheet can be measured.

As discussed earlier, it is possible to extend this measurement to a 3D volume by adding enough additional cameras to form an array as in tomographic PIV. However, the optical access required for such an approach can be prohibitive. The plenoptic camera is capable of overcoming many of the limitations of tomographic PIV in this application [11]. As a single camera technique, the optical access requirements are much lower than even two camera stereo PIV. Currently, plenoptic PIV relies on the use of the Multiplicative Algebraic Reconstruction Algorithm (MART) to reconstruct a 3D volume containing particles [12]. While MART is computationally expensive, work is ongoing towards developing faster algorithms [22]. These

reconstructions are handled by software (ALFA/Dragon) developed by Tim Fahringer in our lab. An example of plenoptic PIV applied to flow behind a hemisphere is given below in Figure 28. This example was provided courtesy of Kyle Johnson.

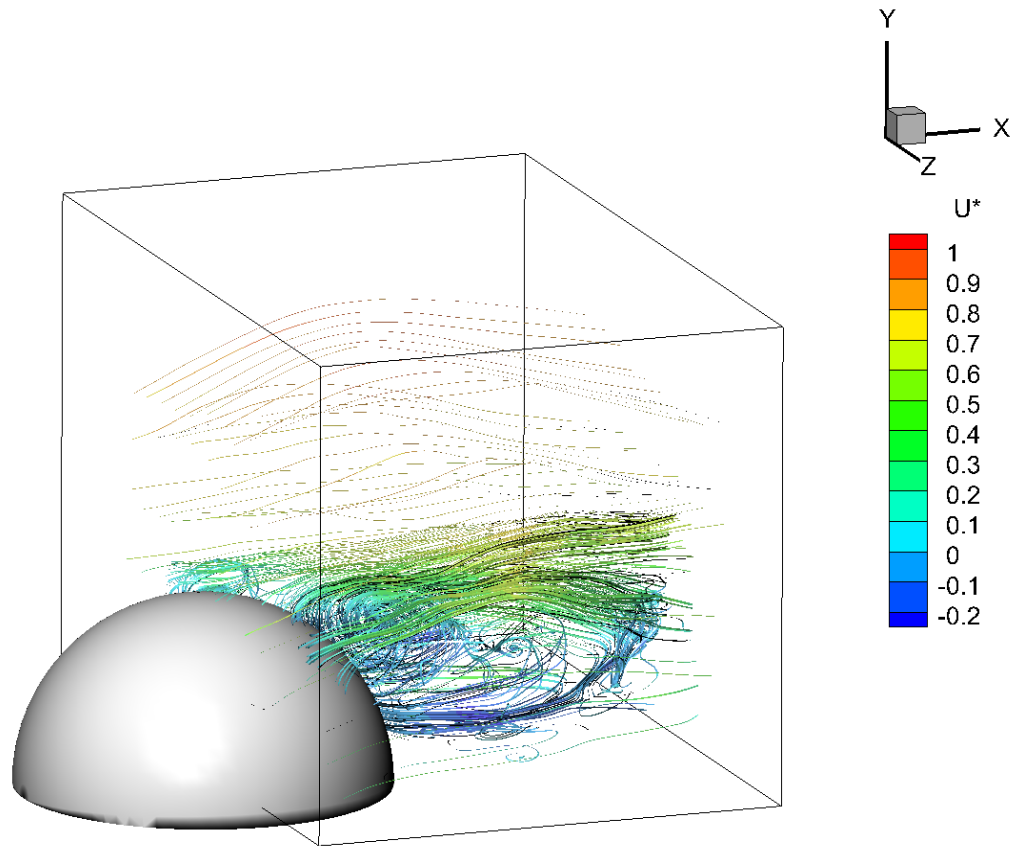


**Figure 28: Example of plenoptic PIV behind a hemisphere**

This particular experiment was designed to inspect flow structures in the wake behind a 1” diameter hemisphere as an initial step before tackling more complex flows with multiple hemispheres. The experiment was conducted in a refractive index matched water tunnel facility at a velocity of 0.3957 m/s, examining a 50 x 34 x 34 mm sized volume with a 300 x 205 x 205 voxel grid. From a single pair of plenoptic images, 3D velocity data as above can be determined. Although the plenoptic camera is still a relatively new flow diagnostic tool, the ability to capture 3D information in a single snapshot makes it a compelling device.

## IV. Resolving Depth Information

### A. Computational Refocusing

Having above demonstrated the power of the plenoptic camera to capture 3D information about a scene, a technique must be chosen to most effectively represent a given plenoptic image in a three-dimensional sense. Attention must be given to the applicability of the technique to imaging in environments with translucent occlusions or flames. For example, the reconstruction software and algorithms used by our lab for PIV are not well-suited for imaging most chemically reacting flows. The smooth gradients and translucent nature of the types of flows being investigated in this work differ substantially from the assumptions made in the context of imaging finite particles in PIV.

Perhaps the most straightforward way to leverage the spatial and angular information captured by a plenoptic camera is to form a focal stack via computational refocusing. A focal stack is generated from a single raw plenoptic image and consists of a series of images refocused to different depths in the imaged volume. The focal stacks used in this work are typically defined in terms of a minimum/maximum depth parameter  $\alpha$  and the number of the images in the stack, which are spaced uniformly in  $\alpha$ . Note that this thesis often uses the term *slice* to denote a single image from a given focal stack.

Depending on which image in the focal stack is selected, different objects in the scene will come into or out of focus. The blurring of objects off the refocused focal plane gives an indication of the depth of such objects. When a given object has maximum sharpness, its depth can be inferred to be at the depth of that refocused focal plane.

However, when objects are off the focal plane of the camera, the blur from these objects can obscure the desired image at the refocused focal plane. That is, a given slice (image) of the focal

stack contains not only the in-focus image at that depth but also intensity contributions from blurred objects off the focal plane. Because of this, the focal stack can be thought of as a rough 3D approximation of the volume.

Each slice in the focal stack corresponds to a different location of the synthetic focal plane in the volume. This can be seen by examining the thin lens equation in Eq. (7) below.

$$\frac{1}{s_i} + \frac{1}{s_o} = \frac{1}{f_{main\ lens}} \quad (7)$$

Note that  $s_i$  corresponds to image distance,  $s_o$  to object distance, and  $f_{main\ lens}$  to focal length of the main lens. It is straightforward to solve for  $s_o$ , as the focal length of the main lens is known and  $s_i$  can be calculated from the (positive) magnification  $M$  as in Eq. (8) below.

$$s_i = (f_{main\ lens})(1 + M) \quad (8)$$

In practice, the magnification for an experiment can be easily measured by placing a ruler or object of known dimensions at the nominal focal plane of the camera [23]. The thin lens equation of Eq. (7) can then be rewritten for the case of computational refocusing. Substituting  $s'_o$  for  $s_o$  and  $s'_i = \alpha \cdot s_i$  for  $s_i$  as in Figure 19 results in Eq. (9), which can be rearranged to yield Eq. (10).

$$\frac{1}{\alpha \cdot s_i} + \frac{1}{s'_o} = \frac{1}{f_{main\ lens}} \quad (9)$$

$$s'_o = \left( \frac{1}{f_{main\ lens}} - \frac{1}{\alpha \cdot s_i} \right)^{-1} \quad (10)$$

The above Eq. (10) can be used to calculate the depth location of the refocused focal plane for each layer of the focal stack. Generally this will be expressed as an offset from the nominal focal plane  $s_o$  of the experiment. Assuming a focal length of 50 mm, Eq. (10) can be plotted for a variety of magnifications as in Figure 29 below.

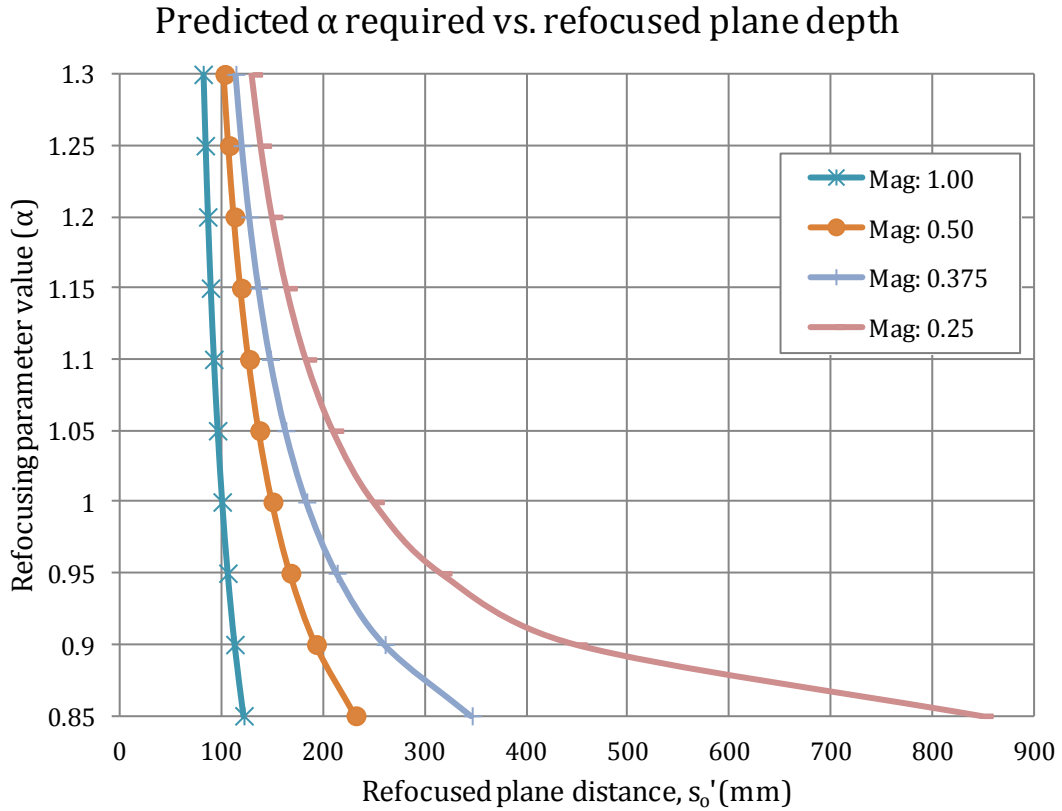


**Figure 29: Variation of alpha with focal plane depth for varying magnifications**

For high magnifications, the refocused plane distance varies slowly with  $\alpha$  whereas at low magnifications the refocused focal plane distance changes rather dramatically. This observation makes more sense in light of the quantity known as depth of field (DOF).

The DOF of an imaging system is the range about the focal plane of the camera in which objects are acceptably sharp [24]. While arbitrary values of  $\alpha$  can be used to refocus to arbitrary focal planes in the volume, the depth resolution of the plenoptic camera is not infinite. The DOF of the optical setup will constrain the resolution in depth of the refocused images. The DOF for close objects (where the magnification is between 0.1 and 1.0) can be represented by Eq. (11) below.

$$DOF = \frac{2CN(1 + |M|)}{M^2} \quad (11)$$

The above equation gives the depth of field, where  $C$  is the circle of confusion,  $N$  is the f-number, and  $M$  is the magnification. The circle of confusion refers to the size of the blur circle below which image detail cannot be perceived [24]. While historically the circle of confusion in general photographic applications often incorporates additional considerations related to print size and the acuity of the human visual system, the most relevant factor to consider in this analysis is the pixel size on the image sensor.

In a conventional camera, the pixel size can be used to calculate the circle of confusion. However for a given image sensor in a plenoptic camera, the spatial resolution is constrained by the number of microlenses in the microlens array. As each microlens represents a single spatial sample, for the plenoptic camera it is appropriate to take the microlens size as the circle of confusion. For the prototype camera used in this research, the image sensor has microlenses with diameters of 0.125 mm compared to a pixel size of 0.0074 mm.

Returning to Eq. (11), for a fixed circle of confusion and aperture, the DOF will be small for high magnifications and large for low magnifications. Plotting Eq. (11) over the valid magnification range for a variety of f-numbers yields Figure 30 below. A circle of confusion of 0.125 mm was used.

### Variation of DOF with Magnification

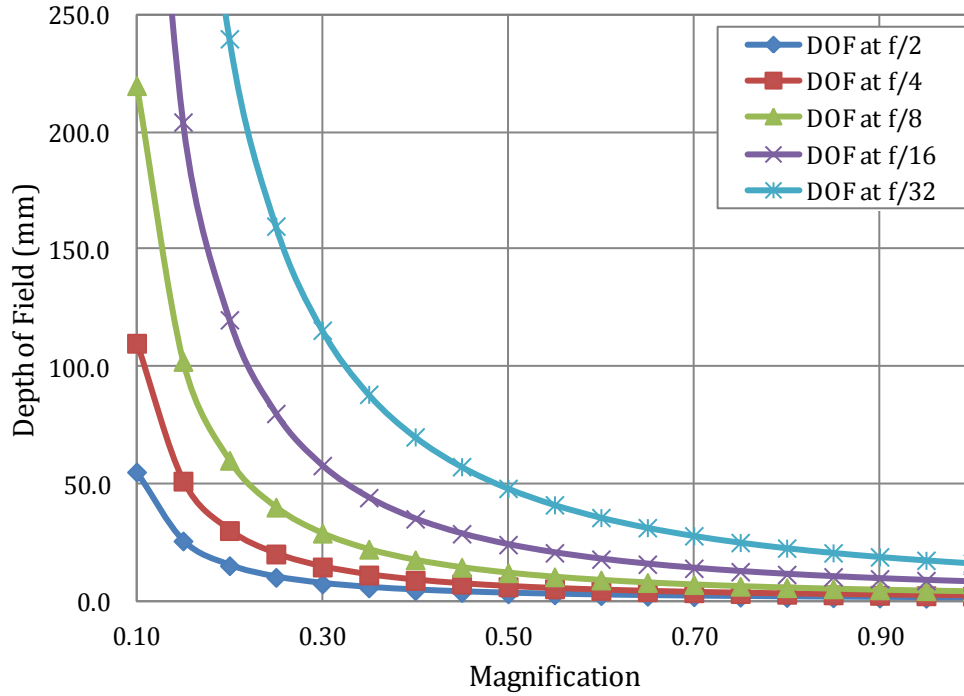


**Figure 30: Depth of field variation with magnification for different f-numbers**

As magnification increases, the DOF shrinks for all f-numbers. For smaller aperture sizes (higher f-numbers), the size of the DOF increases more rapidly as the magnification decreases. To maximize the depth of field in a conventional camera, the aperture of the main lens can be reduced in size by increasing the f-number. The tradeoff is that with less light entering the camera, a longer exposure is required to record a sufficiently high signal. Recall that with the plenoptic camera, images are captured with the main lens aperture as open as large as possible without inducing overlap between the sub-aperture images behind each microlens. While this ensures maximum angular sampling, this has the additional benefit of increasing the recorded signal intensity.

By selecting the same relative pixel behind each microlens, a perspective image can be formed. This perspective image will have a depth of field which corresponds to an aperture that

is  $1/P$  large, where  $P$  is the number of pixels across each microlens. That is, the synthetic aperture of the perspective image will be  $P$  times narrower than the actual aperture of the main lens. This means that a single pixel sets the overall depth of field for the image. An example plenoptic image generated using only 1 pixel from each microlens is shown below in Figure 31.



**Figure 31: Representative (stopped-down) aperture diagram and resulting image with wide DOF**

Most of the above scene in the rightmost image in Figure 31 is in focus. This is the maximum depth of field possible for the raw plenoptic image Figure 31 was generated from. Note that the diagram to the left of the figure represents the aperture plane, where only the center pixel is selected. Compare this diagram and image to the corresponding Figure 32.

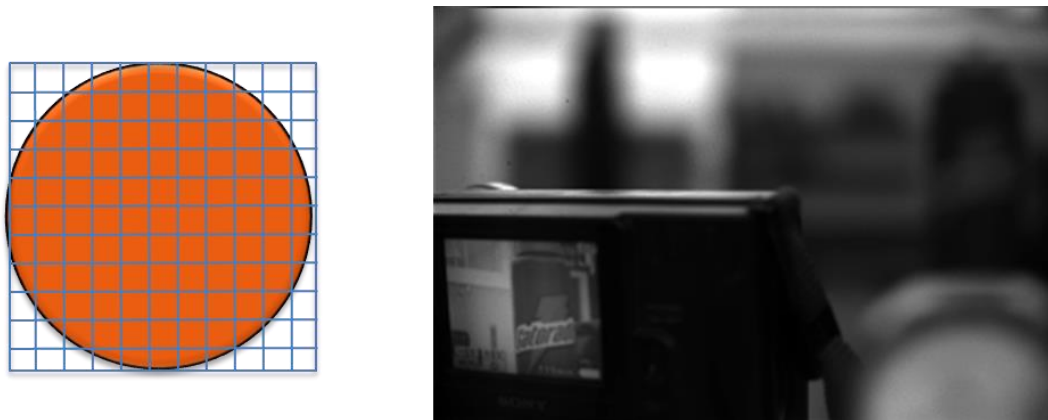


**Figure 32: Representative (full) aperture diagram and resulting image with narrow DOF**



Comparing Figure 31 to Figure 32, the increased depth of field afforded by a digitally stopping down the aperture (as in a perspective view) can be seen. The aperture in Figure 32 is fully open, creating a narrow DOF. The camera in the scene above is the only object in focus since it falls within the depth of field about the focal plane for a main lens aperture that is  $P$  times narrower.

The key conclusion from the above discussion is that the number of distinct planes that can be refocused is proportional to  $P$ . In other words, if a single pixel sets the overall depth of field, then  $P$  different planes should be resolvable within that depth of field. Refocusing beyond those limits is technically possible. However, if refocusing beyond the overall depth of field limits, the spatial resolution will be lower than within the limits. Alternatively, generating more images in the focal stack than are theoretically unique in terms of depth resolution will increase computation time but otherwise should have a negligible effect.

## **B. Deconvolution**

### *1. Introduction*

Three-dimensional deconvolution promises improvements over the method of computational refocusing alone. As stated above, the refocusing technique suffers from out-of-plane blur contributions to the desired in focus plane being examined. Three-dimensional deconvolution seeks to reassign these out-of-plane blurs to their original in focus locations. Note, however, that the depth of field considerations outlined above apply to this technique as well.

All deconvolution algorithms are based on the principle on convolution. Convolution can be conceptualized as moving a filter mask rotated 180 degrees over a given image, multiplying the filter with the image, and summing the results at each location [25]. Mathematically, this relationship can be represented for the 2D case as in Eq. (12).

$$g(x, y) = \int_{-\infty}^{\infty} \int_{-\infty}^{\infty} f(\alpha, \beta) h(x - \alpha, y - \beta) d\alpha d\beta \quad (12)$$

In the image restoration context of this research, a 3D version of this framework is used to model the influence of blur on an image. While there are several types of image degradation including noise and glare, deconvolution specifically seeks to ameliorate image degradation due to blur. Given a theoretical sharp image  $f$ , a blurring function  $h$  will spread out the intensity (that is, blur)  $f$  to create a degraded image  $g$ . The goal of deconvolution is to reverse this process and recover the sharp image  $f$ . Although there are many available deconvolution algorithms [26], [27], they can all be broadly classified into one of two categories: 2D methods and 3D methods.

### *1. Two-Dimensional Deconvolution Techniques*

Two-dimensional methods are the most straightforward deconvolution algorithms to implement. Sometimes these 2D techniques are referred to as deblurring methods. One may be familiar with such algorithms in commercially available image editors, where a common 2D deconvolution based method of deblurring is known as an unsharp mask.

When applied to a 3D image stack (focal stack), 2D deconvolution techniques operate on a slice-by-slice basis. Only a single slice of the focal stack is processed at a time, taking into account only the current slice or at most a few neighboring slices. While computationally inexpensive, 2D deconvolution has several drawbacks compared to the 3D methods to be discussed. Because blur is removed from each plane rather than being restored to the focal plane from which it originated, there will be an overall drop in signal intensities. Although contrast is improved, the reduction in signal intensity lowers the signal-to-noise ratio in the deconvolved images. Another drawback is the possible creation of artifacts. As the processing associated with a given slice cannot account for information in all the other slices contained throughout the focal stack, areas that are actually smooth may be artificially sharpened at slices different from their

actual depth in the scene. Finally, the intensities of pixels relative to one another are not held constant throughout the focal stack as each slice is treated independent of the whole focal stack. This nonlinearity in processing prevents certain quantitative measurements that rely on the relative ratios of intensities between slices.

## 2. *Three-Dimensional Deconvolution Techniques*

Three-dimensional deconvolution addresses the above limitations of 2D deconvolution by operating on the entire focal stack rather than on an independent slice-by-slice basis. Rather than attempting to simply remove the blur from a given slice, 3D deconvolution techniques seek to reassign the out-of-focus light (blur) at a given plane back to the plane at which it was originally in focus. The method of 3D deconvolution is built upon the assumption that the blur in an image can be represented by the convolution of a hypothetical in-focus image stack with some 3D blurring function. Extending Eq. (12) to three dimensions and adding a noise term, the resulting model is typically shown in the shorthand form of Eq. (13) below.

$$g(x, y, z) = f(x, y, z) * h(x, y, z) + \eta \quad (13)$$

In the above equation,  $g(x, y, z)$  is the experimental blurred image stack,  $f(x, y, z)$  is the hypothetical sharp image stack (volume), and  $h(x, y, z)$  is a function modeling the blurring process. The blurring function  $h(x, y, z)$  considered here is the point spread function, which will be discussed in more detail below. A noise term,  $\eta$ , is included since noise will be present in any real image. The process of 3D deconvolution seeks to solve for the in focus image stack,  $f(x, y, z)$ . While there are a variety of 3D deconvolution algorithms in the literature, they can be logically grouped per [26] as linear methods, nonlinear methods, statistical methods, and blind deconvolution methods.

The most direct type of 3D deconvolution approaches are the linear methods. These methods solve for  $f(x, y, z)$  in Eq. (13) in a straightforward manner. Inverse filtering is one of the most basic linear techniques as well as the oldest [27]. An inverse filter is given in Eq. (14) by transitioning to the frequency domain and solving directly for  $f(x, y, z)$ .

$$F(\omega_x, \omega_y, \omega_z) = \left[ \frac{G(\omega_x, \omega_y, \omega_z)}{H(\omega_x, \omega_y, \omega_z)} \right] \quad (14)$$

While very simple to implement, the inverse filter does not handle noise well, as zero or near zero terms in the denominator cause significant noise amplification. A more useful linear technique is that of the regularized 3D Wiener filter.

The regularized 3D Wiener filter incorporates a regularization parameter in the denominator to address the limitations of the inverse filter. The 3D deconvolution relationship for a Wiener filter is given below in Eq. (15).

$$F(\omega_x, \omega_y, \omega_z) = \left[ \frac{H^*(\omega_x, \omega_y, \omega_z)}{|H(\omega_x, \omega_y, \omega_z)|^2 + \frac{S_\eta(\omega_x, \omega_y, \omega_z)}{S_f(\omega_x, \omega_y, \omega_z)}} \right] G(\omega_x, \omega_y, \omega_z) \quad (15)$$

The  $S_\eta$  term represents the power spectra of the noise; the  $S_f$  term likewise represents the power spectra of the original image volume. When neither of these terms is known as is the case here [17], it is common to let  $K = S_\eta/S_f$ . This regularization parameter is a constant that can be adjusted to vary the strength of the deconvolution. The regularization parameter incorporates into the deconvolution relationship an assumption regarding the smoothness of the objects in the scene. A large regularization parameter will reduce high frequency content in the frequency domain (and thus the scene), producing a smoother image. Smaller regularization parameters will preserve this high frequency content, although the previous considerations regarding noise

amplification in the inverse filter can become a concern. With this substitution, Eq. (15) becomes Eq. (16).

$$F(\omega_x, \omega_y, \omega_z) = \left[ \frac{H^*(\omega_x, \omega_y, \omega_z)}{|H(\omega_x, \omega_y, \omega_z)|^2 + K} \right] G(\omega_x, \omega_y, \omega_z) \quad (16)$$

Again, recall the connection to Eq. (13), albeit with the terms here converted to the frequency domain via fast Fourier transforms (FFT) in 3D.  $F(\omega_x, \omega_y, \omega_z)$  is the deconvolved image stack,  $H(\omega_x, \omega_y, \omega_z)$  is the point spread function,  $G(\omega_x, \omega_y, \omega_z)$  is the refocused image stack, and  $K$  is the regularization parameter.

Other linear methods include the linear least squares method and Tikhonov filtering. It should be noted that all linear methods are quite sensitive to the choice of the point spread function (PSF). Mismatches between the defined PSF and the actual PSF can cause significant artifacts in the deconvolved image stack. Linear methods are straightforward to implement and computationally inexpensive. Nonlinear methods incorporate additional constraints (regularization, positivity) in an iterative fashion but increase the computational overhead in both implementation and processing cost. Statistical methods are well suited for handling very noisy inputs, but with a further increase in computational requirements. Blind deconvolution tackles the problem from a different perspective by not requiring a PSF model to be specified, although popular implementations of the technique can be sensitive to noise.

For this research, a regularized 3D Wiener filter was selected for use. A fellow research group at Auburn helped pioneer the use of such a filter [17], [28] with plenoptic images. The author is indebted to Paul Anglin and Dr. Stanley Reeves for their generous assistance in implementing Eq. (16) in MATLAB. This regularized 3D Wiener filter technique is straightforward to

understand and implement and provides a useful baseline for future work with more advanced/computationally expensive algorithms.

To perform this 3D deconvolution in practice, one (or more) plenoptic images are captured during an experiment. Following the completion of the general experimental process described earlier, LFIT is used to generate a focal stack of a given plenoptic image. The focal stack images are spaced equally in  $\alpha$  to maintain the assumption of shift-invariance per the discussion in [17]. This corresponds to a linear spacing in image space but a non-linear spacing in object space. A 3D FFT is then taken of the focal stack to obtain  $G(\omega_x, \omega_y, \omega_z)$ , the experimental focal stack in the frequency domain. To obtain  $H(\omega_x, \omega_y, \omega_z)$ , the point spread function must be characterized.

### *3. Point Spread Function*

The point spread function (PSF) is the impulse response of an optical system that characterizes how an imaged point of light spreads out as the point source is translated away in depth from the nominal focal plane. At the focal plane, a 2D slice of the PSF will be a small, in focus point; away from the focal plane, this point blurs (spreads) according to the optical configuration. A different optical setup will result in a different PSF. The quality of the 3D deconvolution results will vary with the quality of the supplied PSF.

In the field of microscopy where deconvolution is commonly applied [29], the PSF is often calculated experimentally. A slide with sub-pixel sized fluorescent beads is prepared, mounted, and then translated through the desired experimental volume beneath the microscope. A bead is treated as a point source and used to create an image stack of the bead at different defined depths in the volume. After some processing, the bead image stack becomes the 3D PSF for the microscope for the given optical configuration. In this microscopy example, the PSF is treated as shift invariant—the same PSF is assumed to be valid for every point in the volume. This is a fair

assumption for many cases in microscopy [27], but in conventional (macroscopic) imaging the PSF will be shift variant, which adds considerable complexity to the problem. Each point in the volume being imaged will have its own 3D PSF. However, by applying careful attention to scaling in the image formation process (see earlier discussion), our implementation can be reasonably modeled as shift invariant [17].

There are a few approaches by which one can obtain a PSF for use in the 3D deconvolution discussed above. Generally speaking, a PSF can be obtained via either analytic or experimental means. An analytic solution could be derived with the knowledge of the camera geometry and optical path. Although some promising work has been performed towards modeling the PSF for a plenoptic camera [30], [31], it is difficult to fully account for all possible aberrations in a real world imaging scenario. Alternatively, one could take an experimental approach by imaging an approximate point source for a given setup. While such an approach would capture the physical aberrations present, any light used would only be an approximation to a true point source. From a practical perspective, this approach would be tedious to execute precisely and reliably for experiments with changing optical setups, and likely not possible for certain experimental configurations.

The approach used in this research is a hybrid technique. Consider a hypothetical point source of light located at the nominal focal plane of the plenoptic camera. With appropriate placement in plane, a single microlens would be illuminated. That is the point source would illuminate a single spatial sample (one microlens) while the rays strike the main lens at all angles for a complete angular sampling (such that every pixel behind the single microlens is illuminated).

This can be performed on the computer by synthetically “illuminating” the microlens closest to the center of a raw plenoptic image. A raw plenoptic image of a white surface is captured

during a given experiment. Manipulating this image on the computer, the center microlens is left alone while all other microlenses in the raw image are zeroed out. The modified image is saved then processed in LFIT to generate a focal stack with the same values of  $a$  as in the focal stack of the experimental image. This focal stack of the modified raw image constitutes the 3D PSF used.

A vertical cross section of one of the 3D PSFs used for results in this paper is given below in Figure 33. The figure intensity was adjusted for clarity.

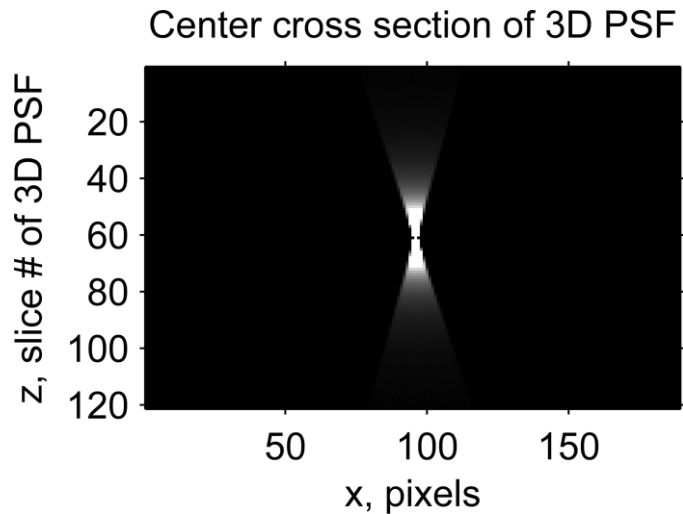


**Figure 33: Vertical cross section of real 3D PSF for a magnification of 0.375**

The nominal focal plane for the experiment is at the center of the  $z$  axis of the above stack in the region of bright slices. At the nominal focal plane, the 3D PSF is only a single pixel, as expected given our hybrid point source simulation discussed above. Moving away from the focal plane, the intensity in a given slice of the PSF remains constant but is increasingly spread out. This can be seen in Figure 34 by plotting the intensity with respect to the slice (depth).



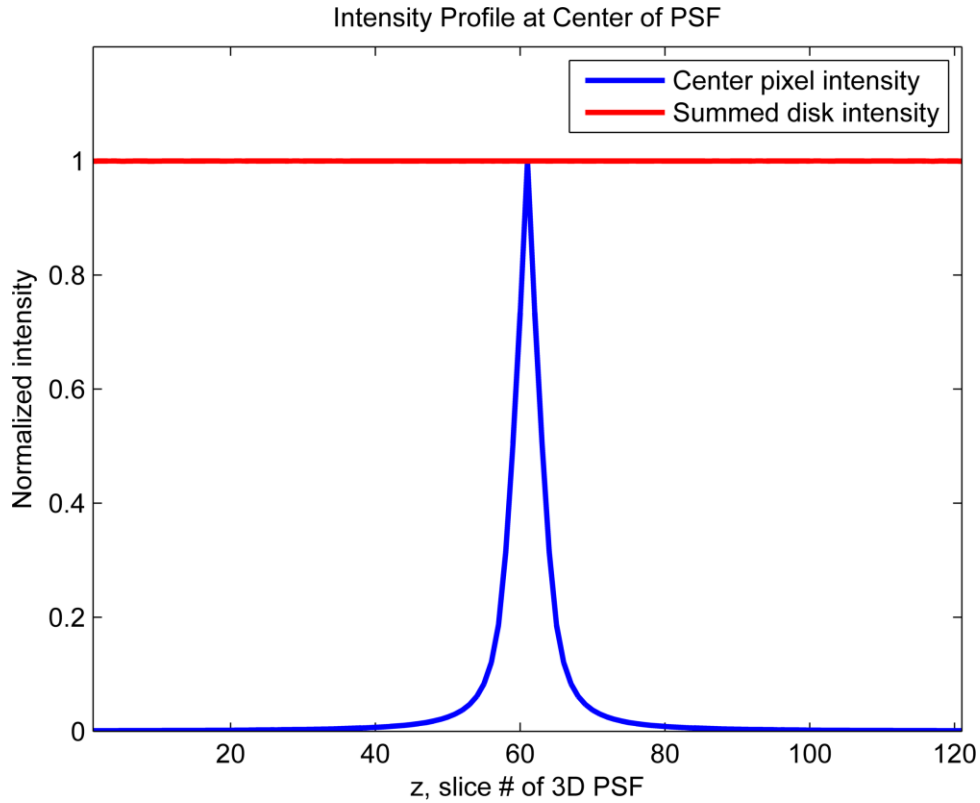


**Figure 34: Intensity profile of PSF with respect to depth**

In the figure above, the red line spanning the entire range of depths is the summed intensity of each slice. That is, summing all of the pixel intensities at a given slice of the PSF yields a value of 1. As noted above, the intensity in a given slice will indeed spread out when moving off the nominal focal plane, but it remains constant throughout the focal stack as confirmed here. Looking at the profile shown by the blue curve, it can be seen that at the nominal focal plane (slice 61), all of the intensity is concentrated in the center pixel plotted. However, the intensity of the center pixel will rapidly decrease when moving to slices off the nominal focal plane. With a technique for modeling the PSF now chosen, it is possible to proceed to the experimental stage.

## V. Characterizing Refocusing Performance

### A. Motivation

Before proceeding to test the performance of the plenoptic camera in occluded environments, it is worthwhile to first consider the performance of the plenoptic camera in an environment free of occlusions. If imaging in an environment with translucent occlusions, there may be a subject of interest at a specific depth. Perhaps a specific piece of hardware in a combustor is being studied, or flames in a specific subset of a larger volume are being investigated. This section seeks to answer the question of where to nominally focus the plenoptic camera to achieve the highest spatial resolution at that desired depth. Alternatively, even if there is not a specific depth of interest in the volume, this section will provide some context for expected performance when refocusing to a variety of depths throughout the volume.

### B. Spatial Frequency Response as a Resolution Metric

To quantify the performance of the plenoptic camera when applying computational refocusing in an occlusion-free environment, it is first necessary to select a metric by which to judge the quality of the output images. In this case, the spatial resolution achievable on the image sensor when at a given refocused plane is the primary parameter of interest. There are a host of algorithms [32] designed to quantify the spatial resolution of imaging systems.

Visual resolution techniques rely on a specific resolution target with a series of bar patterns, such as the 1951 USAF resolution target. This technique requires a human observer to determine the highest visible spatial resolution (smallest resolvable bar pattern) according to a set of rules. While intuitive, this method measures the spatial response only at a single point and is not well suited for computational analysis. Many other methods have been designed specifically for automated testing. The log frequency method uses a sinusoidal bar plot that increases in

frequency across the image, but the method is space inefficient and sensitive to noise. The sine-based spatial frequency response measurement (s-SFR) or Siemens star technique handles noise well but also requires significant space in the image for testing. The dead leaves/spilled coins technique uses randomly-sized stacked circles to create a test with pattern statistics similar to a typical image, but likewise requires generous space.

The most attractive technique is the slanted edge method known formally as the edge-based spatial frequency response (e-SFR). The slanted edge method computes the spatial frequency response via horizontal or vertical slanted edges in an image. The spatial frequency response (SFR) is defined as “a multi-valued metric that measures contrast loss as a function of spatial frequency” [33]. The SFR is analogous to the modulation transfer function (MTF) for monochromatic and linear image processing (as is the case with the monochromatic scientific CCD camera used in this research). The slanted edge technique requires minimal area in the test image and is generally insensitive to noise. Additionally, the slanted edge technique is endorsed by the International Organization for Standardization (ISO) in their standard ISO 12233:2014 where the e-SFR technique is officially defined.

While the interested reader is encouraged to consult the ISO standard for a comprehensive description of the algorithm, an overview of the main components of the slanted edge algorithm are given here. A single slanted edge region of interest (ROI) cropped from a captured image is inputted to the slanted edge algorithm. The edge slope and offset are estimated. The image data is then projected by shifting the data along the edge direction to the edge of the image. A 4x supersampled edge spread function is then formed by accumulating the shifted data. The 1D derivative of the edge spread function is taken to obtain the line spread function. The line spread function is centered and multiplied with a Hamming window to reduce the effect of noise. The

discrete Fourier transform is then taken of the line spread function. The modulus of the discrete Fourier transform is normalized and corrected for bias introduced by the 1D derivative earlier. This result is the e-SFR, the edge-based spatial frequency response.

The fundamental idea behind this technique lies in the fact that the SFR is calculated by taking the discrete Fourier transform of the line spread function. To obtain the line spread function, a camera system can image an edge. However, if the edge is orthogonal to the sampling grid, the resulting line spread function will be sampled at only a few points [34]. By rotating the edge such that it is slanted relative to the image sensor, it is possible to sample the line spread function in a much finer manner.

Some efforts have gone into characterizing aspects of the SFR/MTF of a plenoptic camera. Ng incorporated synthetic MTF analysis in his description of a generalized light field camera [21]. Although not the focus of his synthetic analysis, he did note that for the case of the main lens being focused on the microlens array (as in our camera), the highest spatial resolution should be expected at the focal plane.

A recent paper [35] on characterizing the SFR of light field cameras has some parallels to this work; however, their analysis (purposefully) conducts SFR measurements on the microimages themselves rather than on refocused images. While intriguing, their approach is primarily applicable to superresolution techniques and so-called plenoptic 2.0 implementations [10] that rely on the direct manipulation of microimages to improve output resolution. Their (intentional) neglect of the traditional rendering pipeline makes the application of their results to this work inappropriate. With spatial resolution chosen as the parameter to be measured and the e-SFR as the technique, an experiment was devised to determine the SFR variation with the position of the nominal focal plane.

## **C. Experimental Arrangement**

### *1. Overview and Procedure*

An experiment was set up to quantify how the SFR changes as the distance between the nominal focal plane (physically fixed by the main lens) and a target of interest is varied. As the target is translated in front of and behind the nominal focal plane, the target will become blurred. The raw plenoptic image of the now blurred target is refocused via LFIT back onto the target, and the SFR is assessed. This experiment was designed to experimentally verify the ideal position of the nominal focal plane relative to a depth of interest. That is, to obtain the best SFR, should the camera be focused in front of the target, behind the target, or on the target?

A target with a generous number of slanted edges was designed for use at a variety of magnifications. The rectangular boxes forming the edges were rotated 5 degrees from the vertical axis. The boxes were evenly spaced on the target to provide abundant edges at each magnification setting. The target was printed in high resolution on cardstock, mounted onto a rigid metal backing, and attached to a traverse on an optical table. The plenoptic camera was mounted to the optical table facing the target. A Tamron AF 60mm f/2.0 SP DI II LD IF 1:1 macro lens was selected for use in this experiment as it is well suited for imaging at moderate to high magnifications. A Nikon BR-6 adapter was used to manually set the aperture of the macro lens as it lacks an aperture ring. Two light sources were placed at 45° offsets on either side of the target per the ISO 12233:2014 standard to provide illumination. The experimental setup is pictured below in Figure 35.

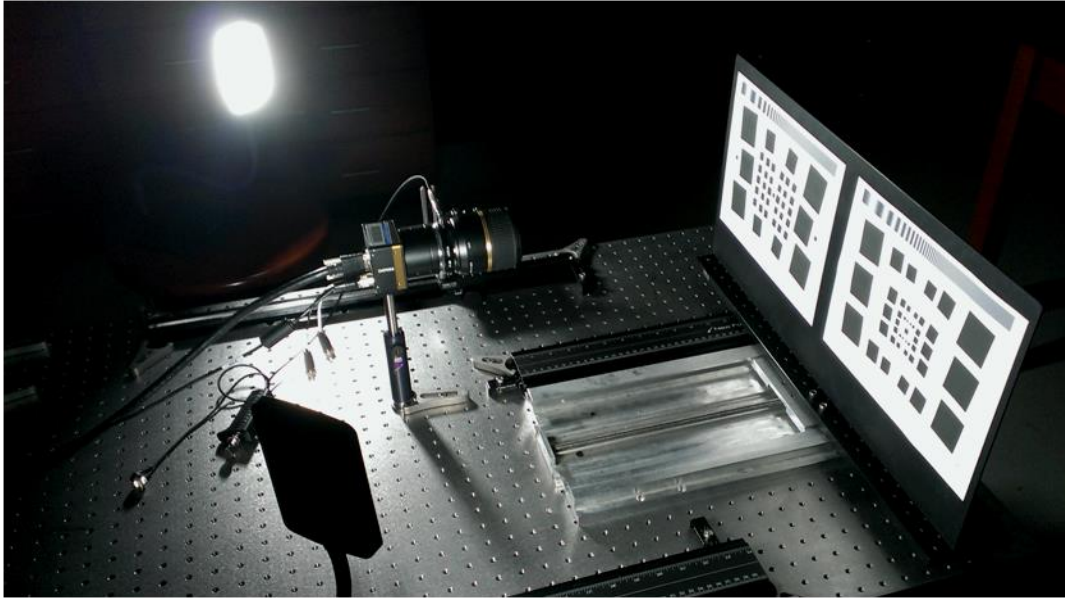


**Figure 35: Experimental setup for refocus performance testing**

The leftmost target in the above figure was used for the tests described here. (The rightmost target was unused in this thesis.) For this set of refocusing experiments, four different nominal focal plane magnifications were identified for testing: 0.250, 0.375, 0.500, and 1.000. These nominal magnification values delineate the four different cases tested. For each case, the nominal focal plane was set via the main lens of the camera then left alone. The target was then translated through a predetermined set of positions, set in increments of the nominal depth of field (DOF). For each DOF increment (position on the traverse), a series of 100 raw plenoptic images were captured then averaged into a single image to reduce the influence of noise on the measurement. The data capture locations can be plotted as below in Figure 36.

### Distance from target to camera vs. distance from nominal focal plane to camera

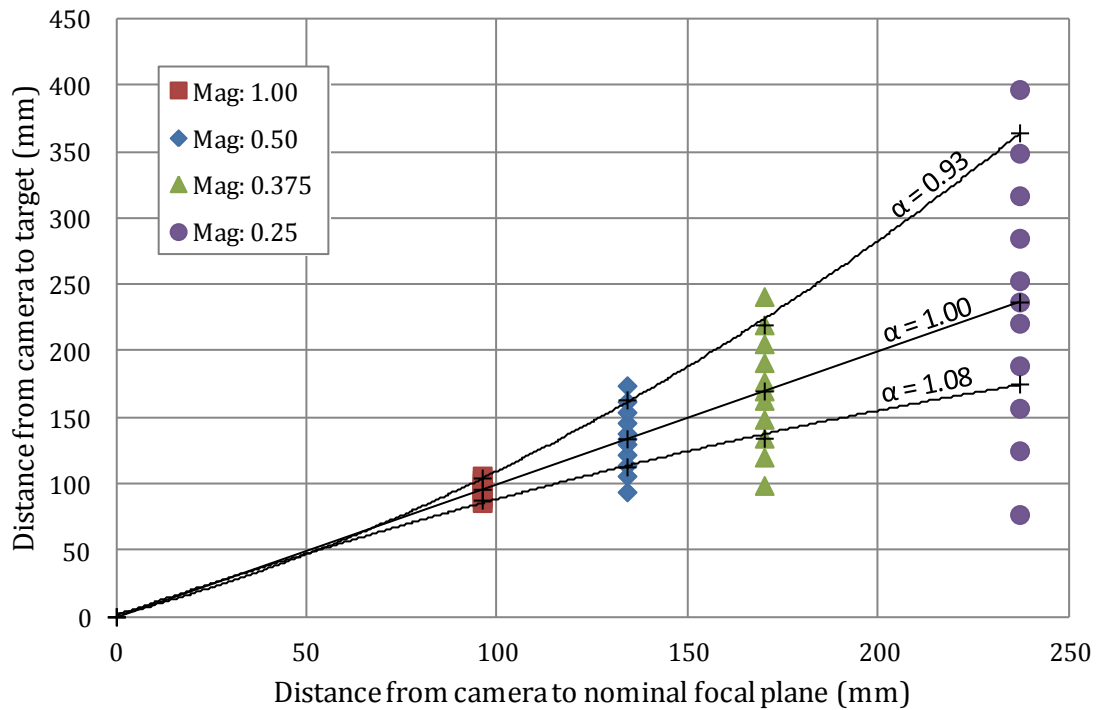


**Figure 36: Plot of refocusing performance experiment data capture points**

The four cases can be seen, delineated by nominal focal plane magnification, where there are four fixed distances from the camera to the nominal focal plane. As stated above, for each case (color-coded magnifications above), the target was translated through a series of positions (vertical groupings) relative to the nominal focal plane of the camera in increments of the nominal DOF. Once the raw images were captured, they were processed in LFIT to refocus the synthetic focal plane onto the target.

Recalling the depth parameter  $\alpha$ , lines of constant  $\alpha$  can be drawn on the above plot. The  $\alpha = 1.00$  line indicates that the target is at the nominal focal plane of the camera. Note that the different target positions (vertical groupings) are intentionally centered about this point. The specific increments (multiples) of DOF used to set the target positions are as follows: -10, -7, -5,

-3, -1, 0, 1, 3, 5, 7, 10. For example, the magnification = 1.000 case has a depth of field of 1 mm. Thus, the first target position relative to the nominal focal plane is  $-10 \times 1 \text{ mm} = -10 \text{ mm}$ .

Because the target positions were determined in increments of DOF, the range of target positions on the traverse was very small for high magnifications which had a narrow DOF. Likewise, the range of target positions on the traverse was large for low magnifications which had a wider DOF. Recall that the DOF is set by Eq. (11) discussed earlier. The circle of confusion will remain fixed while the magnification increases. Also, the f-number required for the maximum allowed microimage size will decrease as magnification increases (see Appendix A and Eq. (31)). This causes the DOF to shrink for increasing magnification.

## *2. Target Selection*

For these refocusing performance testing experiments, it was necessary to select slanted edges from each image to feed to the slanted edge algorithm. This was implemented by hand selecting regions of interest from each image that contained a single edge. This selection process, although manual, followed a regular pattern to ensure that the same edges were selected in each image. In determining the pattern of slanted edges to select, a tradeoff had to be made. Due to the movement of the target relative to the focal plane of the camera in increments of DOF, the field of view on the target changed quite dramatically for lower magnifications.

Because of this, to keep the same edges selected for all the images at a given case (nominal focal plane magnification), it was necessary to limit the selection of slanted edges to the minimum target field of view. In practice, the slanted edges to be used were identified then from the target image with the target positioned closest to the camera (the  $-10 \times \text{DOF}$  increment). For high magnifications, there was little change in the field of view on the target. For low magnifications, many additional edges come into view as the target moves away from the



camera; however, the newly visible edges were not used in order to be consistent with the edge selection throughout the target positions.

In hindsight, this likely introduced a slight bias into the data as the lens used is somewhat softer (less sharp) near the edges of the image. Although the macro lens used was the best available lens for these tests, it was designed for imaging on APS-C sensors which are smaller than the full frame CCD sensor used in this research. As such, there is some vignetting and optical blurring near the edges of the image. This effect and potential bias will be most pronounced at the lower magnifications. While unrelated, it should also be noted that the necessary use of the Nikon BR-6 aperture control ring acts like a small extension tube, so the lens is also being used in a (slightly) off-design condition in this way as well.

With the above caveats noted, below are the reference images used for slanted edge selection. To add context to the change in the field of view, the base refocused image is the target at its maximum distance from the camera (DOF x 10). Overlaid on top of that image is the refocused image with the target at its closest distance to the camera (DOF x -10). The images were scaled such that their features matched. Note that both images will be somewhat blurry as they are from refocused images of the target when it was an order of magnitude outside the original DOF. The slanted edges are numbered for convenience in selection. A total of 48 regions of interest were selected for each case, although generally only the numbered edges in the below figures were used in the analysis.

Below in Figure 37 is the reference slanted edge selection image for a magnification of 0.250.

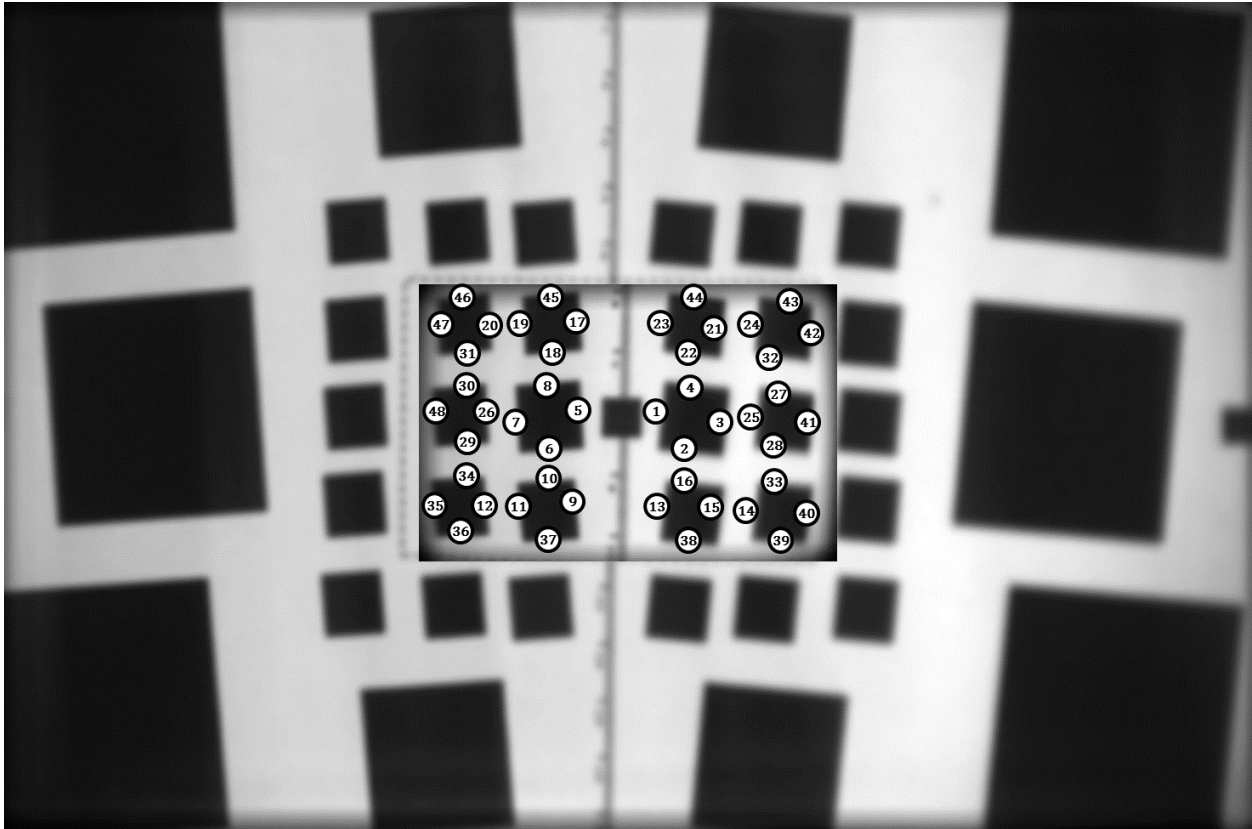


**Figure 37: Slanted edge selection reference image for case 1, magnification of 0.250**

Note the dramatic change in field of view for this case. Biases due to lens softening would be expected to be the highest for this case. A total of 48 slanted edges are numbered in this figure and the next based on the number of slanted edges in the minimal field of view.

Below in Figure 38 is the reference slanted edge selection image for a nominal focal plane magnification of 0.375. The field of view change is less dramatic for this case.

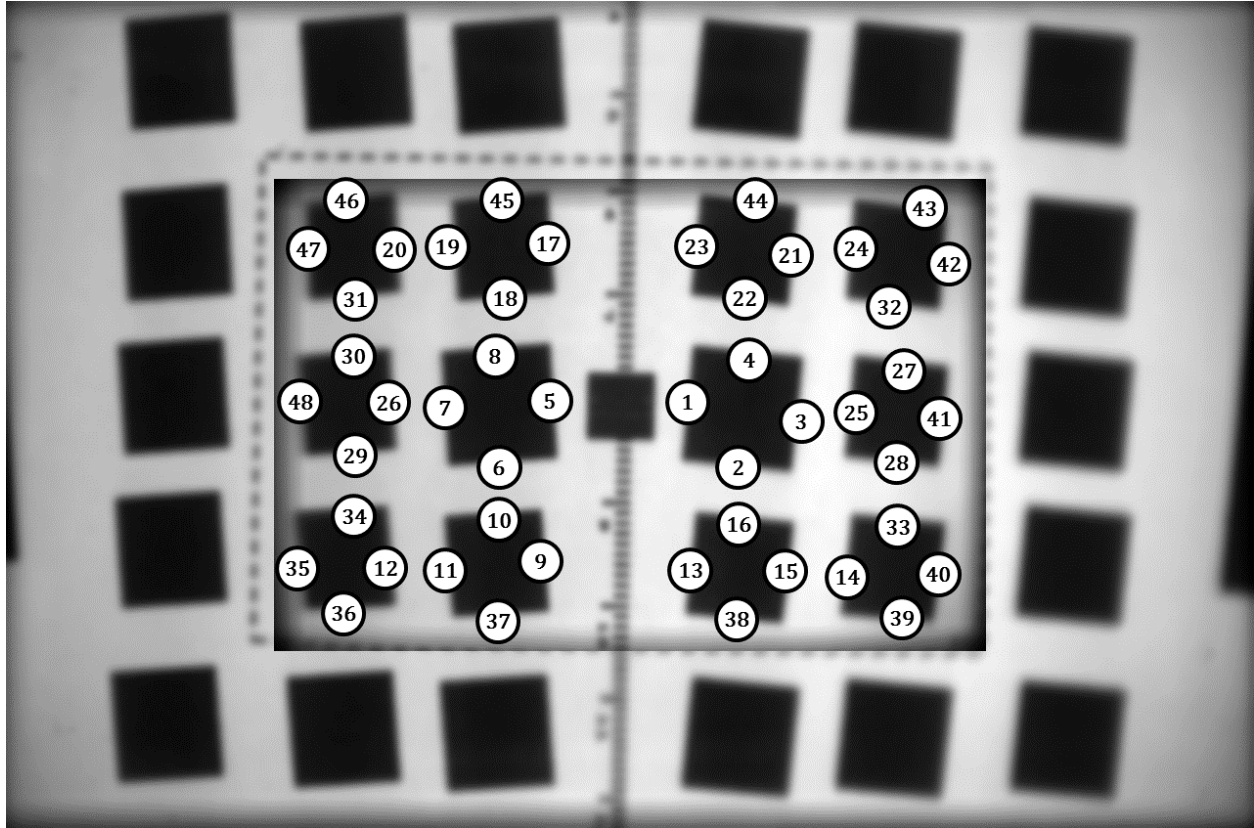


**Figure 38: Slanted edge selection reference image for case 2, magnification of 0.375**

The same slanted edges associated with each rotated box were selected in the same pattern in both Figure 37 and Figure 38.

The reference slanted edge image for case 3 and a nominal focal plane magnification of 0.500 is given in Figure 39. Note that while the previous two figures used the same 48 slanted edges, the minimal field of view is now such that only 34 slanted edges can be selected.

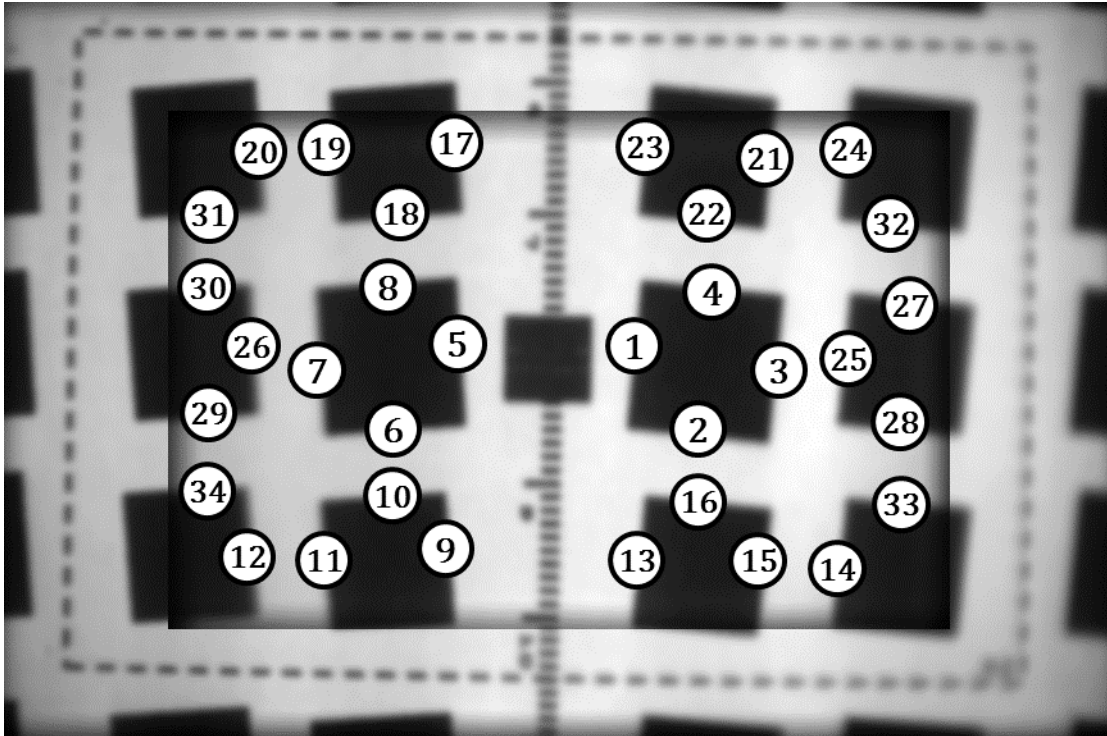


**Figure 39: Slanted edge selection reference image for case 3, magnification of 0.500**

Finally, for the nominal focal plane magnification of 1.000, only 15 slanted edges are available for selection as shown below in Figure 40. Note that to obtain additional measurements, the long slanted edges were broken up into segments in the selection process.

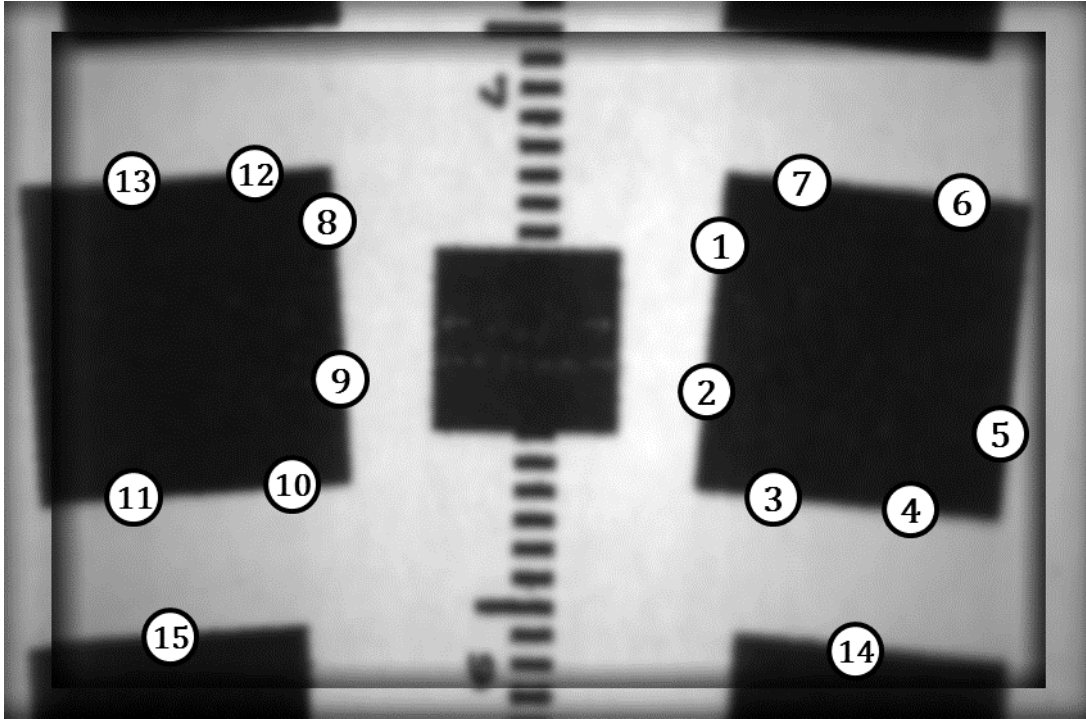


**Figure 40: Slanted edge selection reference image for case 4, magnification of 1.000**

While it was advantageous having a single target to minimize experimental variables, at this high magnification the number of slanted edges was lower than the other cases. Compared to the lowest magnification case, this case has many slanted edges nearer the boundaries of the image as the field of view change is significantly less. This could create biases as discussed earlier.

## **D. Results**

### *1. Processing Procedure*

With the above experimental setup complete, all 4 cases were evaluated with 100 raw plenoptic images being captured at each target position and averaged. For each averaged image, LFIT was used to synthetically refocus the focal plane to bring the target into focus. Up to 48 slanted edges were hand selected in each refocused image following specific patterns outlined above. The MATLAB code provided in support of the ISO standard was adapted for batch

processing and incorporated into a custom test script. Each slanted edge in a given image was passed to this algorithm and the SFR for that edge was computed and stored. The frequency at which the SFR was reduced to 0.5 was also calculated and noted at this stage.

This resulted in a wealth of data, with separate SFR curves associated with each slanted edge at each target position for each magnification case. Several measures were taken to ensure that the SFR curves used in the analysis were of high quality. While the SFR function has a built in status flag to indicate algorithm failure, this function was modified to also trigger the failure status flag when the slanted edge algorithm detected an abnormally high edge slope—an indicator of poor results. Constraints were also set based on the maximum response and standard deviation of each response curve. The standard deviation constraints were set qualitatively, as clear groupings of each set of curves emerged when plotting every slanted edge for a given case and position. In these ways, poor quality and outlier SFR curves were filtered out of the data set as necessary. Selected results are given below.

## *2. Selected Plots and Discussion*

Limiting the scope to a single magnification for visualization purposes, the change in SFR with target depth can be plotted as below in Figure 41. Gaussian curves were fitted with the up to 48 SFR curves generated from the slanted edges associated with each target position.

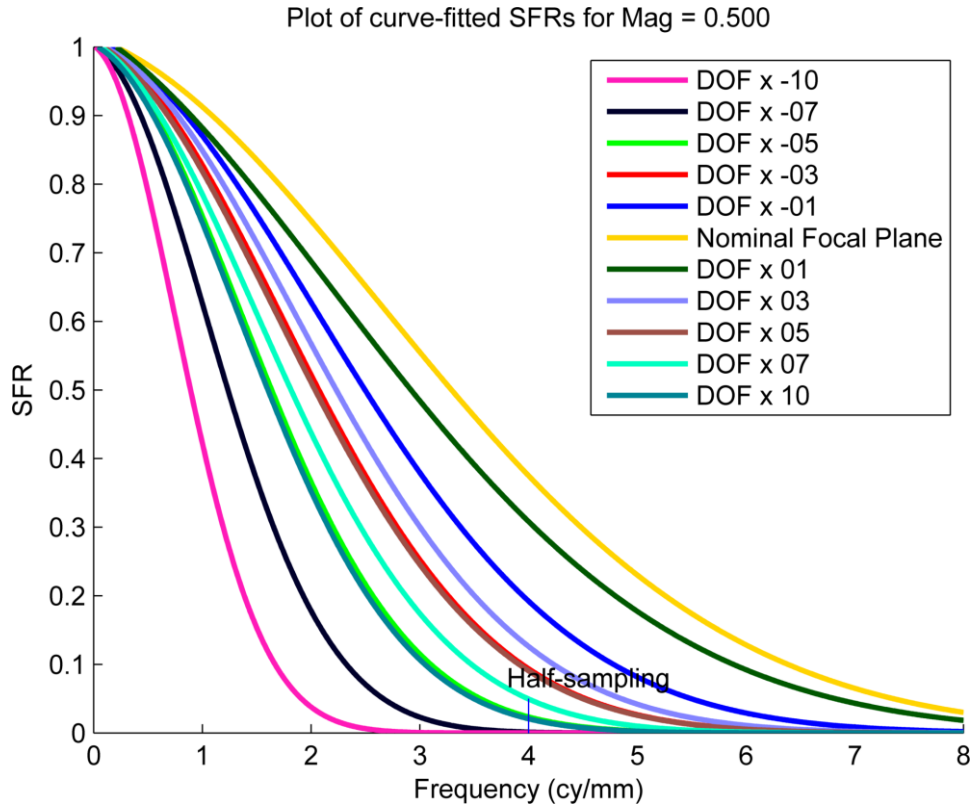


**Figure 41: Curve-fitted variation of SFR with target position at a magnification of 0.500**

Recall that the SFR is the spatial frequency response, defined as the “relative amplitude response of an imaging system as a function of input spatial frequency” [33]. Thus, at low spatial frequencies, the response is quite high regardless of target positions. This indicates that large structures in the image will be visible regardless of target position here. However, as spatial frequency increases, the response drops. This makes intuitive sense; in a slightly out of focus image, large features in the image (say a person) remain resolvable while fine details (say a pattern on their shirt) become illegible quickly. Observe that the frequencies measured here are the frequencies measured on the image sensor (that is, in the output image); the measured frequencies are not the physical frequency on the target. While this follows convention, it bears noting here.

The target positions are labeled in the legend, where DOF x -10 refers to the closest target position and DOF x 10 refers to the most distant target position from the camera. More specifically, since the DOF for a refocused image at a nominal focal plane magnification of 0.500 is 4 mm, the closest target position is -40 mm and the farthest target position is +40 mm from the nominal focal plane. As an aside, note that a perspective view image of the scene would have a DOF of almost 68 mm.

Examining the curves in the above figure, the SFR is clearly the highest when the target is at the nominal focal plane. The next two highest responding curves are when the target is  $\pm 1$  DOF increment from the nominal focal plane. In general, with increasing distance off the focal plane, the SFR will be reduced. This trend can be seen when examining the same edge at different target positions for a fixed nominal magnification case as in Figure 42. Note that due to the manual selection of edge regions of interest and the changing field of view, each cropped edge region varied slightly in dimensions.

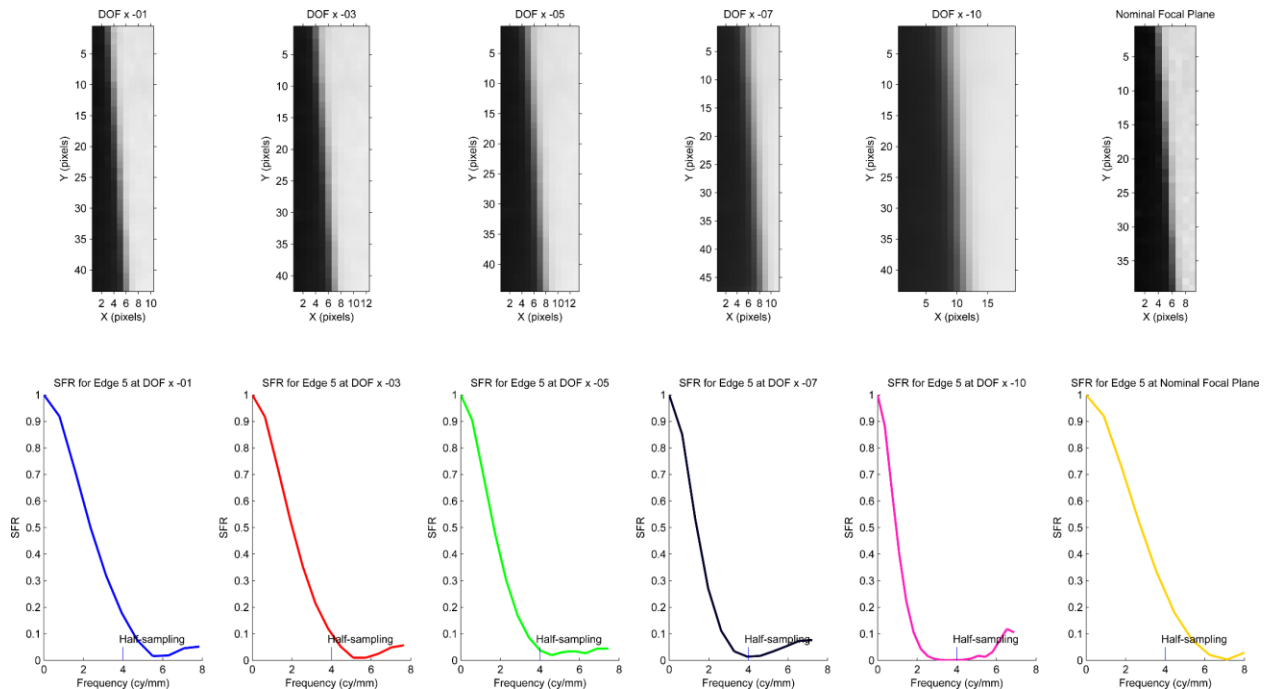


**Figure 42: Edge and SFR comparison at magnification = 0.500 and multiple positions**



In the above figure, edge 5 was chosen from Figure 39 for inspection. For the target positions of DOF x -01, -03, -05, -07, -10, and the nominal focal plane, the edge and its associated SFR curve are plotted above in Figure 42. Note the large SFR response for the sharp nominal focal plane edge at the right of the figure. Examining the other edges, from left-to-right the distance from the nominal focal plane is increasing, and the edges become increasingly blurred.

In Figure 43, the Gaussian curve-fitted SFR is plotted for all the target positions at a magnification of 0.250.

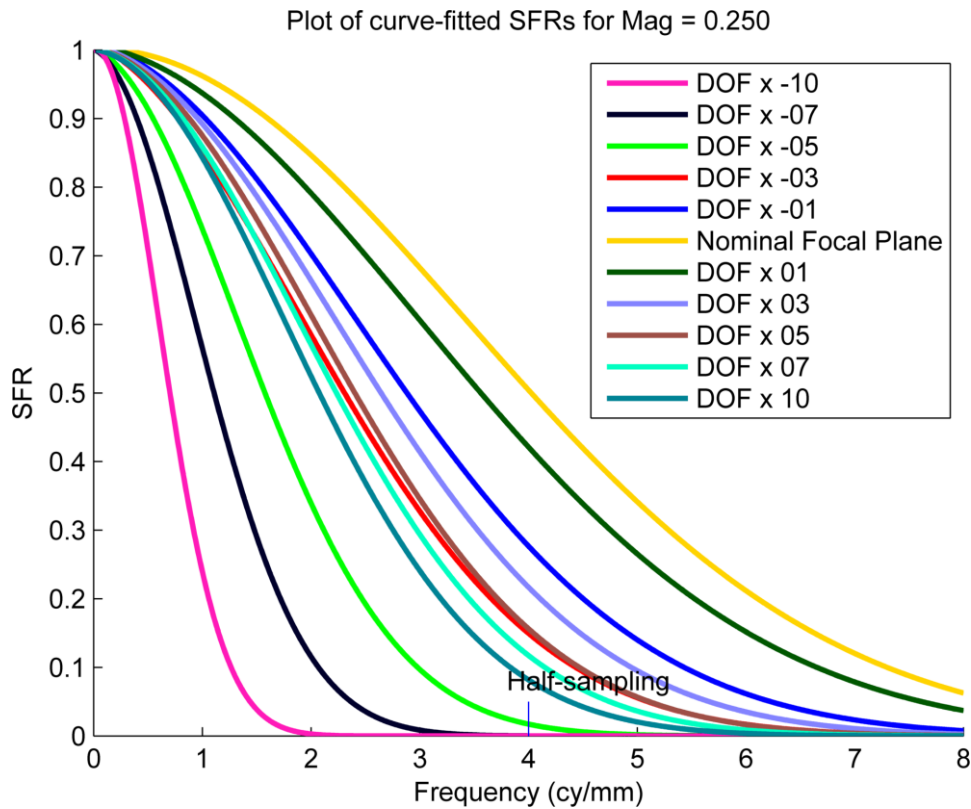


**Figure 43: Curve-fitted variation of SFR with target position at a magnification of 0.250**

The same general trends are observed as in Figure 41 for the magnification of 0.500 case. The SFR curve at the focal plane easily exceeds the response generated by the other target positions.

The next two highest responding curves are the DOF x 01 and DOF x -01 curves which are the next closest target positions to the nominal focal plane.

Below in Figure 44 is the same SFR plot, now shown for a magnification of 0.375.

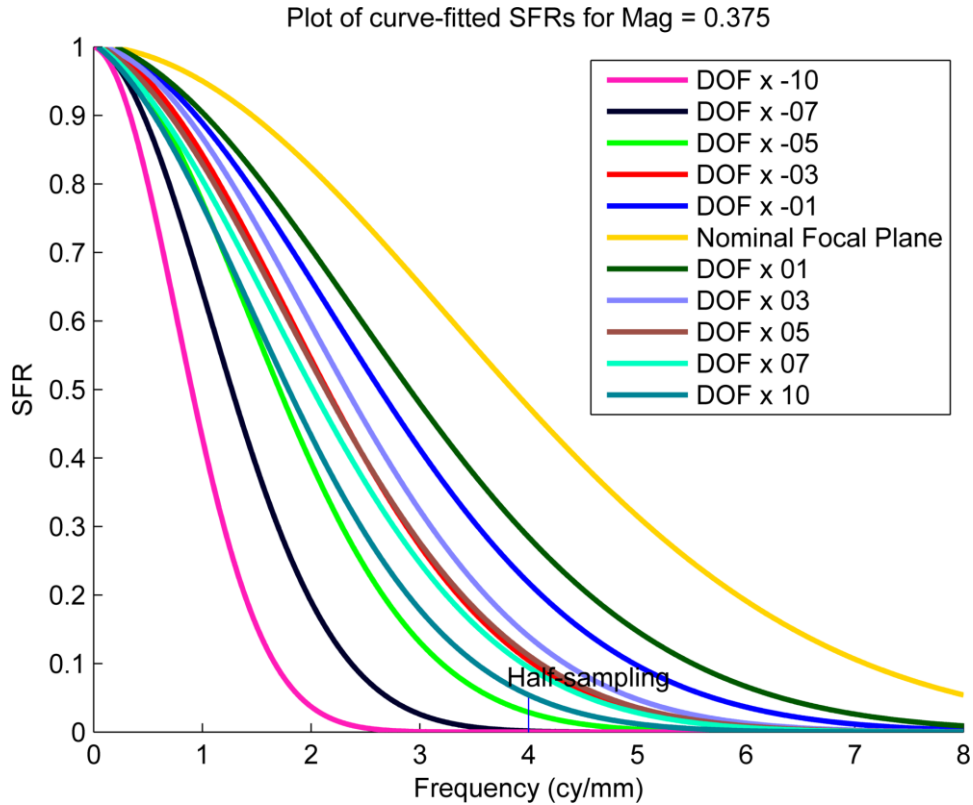


**Figure 44: Curve-fitted variation of SFR with target position at a magnification of 0.375**

The nominal focal plane position has a higher relative SFR in this case compared to the other target positions. Again, similar trends are observed as in the previous figures.

Finally, the 1.000 magnification case is given in Figure 45.

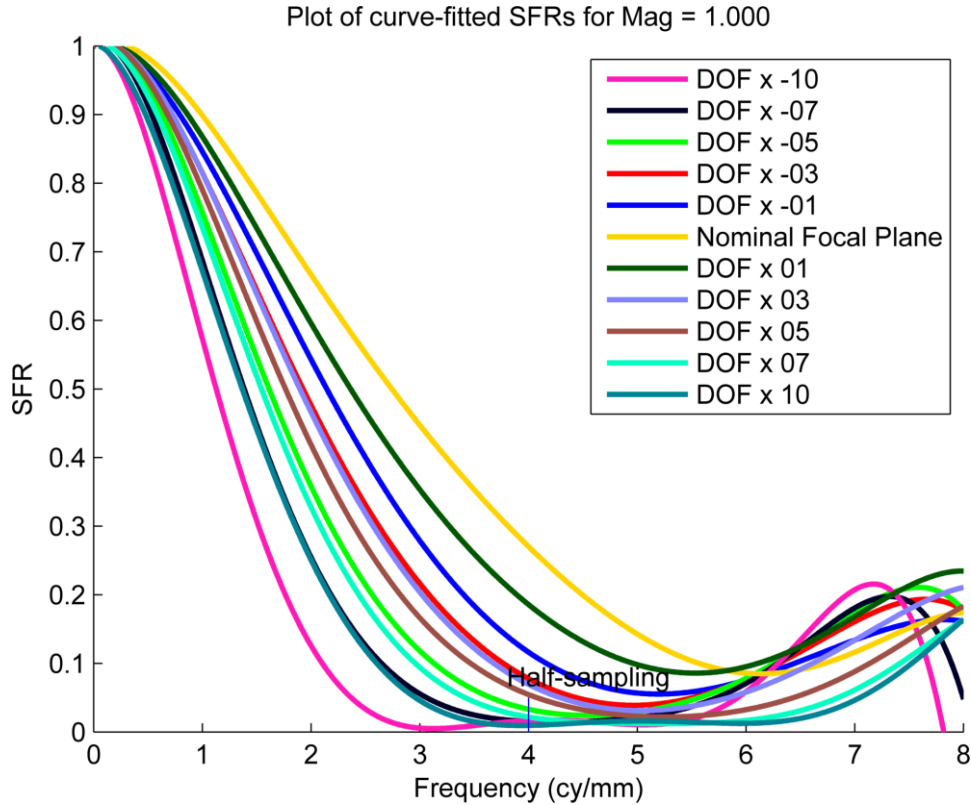


**Figure 45: Curve-fitted variation of SFR with target position at a magnification of 1.000**

Note that for this plot, the Gaussian curve-fits did not track well with the experimental data due to higher than expected response above the half sampling frequency. For this reason, a 6<sup>th</sup> order polynomial was used instead. While the polynomial fit here gives somewhat poor results above a frequency of about 6 cycles per millimeter, it matches the measured data well in the lower frequencies of interest.

This can be seen by examining individual DOF increments. In Figure 46 below, the SFR is plotted for a single DOF increment and magnification of 1.000.

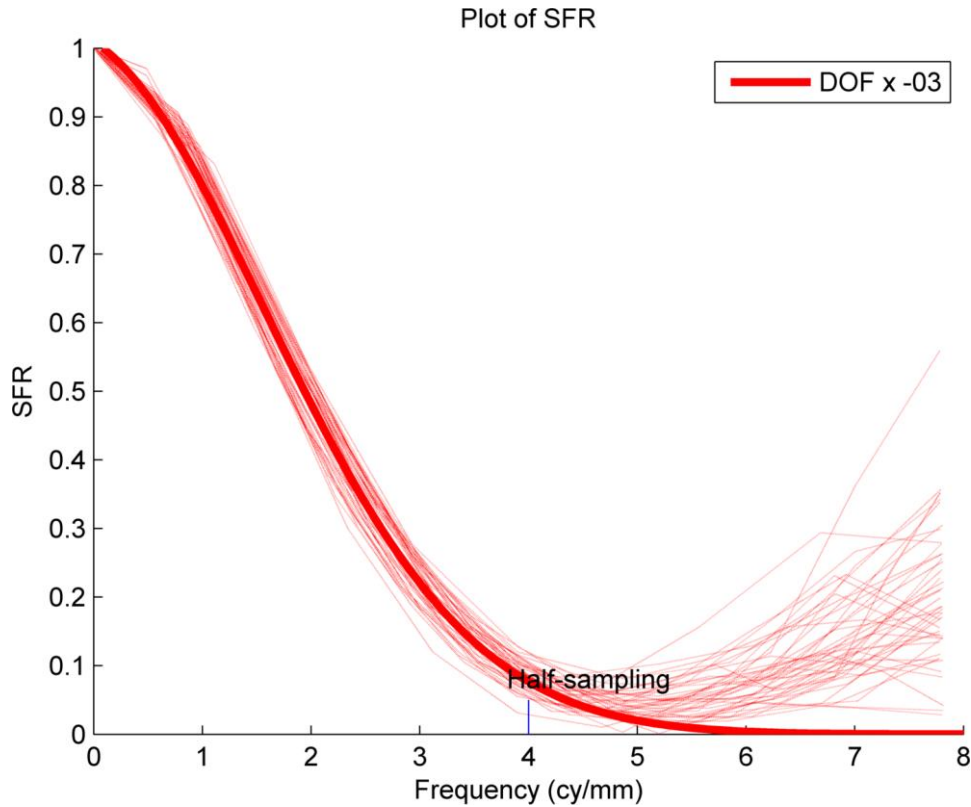


**Figure 46: SFR for DOF x -03 and magnification = 1.000 with Gaussian curve fit**

The smaller lines correspond to the individual SFR curves calculated for each edge in the image. For this particular case, the Gaussian curve in bold still manages to achieve a reasonably good fit. Note however the pronounced response in the measured data beyond the half sampling frequency. This response can be better captured by a 6<sup>th</sup> degree polynomial curve fit. While unnecessary here, this is required for a case like Figure 47 where the DOF x 01 increment is shown.

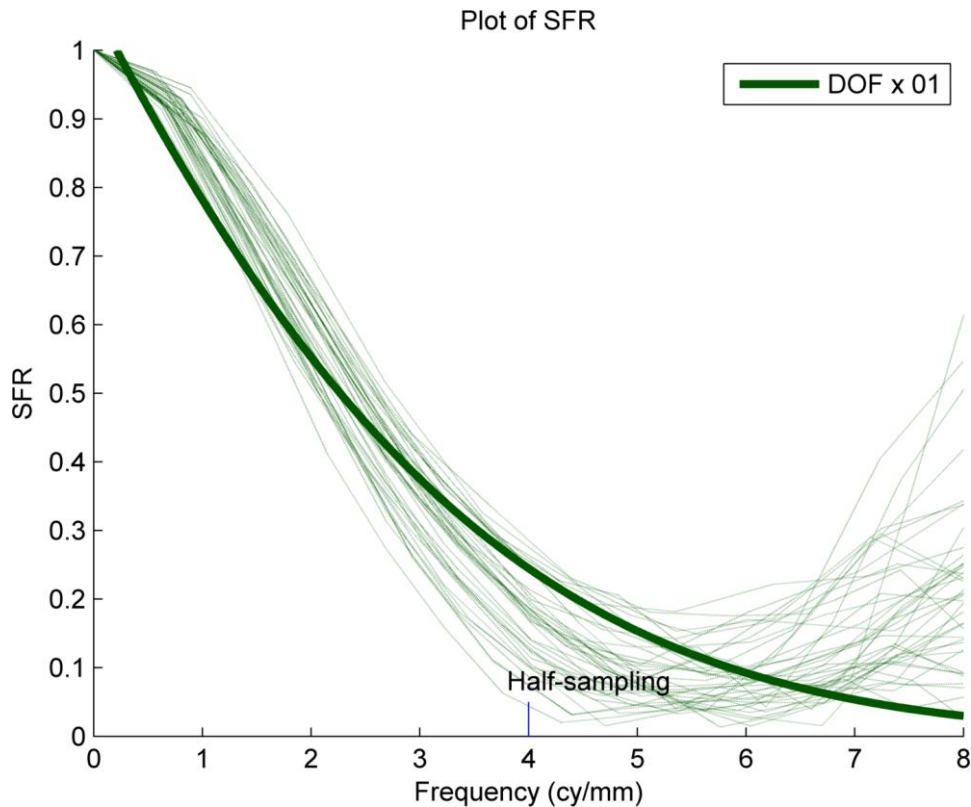


**Figure 47: SFR for DOF x 01 and magnification = 1.000 with Gaussian curve fit**

Here the Gaussian curve fit fails to follow the actual plotted data. In this case a polynomial curve fit is necessary to avoid skewing any conclusions drawn from the curve fit plots. It should be noted that the curve fits were necessary because the SFR algorithm returned SFR points (on the y-axis) at varying, inconsistent frequencies (on the x-axis), such that the curves could not be simply averaged together.

The dominance of the nominal focal plane response can be seen when plotting the SFR50 points for each target position across all 4 magnification cases. Remember that the SFR50 is the frequency at which the SFR drops to a 0.5 response; it is a good indicator of the overall sharpness of the image and commonly used to summarize the results for an entire SFR curve. The SFR50 is plotted below as a function of magnification in Figure 48

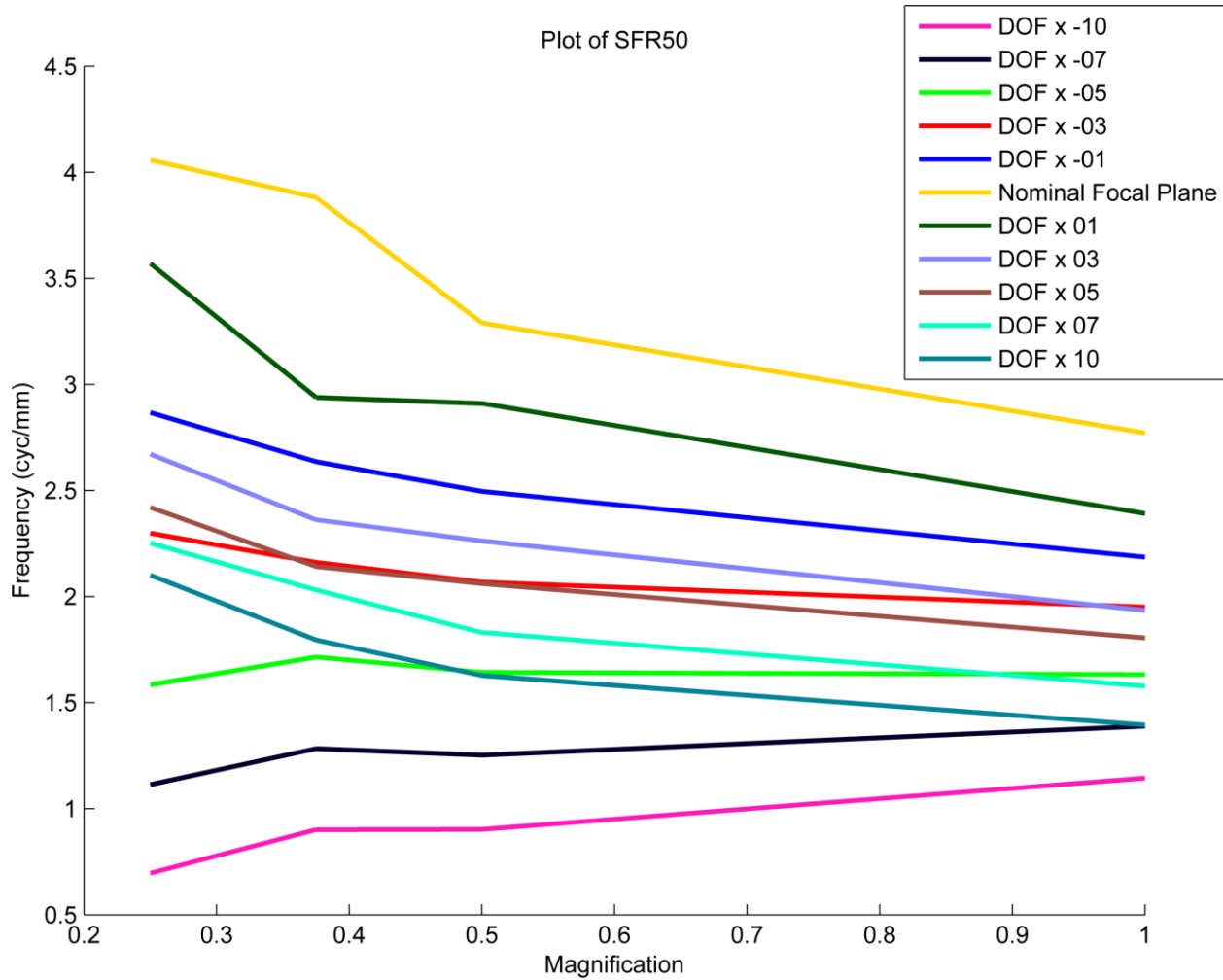


**Figure 48: SFR50 as a function of magnification for refocus testing**

Note that only 4 nominal focal plane magnification cases were tested: 0.250, 0.375, 0.500, and 1.000. Even so, it is clear that the trends observed in Figure 41 hold for other magnifications. When the target is located at the nominal focal plane of the camera, the highest SFR is recorded. The lowest responses come from targets located far off the nominal focal plane of the camera. This experimentally validates that to obtain the highest SFR in an output image, the nominal focal plane of the camera should be set as close as possible to a depth of interest in a given experimental volume.

Interestingly, the response at the sensor trends downward with increasing magnification. A few possible factors could play a role in this trend. The SFR being measured is a function of the entire imaging chain. The target itself, the lens, the camera CCD sensor, and the processing in LFIT all will have some impact on the ultimate SFR. It could be that as the magnification increases, irregularities in the printed target edge become magnified and thus reduce the SFR as the edge is no longer as sharp. The performance of the lens itself is also an open question; recall the earlier discussion regarding possible impacts on image quality due to the lens selection.

One final observation can be made regarding the SFR curves above. Note that the highest responding SFR curve corresponds to the nominal focal plane position at a magnification of 0.250 as seen in Figure 48. This highest responding curve for the plenoptic camera can be compared to the predicted SFR curve for a hypothetical conventional camera with pixels the same size as the microlenses used in our plenoptic camera. For such a camera with rectangular pixels, the geometric SFR is given by the formula below in Eq. (17) per [36].

$$SFR(\omega) = \frac{\sin(\omega\delta)}{(\omega\delta)} = sinc(\omega\delta) \quad (17)$$

The frequency is  $\omega$  and the hypothetical pixel pitch (equal to the plenoptic microlens diameter of 0.125 mm) is given by  $\delta$ . Plotting this function with the highest responding plenoptic SFR case yields Figure 49.

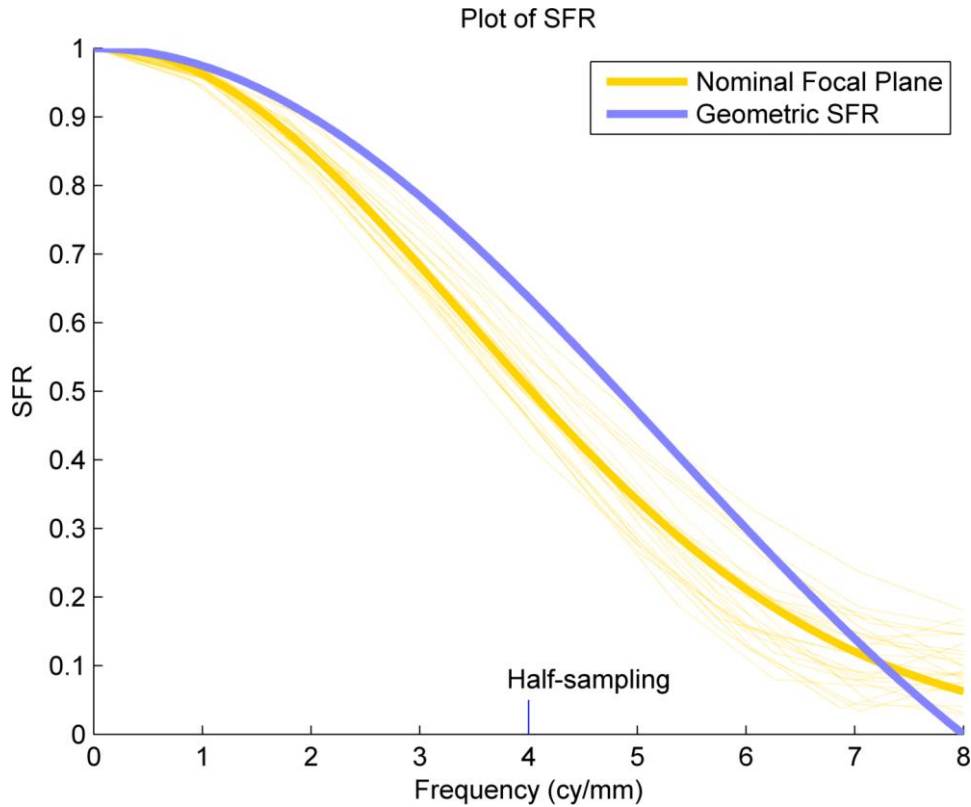


**Figure 49: Geometric MTF compared to nominal focal plane SFR for magnification = 0.250**

Examining the figure above reveals that a perfect conventional camera with pixels equal in size to the microlenses in our camera would have a slightly higher responding SFR curve. Several factors could explain this difference, including the interpolation that occurs in LFIT, possible aberrations in the microlens array, or the performance of the main lens with this setup. The yellow curve for the plenoptic camera above does slightly exceed the geometric MTF at very high frequencies, but this is solidly in the aliased region and could be treated as a spurious result. This provides context for the performance of our prototype plenoptic camera compared to an ideal case.

### *3. Nyquist and Supersampling Effects*

Before proceeding further, several other interesting observations can be made about the captured data above. Returning to Figure 41, it can be seen that there is a half-sampling



frequency indicated on the frequency axis. This half-sampling frequency is referring to the Nyquist frequency. The Nyquist frequency is given below by Eq. (18).

$$\text{Nyquist frequency} = \frac{1}{2\delta} \quad (18)$$

Note that  $\delta$  is the sampling rate of the imaging system. As noted earlier in a discussion regarding the circle of confusion, the spatial sampling rate for the plenoptic camera is given by the microlens diameter (or spacing). For the camera used in this research, the Nyquist frequency (half-sampling frequency) is given by Eq. (19).

$$\text{Nyquist freq} = \frac{1}{\left(2 \frac{\text{pixels}}{\text{cycle}}\right) \left(0.125 \frac{\text{mm}}{\text{pixel}}\right)} = 4 \frac{\text{cycles}}{\text{mm}} \quad (19)$$

The Nyquist frequency is the maximum frequency that can be captured at a given sampling rate without aliasing. Aliasing occurs when a continuous function is undersampled; high frequency components of the function being sampled corrupt lower frequencies in the sampled signal. In images, this can lead to artifacts such as jagged edges [25]. Note that the SFR technique used in this section is indeed capable of measuring frequencies above Nyquist [33]. Thus the measured signal response above the Nyquist frequency in Figure 41 will lead to some aliasing in the output images.

One way to reduce sampling artifacts is to increase the rendering sampling rate by supersampling. That is, by evaluating the  $(s, t)$  and  $(u, v)$  coordinates on a finer grid in the refocusing algorithm, the aliasing in the output image can be reduced. This can be observed qualitatively and quantitatively by examining a single representative edge from the above data set. For the magnification of 0.500 case, with the target positioned 1 DOF increment in front of the nominal focal plane, the SFR can be plotted as in Figure 50.

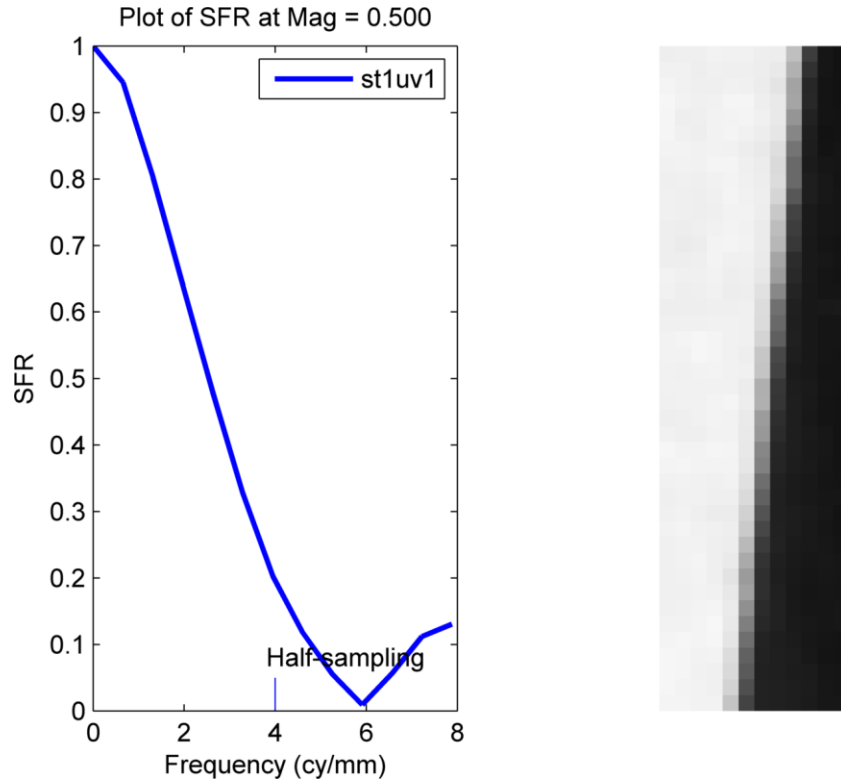


**Figure 50: Non-supersampled edge with corresponding SFR at magnification of 0.500 and target at -1 DOF**

The figure was generated without supersampling in either spatial  $(s, t)$  or angular  $(u, v)$  coordinates. Note the pixelation along the edge and the response above the half-sampling (Nyquist) frequency. Because the edge is a high frequency feature spatially (rapid transition from white to black), the aliasing is manifested along the edge. The sampling rate in the image rendering process can be increased by evaluating the refocusing algorithm on a finer  $(s, t)$  grid as below in Figure 51.

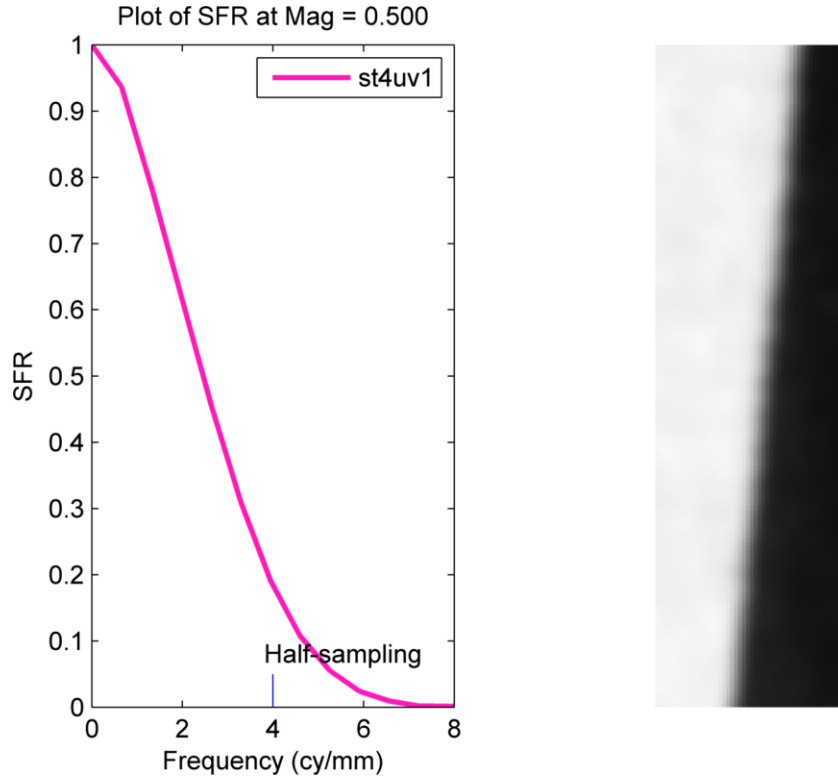


**Figure 51: Supersampled 4x (s,t) edge with corresponding SFR at magnification of 0.500 and target at -1  
DOF**

All other parameters were kept identical to Figure 50. The spatial supersampling has reduced the response above the half-sampling frequency, particularly above 6 cycles per mm. From a qualitative perspective, the edge is now much smoother and no longer jagged. Although some response remains above the Nyquist frequency, this encountering of aliasing is not entirely unexpected. Ng noted that the microlens array and image sensor are ineffective in completely low-pass filtering the incoming light [21]. He also noted the anti-aliasing effect of refocusing, which can be observed in Figure 41 where targets off the focal plane have a lowered response above the Nyquist frequency. For a further discussion of supersampling, refer to Appendix D. Finally, while many conventional consumer cameras have an anti-aliasing filter to low pass filter

out the excessively high incoming frequencies, note that the plenoptic camera used in this research was not outfitted with such a filter.

In light of the above discussions, the refocusing experiments conducted here indicate that to record the greatest spatial resolution with the plenoptic camera, the nominal focal plane of the camera (as set by the main lens) should be fixed upon the proposed depth of interest. With this in mind, a new set of experiments were devised to investigate the performance of the plenoptic camera and the effectiveness of the deconvolution algorithm in an environment containing translucent occlusions.

## VI. Occlusion Testing

### A. Introduction

With the refocusing tests above complete, the next step is to consider the performance of the plenoptic camera and the deconvolution algorithm in an environment representative of real world conditions. In contrast to the previous refocusing experiments above where the camera had an unobstructed view of the target, these experiments take place in an occluded environment. Ultimately this thesis is investigating the viability of the plenoptic camera for imaging in environments containing translucent occlusions. One of the most directly applicable examples of translucent occlusions is chemically reacting flows, or more specifically, flames. Towards that end, several qualitative examples of deconvolution applied to flame volumes will be given later; however, for reasons given below, the quantitative experiments in this section used a smoke machine and laser sheet to create a highly controllable translucent occlusion between the camera and target.

### B. Experimental Arrangement

A similar setup to the previous refocusing experiments was used. The plenoptic camera was again fixed to the optical table, facing an identical slanted edge target mounted on the linear traverse as in the refocusing experiments prior. (Note that the right target visible in Figure 35 was switched out for the one visible in Figure 52.) A Laserglow C53150XSX continuous-wave 532 nm laser was then mounted on a 3D linear translation stage for initial positioning. This laser is capable of over 150 mW of output power, although a waveplate and polarizing beamsplitter was used to attenuate the output.

On a separate traverse, optics for forming a laser sheet were mounted to permit repositioning of the laser sheet without requiring further adjustment of the laser's 3D linear translation stage.

A smoke machine was also incorporated into the setup so that smoke could be introduced into the imaged volume. With sufficient amounts of smoke, the laser sheet acts as a translucent occlusion. The actual experimental setup is shown below in Figure 52.

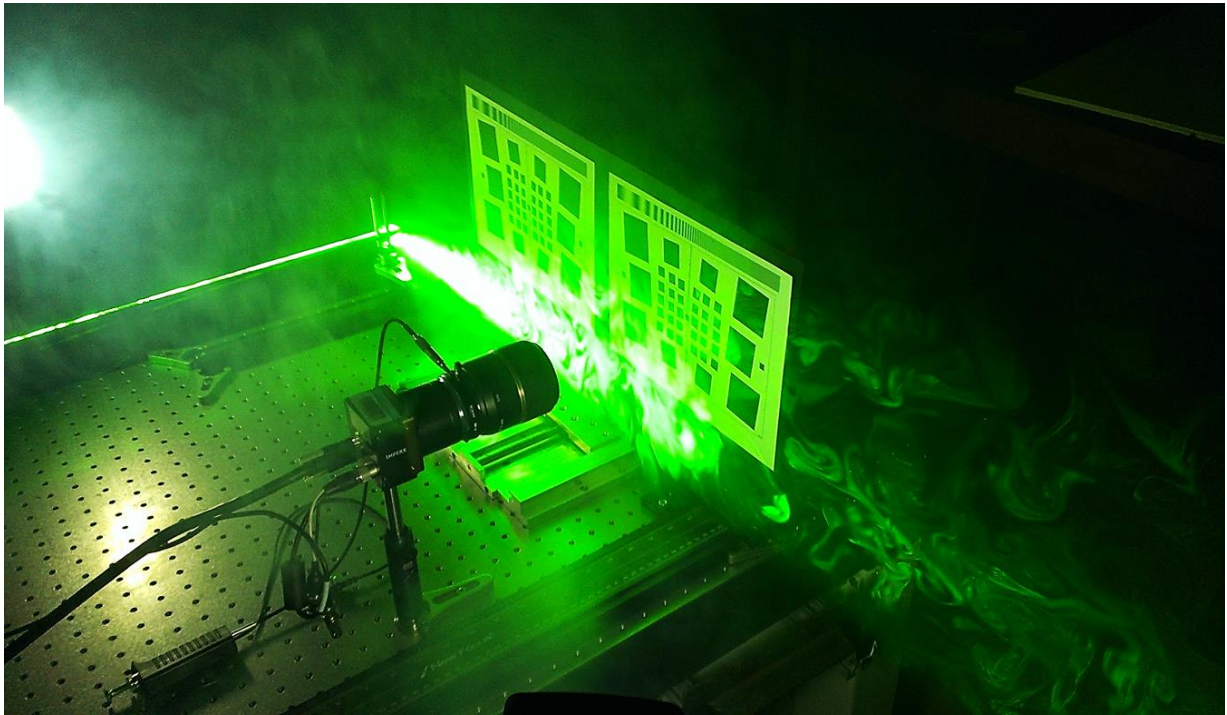


**Figure 52: Experimental setup for occlusion testing**

Four main cases were examined, again delineated by the magnification at the nominal focal plane: 0.250, 0.375, 0.500, and 1.000. For this experiment, the camera was fixed on the optical board, and the target was translated on the traverse to place it at the nominal focal plane for each magnification case. For a given magnification, the target remained fixed at the focal plane and the laser sheet (on a separate traverse) was moved in increments of the DOF relative to the target. The DOF increments, measured from the nominal focal plane at the target, were as follows: -01, -03, -05, -07, and -10. For example, the magnification = 0.250 case has a depth of field of 16 mm. Thus, the first occlusion position relative to the nominal focal plane is  $-1 \times 16 \text{ mm} = -16 \text{ mm}$ .

For each occlusion position, 30 occlusion images were captured sequentially over a period of approximately 15 seconds with the continuous wave laser active and liberal use of the smoke machine. As a consequence of using laser-sheet-illuminated smoke as the occluder, there was noticeable variation in the amount of degradation due to the smoke present in output occlusion images. Although the smoke machine was consistently used in such a way as to achieve maximum smoke in the imaged volume, the occlusion images were averaged after the fact in an attempt to damp out the noted variations between the tests. The laser was then deactivated and time was given to let the smoke clear, and sequences of clean images were also captured and later averaged to reduce the influence of noise on the measurement.

Extensive consideration was given to using an actual flame, but a number of practical considerations stymied this effort. At low magnifications, it would be difficult to create a flame sheet of sufficient dimensions to fully fill the field of view of the camera. Conversely, at high magnifications, the working distance between the camera, target, and flames would be such that both the target and the camera would be at risk of damage from the flames. Additionally, a flame sheet large enough to fill the field of view of the camera would be susceptible to depth variability as it flickers towards and away from the camera with the ambient air currents in the lab. The laser sheet and smoke approach allowed for precise control of the illuminated region. By avoiding reflections and carefully controlling the positioning of the laser sheet, much of the risk to the camera was mitigated.

It should be noted that the nature of this translucent occlusion was primarily low-frequency in nature; that is, individual flow structures in the smoke (while visible in Figure 52) were not directly observed in individual images captured during this experiment. This was a consequence of the decision to use the laser sheet and smoke machine; however, given a uniform flame sheet

large enough to completely fill the field of view, a similar (albeit likely more intense) smooth contrast degradation would be expected. The applicability of the results in this section naturally hinge on the desired application. The fact that the translucent occlusions as described here are primarily a quasi-uniform contrast degradation make this section most directly applicable to imaging in an environment degraded by smoke, fog, or large smooth flames. Other environments, such as a combustor inside a jet engine, could be dominated by a mix of small, turbulent flames with significant spatial variability in the field of view. The performance of the 3D deconvolution algorithm in such a mix of both large blurred flame structures along with smaller fine flame edges is better assessed by the qualitative results in the next section: Example Deconvolution Results as Applied to Flames.

## **C. Quantitative Approach**

### *1. Inadequacy of Slanted Edge Method*

While the slanted edge SFR approach was used for the refocusing experiments previously, the testing in this occluded environment required a new metric. Although a slanted edge target was again used for these occlusion experiments, the ISO 12233:2014 standard defining the slanted edge testing was designed for quantifying the ideal performance of digital cameras in a strictly controlled test environment. The e-SFR algorithm was not designed for quantifying image degradation due to external occlusions, nor does the standard make any provision for such testing.

Although the slanted edge (e-SFR) technique is a powerful tool, it was determined to not be an appropriate metric for the occlusion testing. The occlusion experiment described in this section using the smoke machine and laser sheet was successful in partially occluding the target. However, actual structures in the smoke were not observed in images captured by the plenoptic



camera. The effect was one of a general contrast degradation (“washing-out”) of the occluded image compared to the clean reference image. No blurring of the edges was observed due to the translucent occlusion.

As a trial, the SFR algorithm was applied to edges in the occluded images using a similar procedure as in the refocusing experiments. However, the fact that the edges remained sharp (albeit with less contrast) caused the algorithm to return SFR curves for the clean results that were nearly indistinguishable from the refocused results for several magnification cases. Because the e-SFR slanted edge algorithm is ultimately based on taking the derivative of the edge spread function to obtain the line spread function (and then the SFR), the slope of the edge spread function is the key parameter in the algorithm. A close examination of the results revealed that for many cases, while the contrast across a given edge decreased, the slope of the edge spread profile remained virtually constant. Thus, there was little observed difference between the SFR of clean or occluded refocused images.

Supporting this observation is a note regarding the ISO 12233:2014 standard. The authors of the first edition of this standard (ISO 12233:2000) initially recommended using a higher contrast edge in e-SFR tests than is now specified. The new standard recommends a lower-contrast edge. (This is to ensure that the edge is imaged in the linear response range of the camera; unlike the scientific CCD that is the basis for our plenoptic camera, most consumer cameras have a non-linear response to very bright or very dark intensities.) The fact that this lower-contrast edge can be specified in the new standard for the above reason alone indicates that the e-SFR is not primarily designed to measure pure changes in contrast with all other things being equal.

## 2. Root Mean Square Error Metric

A more general metric used for quantifying the effects of various image restoration techniques is the mean square error [25]. Commonly the square root of this measure is used instead, where it is known as the root mean square error (RMSE) and given by Eq. (20) below.

$$RMSE = \sqrt{\frac{1}{MN} \sum_{i=1}^M \sum_{j=1}^N \left( I_{reference}(i,j) - I_{degraded}(i,j) \right)^2} \quad (20)$$

Note that  $M$  and  $N$  here refer to the horizontal and vertical dimensions of the image as measured in pixels. The RMSE can be taken as an unbiased estimator of the standard deviation of the error between the two images [37]. While the RMSE is a very useful tool for quantifying image restorations, a quantitative improvement does not necessarily manifest itself as a perceived qualitative improvement, so it is still worthwhile to examine the actual results.

## D. Results

LFIT was used to generate focal stacks consisting of 121 images between  $\alpha = 0.7$  and  $\alpha = 1.3$  for each occlusion position. (Refer back to Figure 29 for  $\alpha$  variation with focal plane depth and the section Influence of Number of Slices on Deconvolution Quality to be discussed later.) The center  $\alpha = 1.000$  slice corresponding to the focal plane was extracted for the refocused results. A PSF was generated per the earlier discussion in the Point Spread Function section. For the deconvolved results, the refocused and PSF focal stacks were used. A series of regularization parameters between  $1 \times 10^{-1}$  and  $1 \times 10^{-7}$  were used to generate separate deconvolved stacks. These deconvolved stacks were examined qualitatively and quantitatively to determine the best regularization parameter.

Using the RMSE as the primary metric, the refocused images can be compared to the clean reference images for all the magnifications and occlusion positions. These results are plotted in Figure 53 below. Although the actual position of the laser sheet occlusion varied between the magnification cases, here the x-axis position is normalized by displaying the position in increments of DOF.

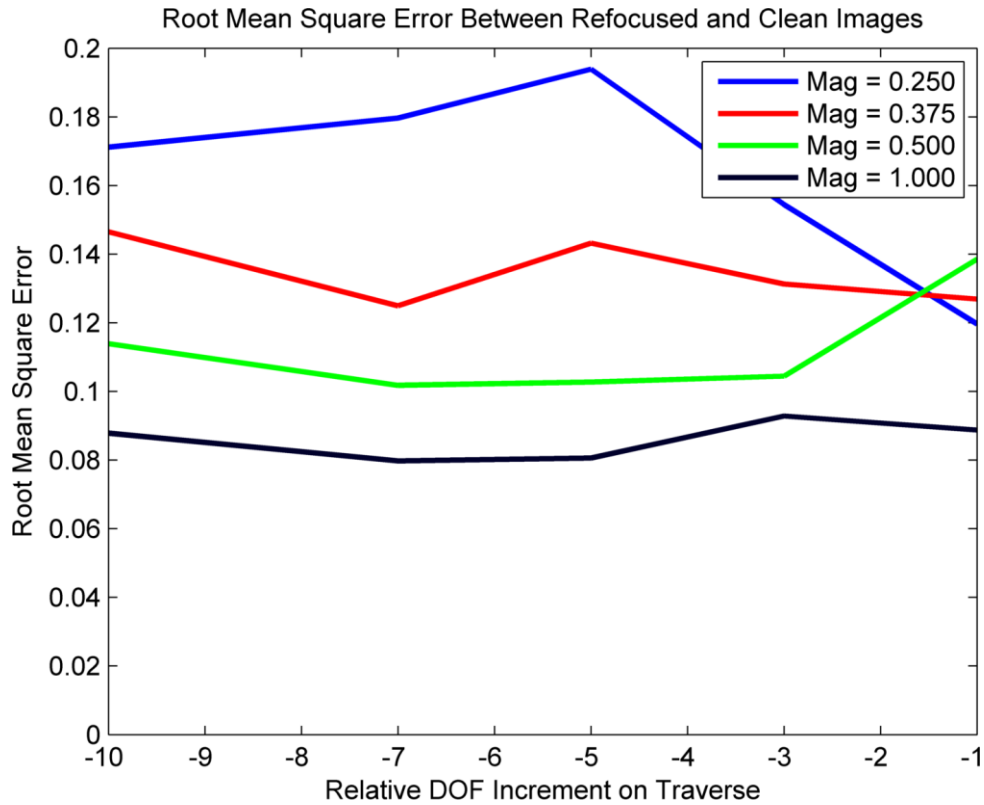


**Figure 53: Root mean square error between occluded refocused images and clean reference images**

The RMSE between the occluded refocused images and the clean reference images generally drops with increasing magnifications. This indicates that the translucent occlusion is having less of a degrading effect on the imaged target as the field of view narrows and magnification increases. For a given magnification case, the general variation between different relative DOF increments is likely due to the inherent variability in the occlusion generation in the experiment. Although this was attempted to be mitigated through the use of a fixed intensity laser,

consistently high usage of the smoke machine, and image averaging, these variations could not be completely eliminated. A careful examination of Figure 54 reveals these variations in the contrast.

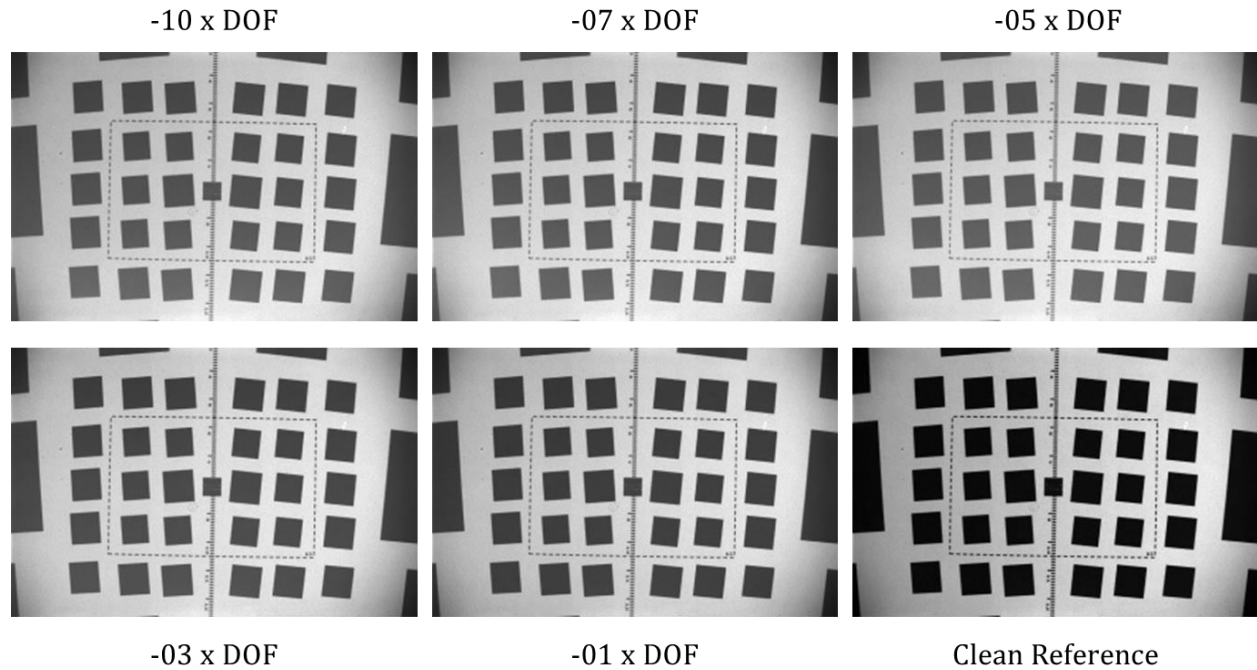


**Figure 54: Qualitative results for magnification 0.250 case occlusion testing**

The plotted RMSE in blue in Figure 53 matches qualitatively well with the images from the magnification 0.250 case in Figure 54 above. The -10 x DOF, -07 x DOF, and -05 x DOF case along the top row of the figure all appear to have virtually the same contrast. Carefully studying the gray level of the boxes in the -03 x DOF case and the -01 x DOF case shows improvement in contrast over the top row of images, manifested in a darkening of the imaged boxes. The reference image clearly has the highest contrast between the dark boxes and white background. While earlier the increase in contrast for the -03 x DOF and -01 x DOF cases was attributed to occlusion variability, it should be noted that another mechanism could be at play.

As seen in Figure 52, the laser sheet had a significant scattering effect as it illuminated the smoke. Thus, as the laser sheet was translated closer to the target, the laser may have had an illuminating effect on the target. However, the smoke output from the smoke machine had a tendency to rebound off of the target as it rapidly exited the machine's nozzle. This, combined with the relatively fast dissipation of the smoke, made it difficult to maintain a high density of smoke directly on the target. This possible gradient in smoke density could partially explain the higher contrast near the target as the laser sheet illuminates less smoke.

Turning the attention now to the deconvolved results, the improvements gained by applying 3D deconvolution to the occluded images can be seen in Figure 55 below. Note that a series of regularization parameters  $K$  were examined before choosing  $K = .075$  to minimize the RMSE between the deconvolved and clean images. Also, the deconvolved and reference images were slightly cropped to remove the influence of the black border introduced by the deconvolution process.

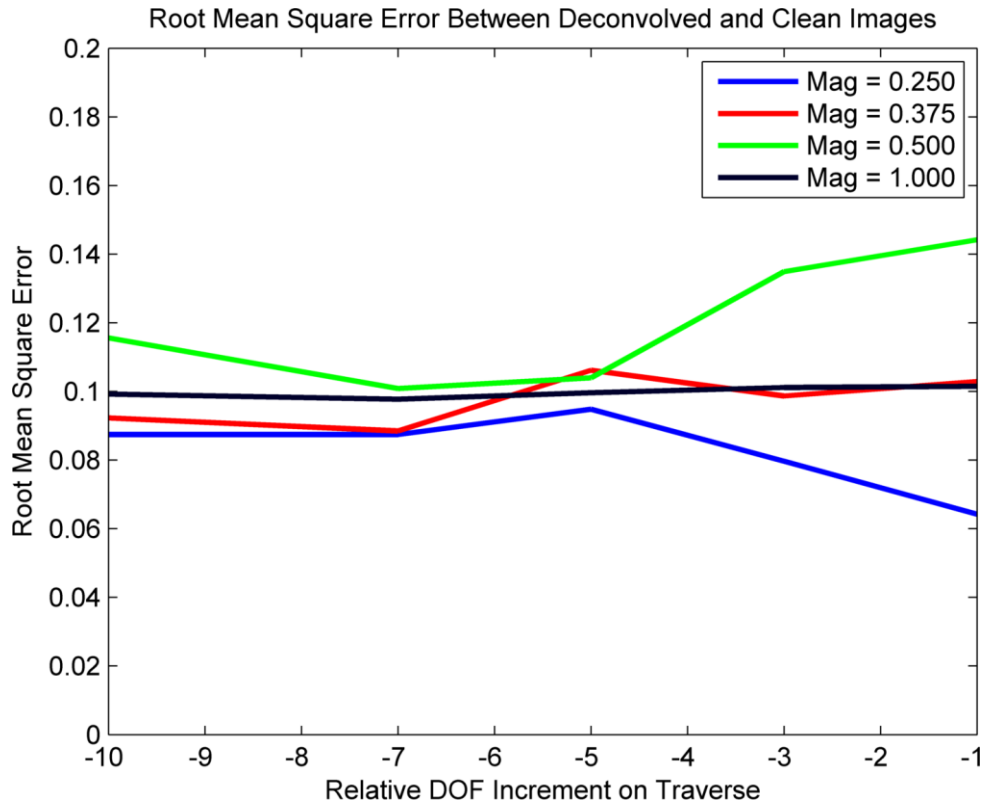


**Figure 55: Root mean square error between occluded deconvolved images and clean reference images**

Several interesting observations can be made regarding the RMSE for the deconvolved results above in Figure 55. For the two lower magnification cases, the deconvolved images had a lower RMSE than the refocused images, as noted by comparing Figure 53 and Figure 55. However, when performing the same comparison for the two higher magnification cases, the RMSE actually increased in the deconvolved images compared to the refocused images. This can be more clearly seen when comparing the refocused and deconvolved cases directly.

The RMSE between the deconvolved and clean images (as in Figure 55) was subtracted from the RMSE between the refocused and clean images (as in Figure 53). This calculated difference was then divided by the RMSE between the refocused and clean images to yield the percent change of the deconvolved results compared to the refocusing results. This is plotted in Figure 56.

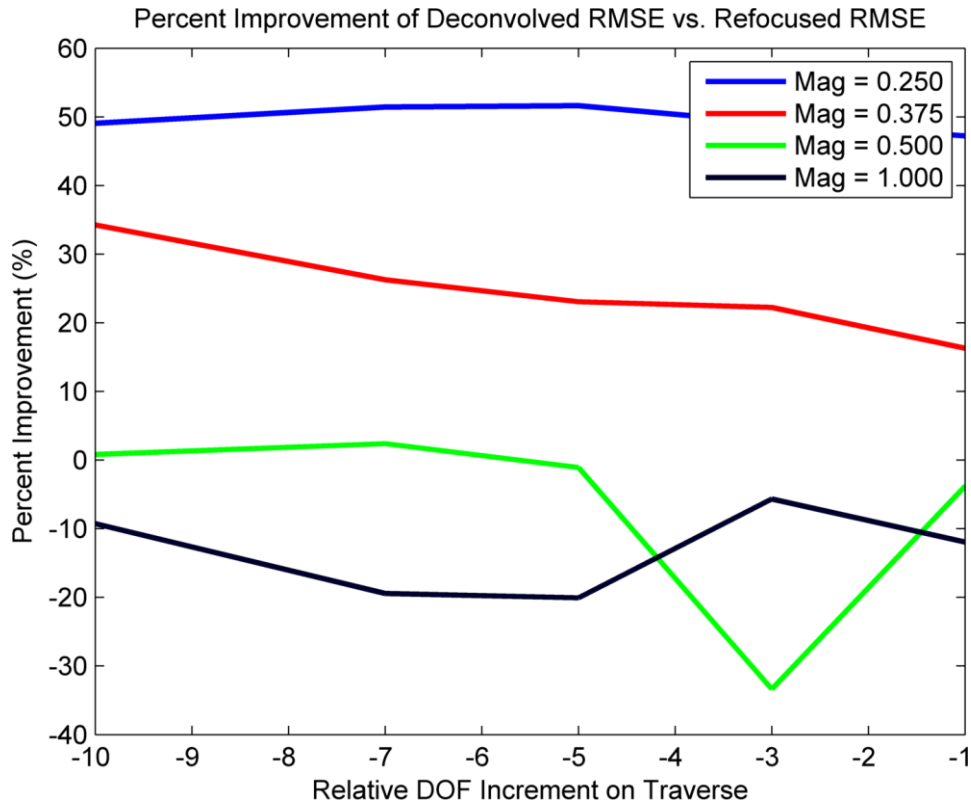


**Figure 56: Percent change between the RMSE results for deconvolution and refocusing**

The earlier discussion becomes clearer in light of the above figure. The measured deconvolution RMSE for the magnification case of 0.250 is 50% better than the plain refocusing RMSE. The measured deconvolution RMSE for the magnification case of 0.375 is on average approximately 25% better than the refocusing RMSE. This indicates the successful application of the deconvolution algorithm. Still, the question remains regarding the worse RMSE values for the higher magnification cases. Examining Figure 56 again, the magnification case of 0.500 has virtually no change between the deconvolved RMSE and the refocused RMSE, save for the -3 x DOF increment. The 1.000 magnification case wavers around a 10% RMSE change for the worse.

Several factors are likely at play in these two cases. Below in Figure 57, selected deconvolved and corresponding refocused results are provided for a magnification of 1.000.

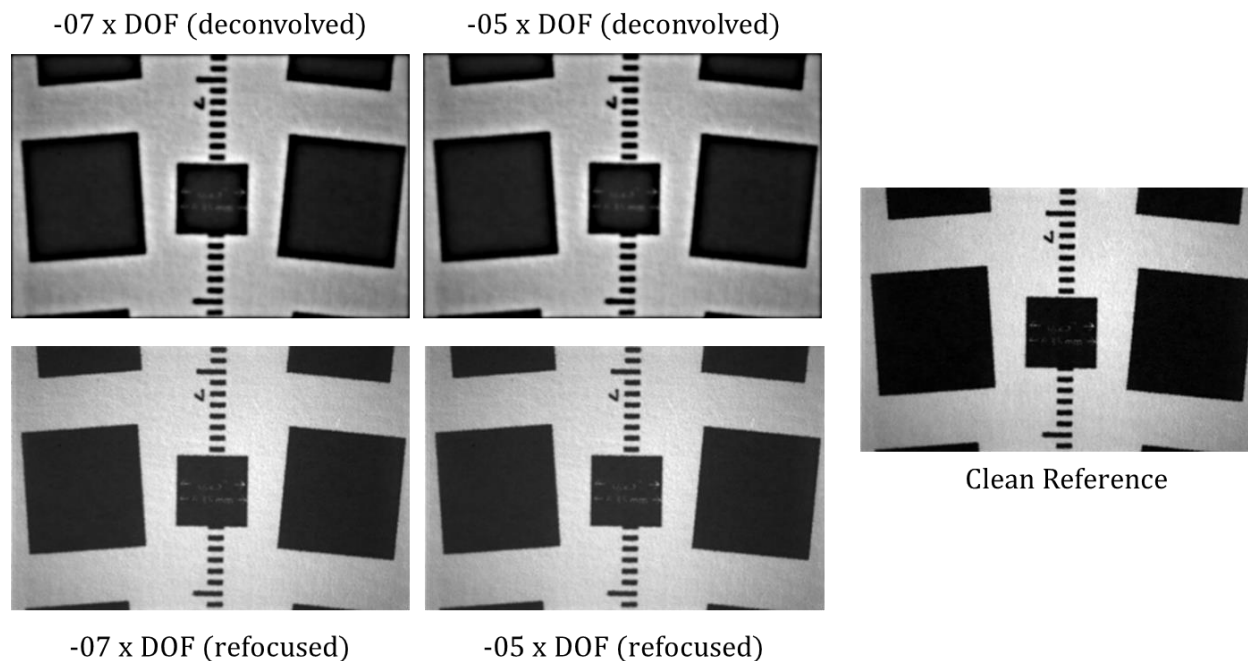


**Figure 57: Qualitative comparison of deconvolved results with refocusing results at a magnification of 1.000**

The deconvolved results at top show greater edge contrast than the refocused results at the bottom of the figure. However, the deconvolution has also slightly washed out the interior of the large black squares. Additionally, at this high magnification, the deconvolution has revealed more of the texture of the cardstock paper background than is even visible in the clean reference image. These lead to differences when directly comparing the reference image with the deconvolved image in the RMSE algorithm.

Perhaps the primary factor to consider is that qualitatively speaking, the refocused images are not that different from the clean reference image. While there is some loss of contrast, the occluding effect in the captured images is far subtler than was expected at the start of the experiments. Contrast differences between the clean and refocused images in Figure 57, while present, are quite faint. This hearkens back to the earlier observation that at high magnifications, the observed occlusions were less than at lower magnifications.



The conclusions to be drawn from this quantitative analysis are multifold. First, given sufficient translucent occlusions, 3D deconvolution is very effective in reducing the degradation of the occlusion. At the lower magnifications where the observed occlusion density was greater, deconvolution performed the best. The second observation is that for subtle, low density occlusions, 3D deconvolution will not necessarily yield quantitatively better results.

## VII. Example Deconvolution Results as Applied to Flames

### A. Introduction

With the previous quantitative results shared, now follows several examples displaying the power of 3D deconvolution to improve the resolvability of flames in a variety of experimental configurations. While the quantitative occlusion experiments investigated a largely smooth, uniform, low magnitude occlusion, these results put the deconvolution algorithm to the test on images with a greater mix of spatial frequencies. Although these results are overall qualitative in nature, they are nevertheless an effective demonstration of what 3D deconvolution is capable of when applied to real images.

### B. Torch and Bunsen Burner Experiment

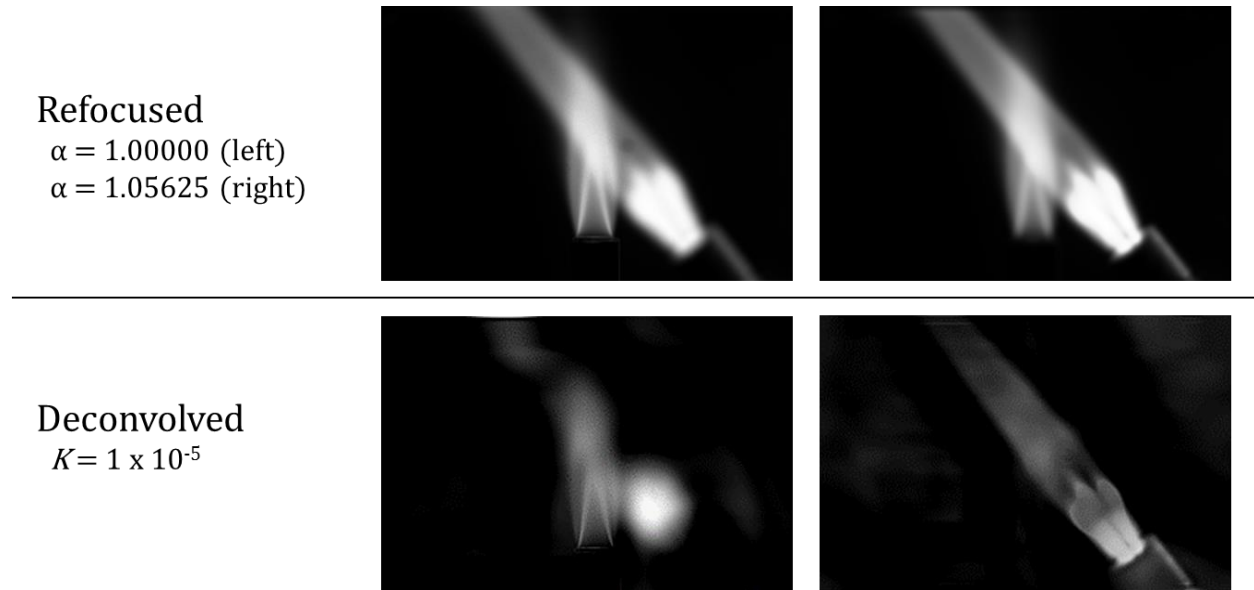
An experiment was set up with the plenoptic camera viewing a Bunsen burner, as seen in Figure 58 below.



Figure 58: Experimental setup for torch and Bunsen burner testing

The nominal focal plane was positioned on the Bunsen burner. A handheld propane torch was inserted into the field of view between the plenoptic camera and the burner such that the flame

images overlapped. Observe that the actual flames in the experiment were separated at different depths. Below in Figure 59, a comparison is made between refocusing and deconvolution. Intensities were adjusted for clarity.



**Figure 59: Example flame and torch image comparing deconvolution to refocusing alone**

In the refocused image at the top left, the Bunsen burner is seen to be in focus while the occluding torch is out of focus. In the deconvolved image at the bottom left, there is increased definition on the burner flame, and the torch intensity has been significantly attenuated as it is at a different depth. In the refocused image at the top right, the torch has been brought into focus with computational refocusing alone. Applying deconvolution as seen at the bottom right dramatically enhances the clarity of the torch flame. Fine details in the torch flame structure are now visible and the Bunsen burner is nearly completely removed from the background. This shows the powerful ability of deconvolution to better isolate objects or flames by depth while simultaneously increasing the resolvability of those objects.

### C. Flame Sheet and USAF Target

In another experiment, a target was placed beyond the nominal focal plane of the plenoptic camera. A photo of the experimental setup is given below in Figure 60.

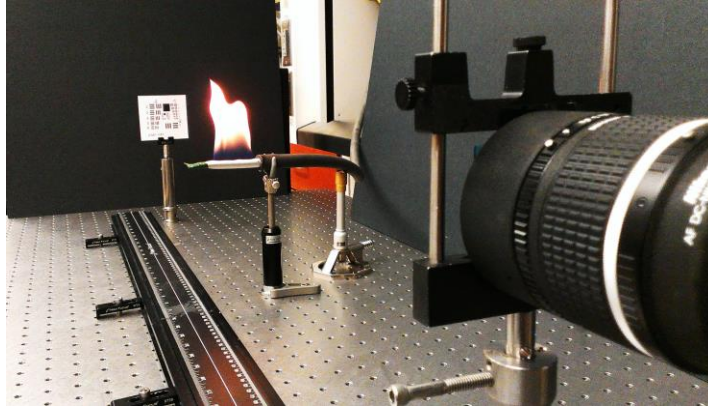


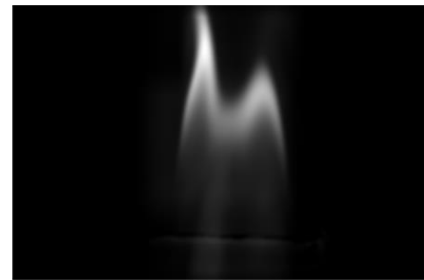
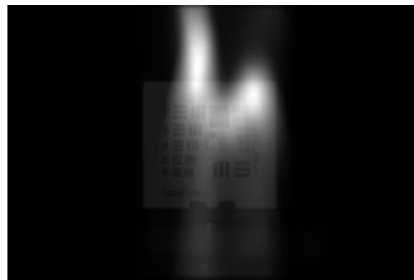
Figure 60: Experimental setup for target occluded by flame sheet

A flame sheet was generated via a modified Bunsen burner placed in front of the nominal focal plane such that the camera was looking through the flame sheet at the out of focus target. A 135 mm Nikon lens was used for this test. Focal stacks were generated and deconvolution was applied. The refocusing and deconvolved results are given below in Figure 61.

Refocused

$\alpha = 0.95060$  (left)

$\alpha = 1.09518$  (right)



Deconvolved

$K = 1 \times 10^{-3}$

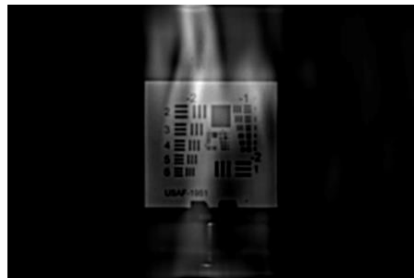


Figure 61: Example flame sheet obscuring a target for comparing deconvolution to refocusing alone

In the top left image of the figure, the image was refocused onto the target behind the flame. While the target itself is visible as the flame is indeed a translucent (not opaque) occlusion, it is not readily legible. Applying deconvolution results in the enhanced image at the bottom left of the above figure. While some artifacts from the flames still remain, the contrast and overall visibility of the target has been clearly improved. Looking now at the flame images on the far right of the figure, the refocused image at the top left does a fairly good job of isolating the flame from the target. This is largely due to the low intensity of the target to begin with, however. Nevertheless, the deconvolved image shown in the bottom right shows greater definition along the edges of the flame structure, and the target is completely removed.

#### **D. Target Plate and Bunsen Burner**

##### *1. Description and Results*

A similar experiment with a different target and a smaller, more defined flame was conducted. The experimental setup is pictured in Figure 62.

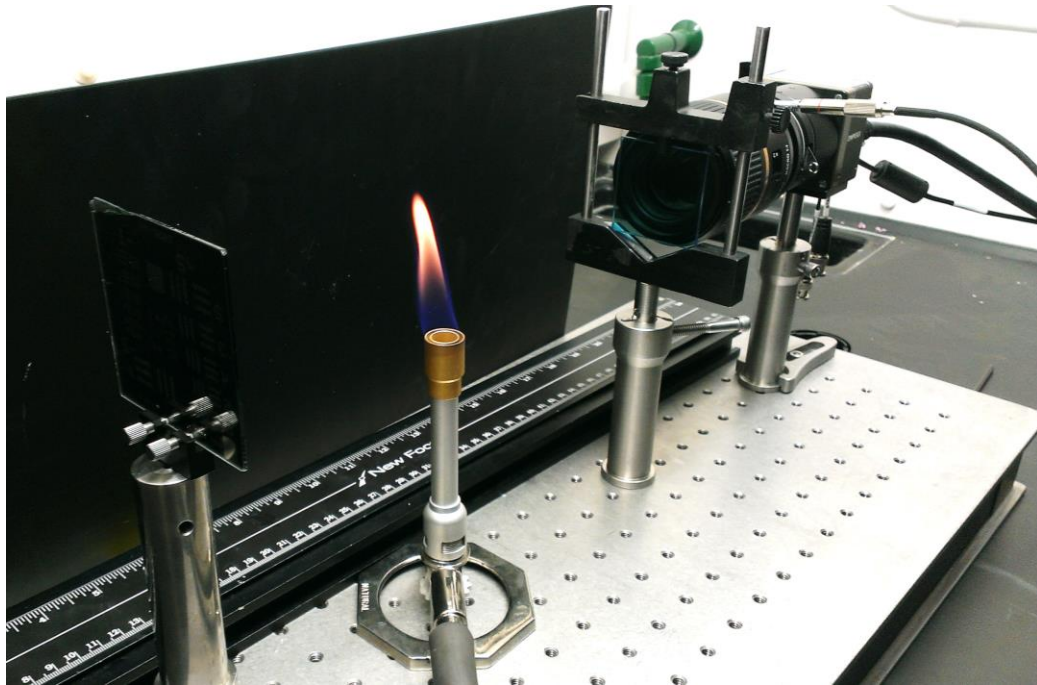


**Figure 62: Flame obscuring 1951 USAF target experimental setup**

Here, the same 60 mm Tamron macro lens described in the earlier quantitative experiments was used. The focal plane in this experiment was located between the Bunsen burner and the target. A Thorlabs FGB37S 335- 610 nm glass bandpass filter was mounted directly in front of the lens as in several of these qualitative experiments in order to attenuate near-infrared emissions from the flame. Comparative slices from the refocused and deconvolved focal stacks are shown below in Figure 63.

Refocused

$\alpha = 0.96506$  (left)

$\alpha = 1.06867$  (right)



Deconvolved

$K = 1 \times 10^{-3}$

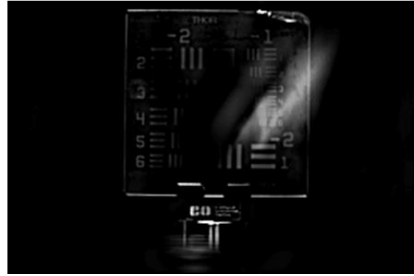


**Figure 63: Bunsen burner and USAF target refocusing and deconvolution slice comparison**

Even after adjusting the intensities for clarity, the refocused target plate in the top left refocused image is difficult to read. After the deconvolution process, the target contrast is dramatically enhanced as seen in the lower left image. Regions of the target previously covered by the flame are now legible, and the overall sharpness of the target is much higher than in the refocused image. Turning now to the Bunsen burner, in the refocused image at top left, the flame is well visible as it is in the foreground of the image, but the out of focus target remains in the background. Following the deconvolution in the bottom right image, the target is now removed from the background and the Bunsen burner is isolated.

## *2. Influence of Number of Slices on Deconvolution Quality*

For 3D deconvolution, a focal stack of the experimental volume and a focal stack of the PSF are required. Dimensionally, both must match. A test was performed to examine the impact the number of slices used in the focal stack had on the deconvolved results. The experimental setup is shown previously in Figure 62.

The PSF was modeled per the discussion in the Point Spread Function section. Focal stacks were generated consisting of 4, 8, 16, 32, 64, 128, 256, and 512 slices. These focal stacks were each deconvolved with a regularization parameter  $K = 1 \times 10^{-3}$ . The slice closest to the target and the slice closest to the flame was each separately extracted. The best slices from each stack are thus shown in Figure 64, with the intensity exaggerated for clarity.



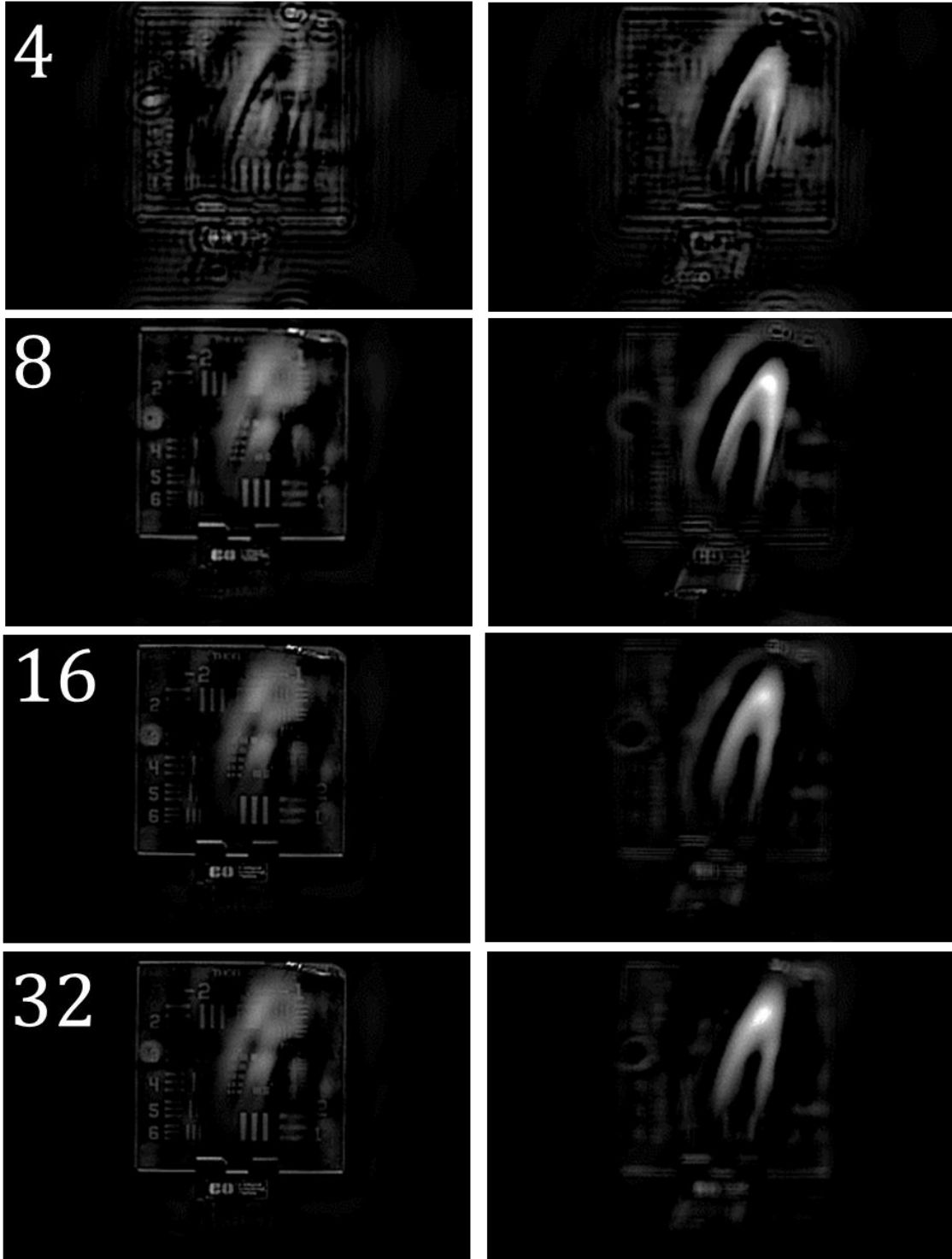


**Figure 64: Comparison of (low) number of slices on deconvolved quality**

While 4 slices case is clearly unusable, with as few as 8 slices the target plate is already comparable to the 32 slice case. Although there are residual artifacts, the flame is acceptably

isolated with 16 slices and achieves the best result at 32 slices. The rest of the results are presented in Figure 65.

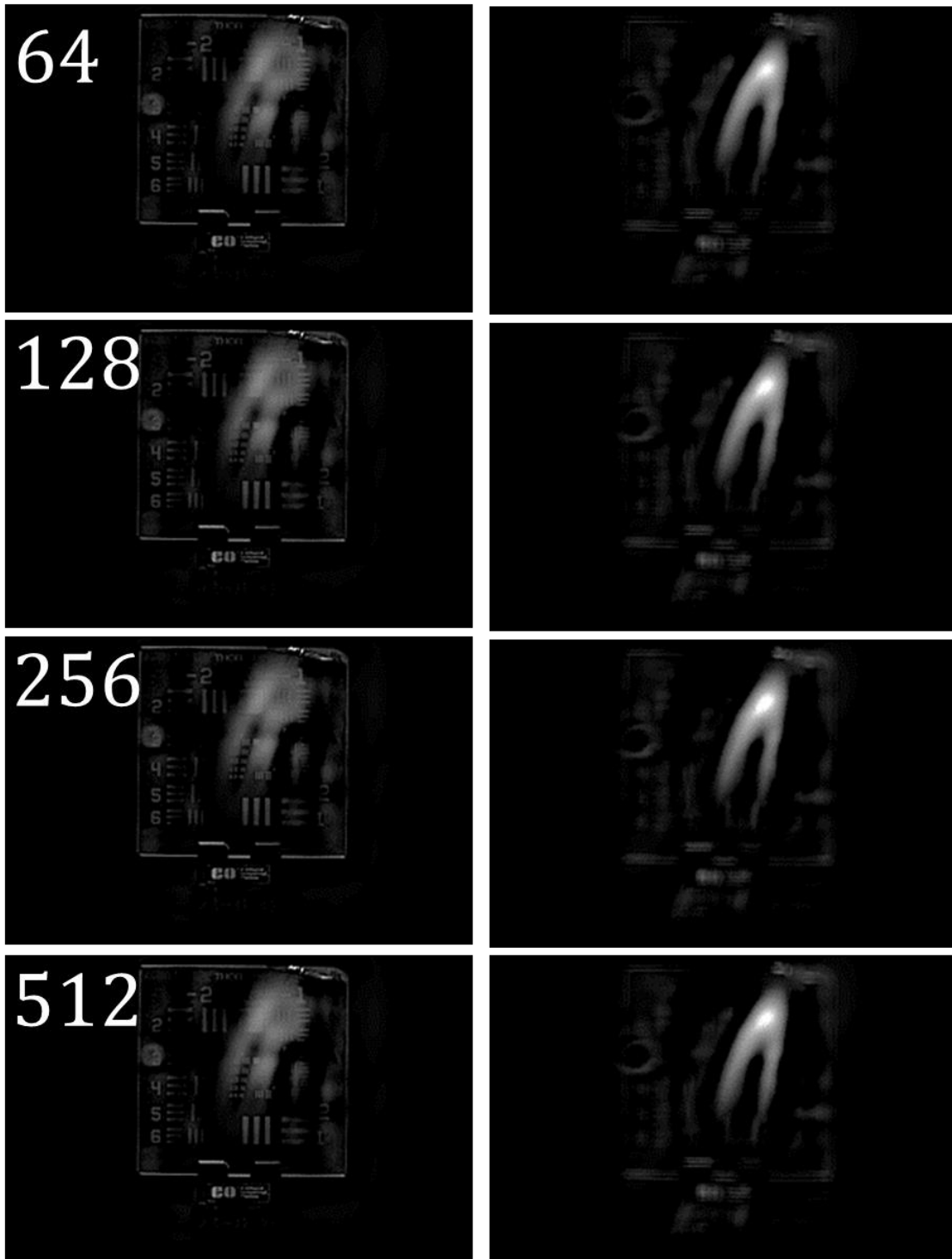


Figure 65: Comparison of (high) number of slices on deconvolved quality

Examining the results for the large number of slices, it can be seen that there is little difference between the deconvolved results. In fact, little qualitative difference can be observed between these high number cases versus the 16 or 32 slice case. This makes sense in light of the earlier DOF discussion where it was noted the number of distinct planes that can be refocused is proportional to  $P$ , where  $P$  is the diameter of a microlens in pixels. Since a single pixel sets the overall DOF,  $P$  different planes should be resolvable within that depth of field. Given that a microlens is approximately 16 pixels across, the fact that the improvement in the results plateaus between 16 to 32 slices indicates agreement. With that said, a more generous value of 121 slices was used for the occlusion testing in this thesis to give margin against any unexpected issues.

### E. Other Qualitative Results

Finally, several results from a non-occluded experiment are given below in Figure 66. A metal bar spanned the field of view with large flames impinging on this bar from a nozzle below. In this experiment, there was not a target or feature of interest behind the flames, nor was the DOF especially shallow. These results are included, however, to show the qualitative improvements possible even when directly imaging chaotic non-occluded flame structures.

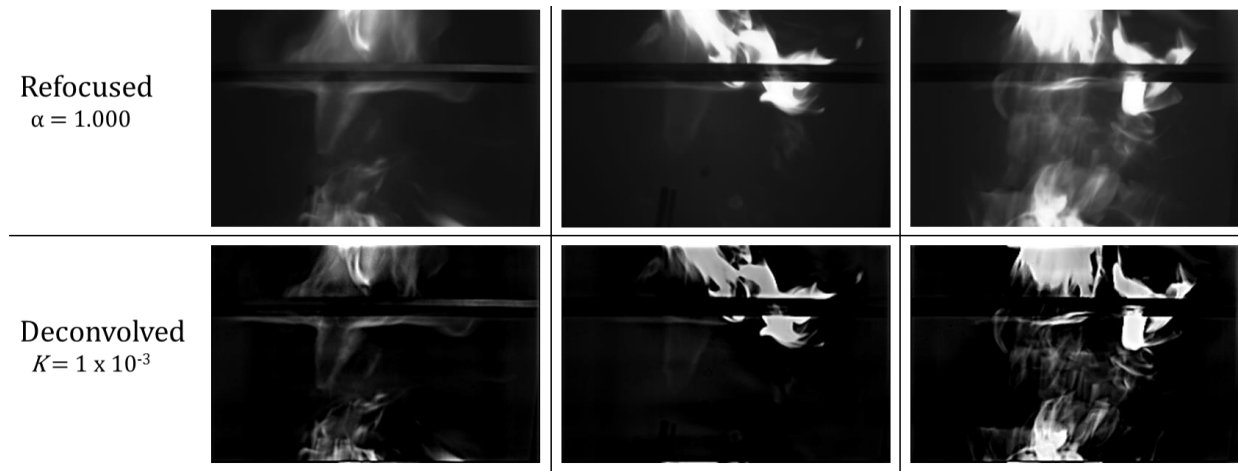


Figure 66: Several examples of (non-occluded) flames comparing refocusing and deconvolution

Each column above in the figure corresponds to a different frame of the experiment, in contrast to the previous result figures. The top row shows refocused results where the flames were all located at the focal plane of the experiment. The bottom row shows the effect of applying deconvolution to the experimental focal stacks. The deconvolution algorithm enhances the clarity and definition of the various flame structures imaged above. The deconvolved results all show improved contrast over the simple refocused results as well. These images as well as the previous results confirm that deconvolution paired with the plenoptic camera can produce both quantitatively and qualitatively better images than refocusing alone.

## VIII. Conclusions and Future Work

The plenoptic camera has been shown to be a powerful tool for rapidly capturing 3D information about a given scene from a single snapshot. This gives the plenoptic camera great utility in the context of flow diagnostics where other three-dimensional tools can be cumbersome to setup and use. While the plenoptic camera is still a relatively young technology, it is rapidly maturing into a very attractive flow visualization and analysis tool, particularly in the realm of particle image velocimetry. The thesis has aimed to posit and demonstrate the applicability of the plenoptic camera for imaging flames or more general scenes containing translucent occlusions.

A thorough overview of the mechanics of light field imaging with a plenoptic camera was provided. The light field was introduced and the fundamental concepts undergirding plenoptic imaging were explained. Processing plenoptic images in the Light Field Imaging Toolkit was discussed from a practical and algorithmic perspective. The concept and implications of the depth of field from conventional photography was introduced into the context of light field imaging.

This thesis has also explored the application of the plenoptic camera towards imaging in environments with translucent occlusions. These translucent occlusions can take many forms, but a primary application in view is that of chemically reacting flow imaging, or more specifically flame diagnostics. Towards that end, the framework of deconvolution was presented as a way of modeling and reversing the effects of out of focus occlusions on a scene. Various deconvolution algorithms were discussed and justification was given for the selection of a regularized 3D Wiener filter. The point spread function was defined and explained, several approaches to computing it were shared, and the hybrid model used in this paper was outlined.

Quantitative experiments to characterize the refocusing performance of the plenoptic camera were conducted. Various spatial frequency metrics were discussed and the edge-based spatial frequency response slanted edge metric was chosen for the refocusing performance testing. The spatial frequency response curves for the refocusing tests were shared, and the best spatial frequency response was found to be when the target was located at the nominal focal plane of the camera. A discussion of the Nyquist frequency, aliasing, and its relation to the observed spatial frequency response curves was presented. It was noted that spatially supersampling plenoptic images in  $(s, t)$  served to reduce the response above the Nyquist frequency and thus reduce the aliasing.

Experiments to quantify the improvements gained by deconvolution compared to refocusing alone in an environment containing translucent occlusions were performed. The translucent occlusions tested in this experiment were largely smooth and uniform. The need for and selection of a new metric, the root mean squared error, was shared. Quantitative results were presented indicating that 3D deconvolution is a powerful tool to increase the resolvability of targets in occluded environments. Finally, qualitative results for flame images with a mix of smooth gradients and fine edges were shared. These results showed the power of 3D deconvolution to improve the resolvability of actual flames in various imaging scenarios.

The relatively simple setup of the plenoptic camera coupled with the powerful technique of 3D deconvolution makes it an attractive option for imaging in environments with a variety of translucent occlusions. As a single camera technique, experimental setups are significantly streamlined while the need for complex multi-camera calibrations and alignments is eliminated. The plenoptic camera's minimal optical access requirements make it uniquely suited for imaging chemically reacting flows specifically. From a single image, a plenoptic camera captures 3D data

without any scanning mirrors or moving parts. All these factors commend the plenoptic camera as a useful tool for flow diagnostics, particularly in the context of flames.

Future work could investigate new deconvolution algorithms. While the regularized 3D Wiener filter used in this thesis serves as an excellent baseline, more advanced iterative algorithms could be implemented to investigate tradeoffs between improved image quality and increased computational cost. Although some discussion was presented on the tradeoffs between number of slices in a focal stack and the deconvolution quality, this relationship could be evaluated more rigorously. The influence of minimum and maximum  $\alpha$  values used in the generation of the focal stacks for deconvolution was not explicitly investigated in this work and would be another area of future study.

While the quantitative occlusion testing experiments in this thesis used a smoke machine and laser sheet to simulate a translucent occlusion, it would be compelling to see a similar test repeated with some type of flame sheet assuming the practical hurdles could be overcome. Because the quantitative occlusion testing performed here dealt with largely smooth occlusions, future work could explore ways of generating spatially varying occlusions with a mix of low and high frequency content to better evaluate the deconvolution algorithm quantitatively.

To limit the number of variables in these experiments, a single lens was used for both quantitative tests. An interesting experiment would be to calculate the spatial frequency response curves as in the refocusing experiment for a variety of lenses. The influence of extension tubes and focus setting could be characterized. Additionally, one could measure the variation of the spatial frequency response with position in the image frame.

Finally, although the model of the point spread function used in this research worked well, future work could examine other approaches to modeling the point spread function. An analytic

model, hybrid model as here, and an experimentally measured model could all be compared to determine the best type of approach. The spatial variance of the point spread function could also be investigated experimentally to determine how valid our theoretical assumption of spatial-invariance is.

As powerful as the plenoptic camera is alone, the addition of 3D deconvolution only enhances the device as a flow diagnostic tool. In contrast to other image processing techniques, 3D deconvolution does not require any prior assumptions regarding the nature of the volume. This makes the technique versatile and well suited for imaging subjects such as flames where the structure may be unknown prior to the experiment. As plenoptic camera technology and processing tools continue to mature, this device will become increasingly useful for characterizing a wide variety of flows.



## References

- [1] R. J. Adrian and J. Westerweel, *Particle Image Velocimetry*. Cambridge University Press, 2010.
- [2] F. Scarano, “Tomographic PIV: principles and practice,” *Meas. Sci. Technol.*, vol. 24, p. 012001, 2012.
- [3] A. Lozano, B. Yip, and R. K. Hanson, “Acetone: a tracer for concentration measurements in gaseous flows by planar laser-induced fluorescence,” *Exp. Fluids*, vol. 13, no. 6, Oct. 1992.
- [4] S. Deusch and T. Dracos, “Time resolved 3D passive scalar concentration-field imaging by laser induced fluorescence (LIF) in moving liquids,” *Meas. Sci. Technol.*, vol. 12, pp. 188–200, 2001.
- [5] S. Deusch, H. Merava, T. Dracos, and P. Rys, “Measurement of velocity and velocity derivatives based on pattern tracking in 3D LIF images,” *Exp. Fluids*, vol. 29, pp. 388–401, 2000.
- [6] M. Levoy, “Light fields and computational imaging,” *Computer (Long. Beach. Calif.)*, vol. 39, pp. 46–55, 2006.
- [7] G. Lippmann, “Épreuves réversibles. photographies intégrales.” *Comptes-Rendus Acad. des Sci.*, pp. 446–451, 1908.

- [8] E. H. Adelson and J. Y. a Wang, “Single lens stereo with a plenoptic camera,” *IEEE Trans. Pattern Anal. Mach. Intell.*, vol. 14, no. 2, pp. 99–106, 1992.
- [9] R. Ng, M. Levoy, G. Duval, M. Horowitz, and P. Hanrahan, “Light Field Photography with a Hand-held Plenoptic Camera,” *Informational*, pp. 1–11, 2005.
- [10] A. Lumsdaine and T. Georgiev, “The Focused Plenoptic Camera,” in *IEEE International Conference on Computational Photography*, 2009.
- [11] K. Lynch, T. Fahringer, and B. Thurow, “Three-Dimensional Particle Image Velocimetry Using a Plenoptic Camera,” *50th AIAA Aero Sci. Meet. Incl. New Horizons Forum Aerosp. Expo.*, no. January, pp. 1–14, 2012.
- [12] B. S. Thurow and T. Fahringer, “Recent Development of Volumetric PIV with a Plenoptic Camera,” *10th Int. Symp. Part. Image Velocim.*, 2013.
- [13] J. Weinkauff, D. Michaelis, A. Dreizler, and B. Böhm, “Tomographic PIV measurements in a turbulent lifted jet flame,” *Exp. Fluids*, vol. 54, pp. 1–5, 2013.
- [14] X. Li and L. Ma, “Volumetric imaging of turbulent reactive flows at kHz based on computed tomography.,” *Opt. Express*, vol. 22, no. 4, pp. 4768–78, 2014.
- [15] K. Y. Cho, A. Satija, T. L. Pourpoint, S. F. Son, and R. P. Lucht, “Time-Resolved 3D OH Planar Laser-Induced Fluorescence System for Multiphase Combustion Kevin,” in *8th U.S. National Combustion Meeting*, 2013.

- [16] M. L. Greene and V. Sick, "Volume-resolved flame chemiluminescence and laser-induced fluorescence imaging," *Appl. Phys. B Lasers Opt.*, vol. 113, pp. 87–92, 2013.
- [17] P. Anglin, S. J. Reeves, and B. S. Thurow, "Characterization of Plenoptic Imaging Systems and Efficient Volumetric Estimation from Plenoptic Data." 2014.
- [18] J. T. Bolan, K. C. Johnson, and B. S. Thurow, "Enhanced Imaging of Reacting Flows Using 3D Deconvolution and a Plenoptic Camera," in *AIAA SciTech*, 2015, pp. 1–15.
- [19] E. Adelson and J. Bergen, "The plenoptic function and the elements of early vision," *Comput. Model. Vis. ....*, pp. 3–20, 1991.
- [20] M. Levoy and P. Hanrahan, "Light field rendering," *Proc. 23rd Annu. Conf. Comput. Graph. Interact. Tech. - SIGGRAPH '96*, pp. 31–42, 1996.
- [21] R. Ng, "Digital light field photography," pp. 1–203, 2006.
- [22] T. W. Fahringer and B. S. Thurow, "Comparing Volumetric Reconstruction Algorithms for Plenoptic-PIV," in *AIAA SciTech*, 2015, no. 53rd AIAA Aerospace Sciences Meeting, pp. 1–10.
- [23] C. Thomason, "Determination of the Image Distance in a Plenoptic Camera," Auburn University, 2014.
- [24] S. F. Ray, *Applied Photographic Optics*. London: Focal Press, 1988.
- [25] R. C. Gonzalez and R. E. Woods, *Digital Image Processing*, Third. Upper Saddle River: Pearson Prentice Hall, 2008.

- [26] P. Sarder and a. Nehorai, “Deconvolution methods for 3-D fluorescence microscopy images,” *IEEE Signal Process. Mag.*, vol. 23, no. May 2006, pp. 32–45, 2006.
- [27] W. Wallace, L. H. Schaefer, and J. R. Swedlow, “A working person’s guide to deconvolution in light microscopy,” *Biotechniques*, vol. 31, no. 5, pp. 1076–1097, 2001.
- [28] P. Anglin, S. J. Reeves, and B. S. Thurow, “Direct FFT-Based Volumetric Reconstruction from Plenoptic Data,” *IEEE Transactions on Image Processing*. 2015.
- [29] M. Broxton, L. Grosenick, S. Yang, N. Cohen, A. Andalman, K. Deisseroth, and M. Levoy, “Wave optics theory and 3-D deconvolution for the light field microscope.,” *Opt. Express*, vol. 21, no. 21, pp. 25418–39, 2013.
- [30] T. E. Bishop and P. Favaro, “The light field camera: Extended depth of field, aliasing, and superresolution,” *IEEE Trans. Pattern Anal. Mach. Intell.*, vol. 34, no. 5, pp. 972–986, 2012.
- [31] R. A. Raynor, “Rangefinding with a Plenoptic Camera,” Air Force Institute of Technology, 2014.
- [32] H. Koren, “Sharpness: What is it and how is it measured?,” *imatest*, 2014. [Online]. Available: <http://www.imatest.com/docs/sharpness/>. [Accessed: 06-Apr-2015].
- [33] ISO, “ISO 12233:2014(E) Photography - Electronic still picture imaging - Resolution and spatial frequency responses.” ISO, Geneva, 2014.
- [34] D. A. Kerr, “Determining MTF with a Slant Edge Target,” 2010.

- [35] D. Firmenich and S. Süsstrunk, “Spatial Frequency Response of a Plenoptic Camera,”  
École polytechnique fédérale de Lausanne, 2014.
- [36] G. D. Boreman, *Modulation Transfer Function in Optical and Electro-Optical Systems*.  
2001.
- [37] C. M. Judd, G. H. McClelland, and C. S. Ryan, *Data Analysis: A Model Comparison  
Approach, Second Edition*. Routledge, 2011.

## Appendices

### A. Derivation of Aperture Matching Relationship

As explained in the discussion about Figure 9 previously, the aperture of the main lens of the camera must be set such that the microimages formed by each microlens do not overlap. The relationship given in Eq. (1) for matching the aperture to maximize the microimages without overlap is derived below.

In a conventional camera, the aperture is defined by a so-called f-number (sometimes written as f/number, and also known as f-stop). This equation is given below in Eq. (21):

$$f/\# = N = \frac{f_{main\ lens}}{D_{aperture}} \quad (21)$$

A less frequently used term, related to the f-number, is the image side f-number. This term is defined in [9] and is given here in Eq. (22) as the separation between the principal plane of the main lens and microlens plane divided by the diameter of the aperture of the main lens. Since the main lens is focused directly onto the microlens plane ( $\beta = 1$ ), this separation distance is simply the image distance  $s_i$ .

$$N' = \frac{s_i}{D_{aperture}} \quad (22)$$

Rearranging Eq. (21):

$$D_{aperture} = \frac{f_{main\ lens}}{N}$$

Also rearranging Eq. (22):

$$D_{aperture} = \frac{s_i}{N'}$$

Allows for the  $D_{aperture}$  terms to be equated:

$$\frac{f_{main\ lens}}{N} = \frac{S_i}{N'}$$

Which results in Eq. (23):

$$N = \frac{f_{main\ lens}}{S_i} N' \quad (23)$$

The plenoptic camera optical geometry can be drawn to reveal relationships via similar triangles:

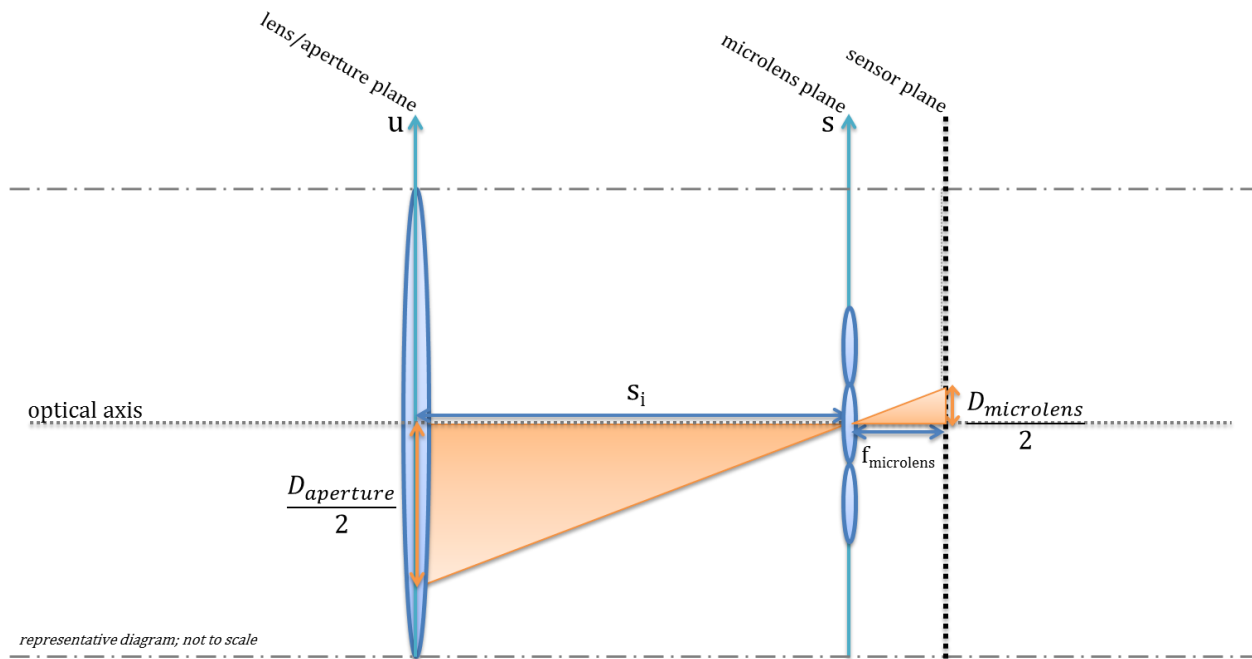


**Figure 67: Geometric relationships in the plenoptic camera to permit f-number matching**

Inspecting the figure, the following relationship can be observed:

$$\frac{f_{micro}}{\frac{D_{micro}}{2}} = \frac{S_i}{\frac{D_{aperture}}{2}}$$

Simplifying:

$$\frac{f_{micro}}{D_{micro}} = \frac{S_i}{D_{aperture}} \quad (24)$$

Note that the left and right hand sides of Eq. (24) have already been defined:

$$N_{microlenses} = \frac{f_{micro}}{D_{micro}} = \frac{S_i}{D_{aperture}} = N' \quad (25)$$

Also note that the f-number of the microlenses in our prototype camera is f/4 ( $N_{microlenses} = 4$ ).

$$N_{microlenses} = \frac{S_i}{D_{aperture}} = N' = 4 \quad (26)$$

We note that magnification (positive convention) can be defined as in Eq. (27):

$$M = \frac{f_{main\ lens}}{S_o - f_{main\ lens}} \quad (27)$$

From the thin lens equation, we obtain Eq. (28):

$$S_i = f_{main\ lens}(1 + M) \quad (28)$$

Substituting Eq. (28) into Eq. (23):

$$N = \frac{f_{main\ lens}}{f_{main\ lens}(1 + M)} N' \quad (29)$$

The relationship given in Eq. (1) is thus obtained:

$$N = \frac{N'}{1 + M} \quad (30)$$

For our camera with f/4 microlenses, this becomes Eq. (31):

$$N = \frac{4}{1 + M} \quad (31)$$



## B. Effect of Averaging on Calibration Images

This section examines the impact of averaging a sequence of calibration images on calibration accuracy. See the earlier Calibration section and end of the Typical Experimental Procedure section for background information on calibration images. In practice, our lab typically captures a sequence of 100 calibration images. This sequence is then averaged in LFIT, and one of two calibration algorithms is applied to the averaged image to determine the location of each microlens center.

To see what effect averaging has on the calibration accuracy, a set of 100 calibration images was selected from an earlier experiment. An averaged image was computed and compared to a single image from the set of 100 images. The results are shown below in Table 1:

**Table 1: Single calibration image versus averaged calibration image**

	Max Intensity	Min Intensity	Standard Dev
Single Image	0.1842	0.00000	0.0189
Averaged Image	0.1828	0.00027	0.0189

The various above metrics are generally comparable. The two images were then processed with the standard rectangular array calibration function in LFIT. The algorithmically calculated positions were separately stored. The calibrated microlens positions for the single image were subtracted from the calibrated microlens positions of the averaged image. The difference between the two calibrations is plotted below for each microlens index for both X and Y positions in Figure 68 and Figure 69.

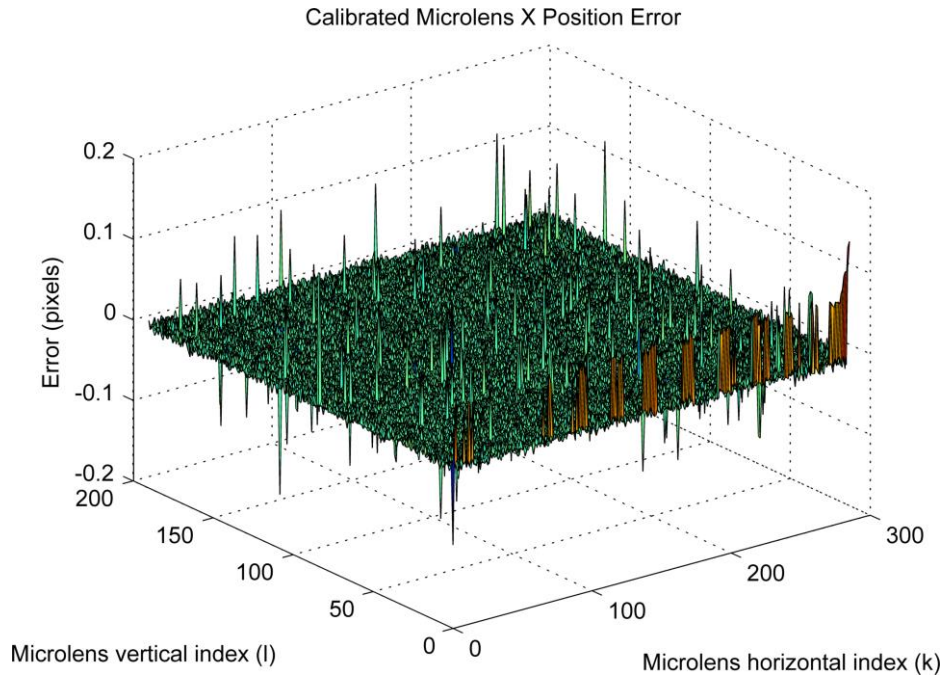


**Figure 68: Surface plot of calibrated microlens X position error in pixels**

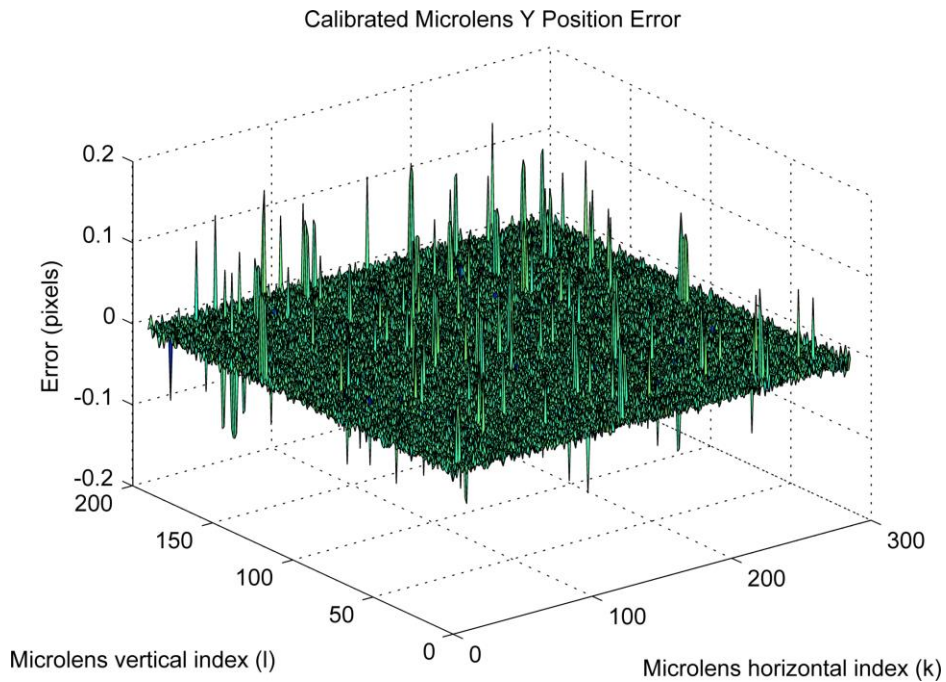


**Figure 69: Surface plot of calibrated microlens Y position error in pixels**

For the most part, the differences are relatively minor. There are a number of microlens position differences on the order of a tenth of a pixel. This is somewhat concerning; while qualitatively the effect on an output image would be in most cases minimal, these differences could have a significant impact on particular applications like PIV where the positional accuracy of particles is paramount. For these reasons, it is recommended to continue capturing and averaging multiple calibration images.

### C. Circular Aperture and (u,v) Supersampling Effects on (s,t) Sampling Grids

When implementing the refocusing equation in double integral form as in Eq. (4), LFIT loops through the range of  $u$  and  $v$  values. As discussed previously, virtually all lenses available have a circular aperture. This serves to create circular images behind each microlens. However, the full square microimage is read into LFIT. By defining a disk centered about the centroid of each microlens, any data outside the disk can be masked out. This is less of a concern in the prototype 16 MP camera as it has a rectangular array of microlenses. However, this becomes critical in cameras with hexagonal arrays, as the formerly empty space is filled in largely by a more efficient packing of microlenses. The effect on the refocusing sampling grid when enforcing a circular aperture is shown below in Figure 70.

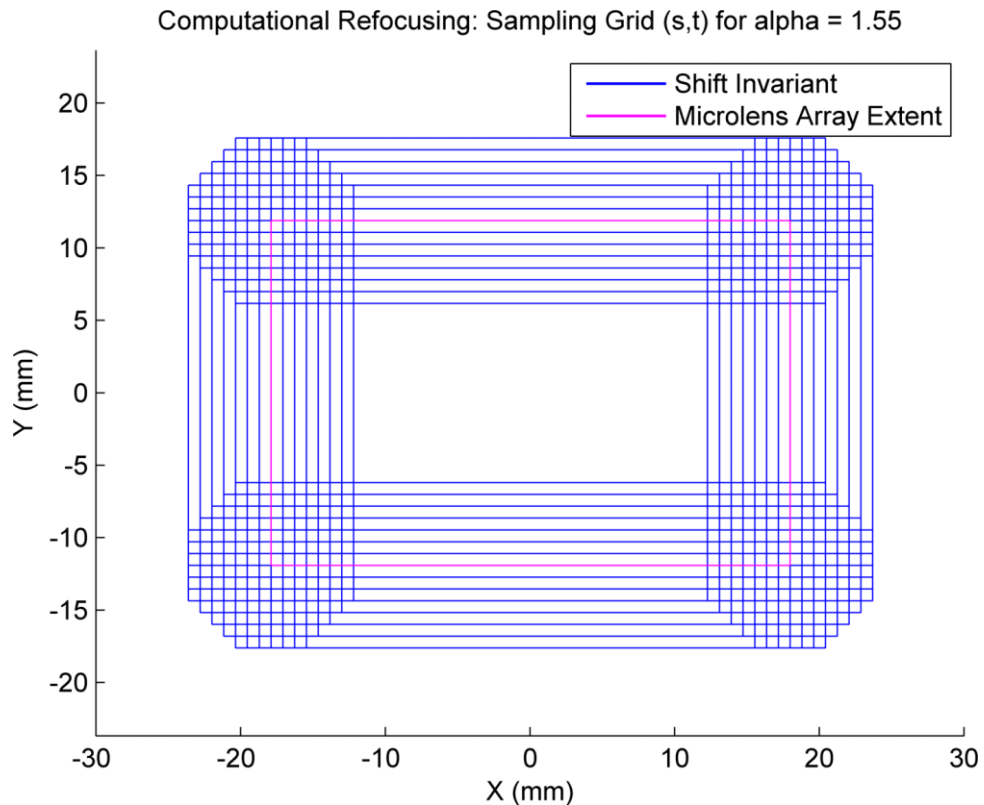
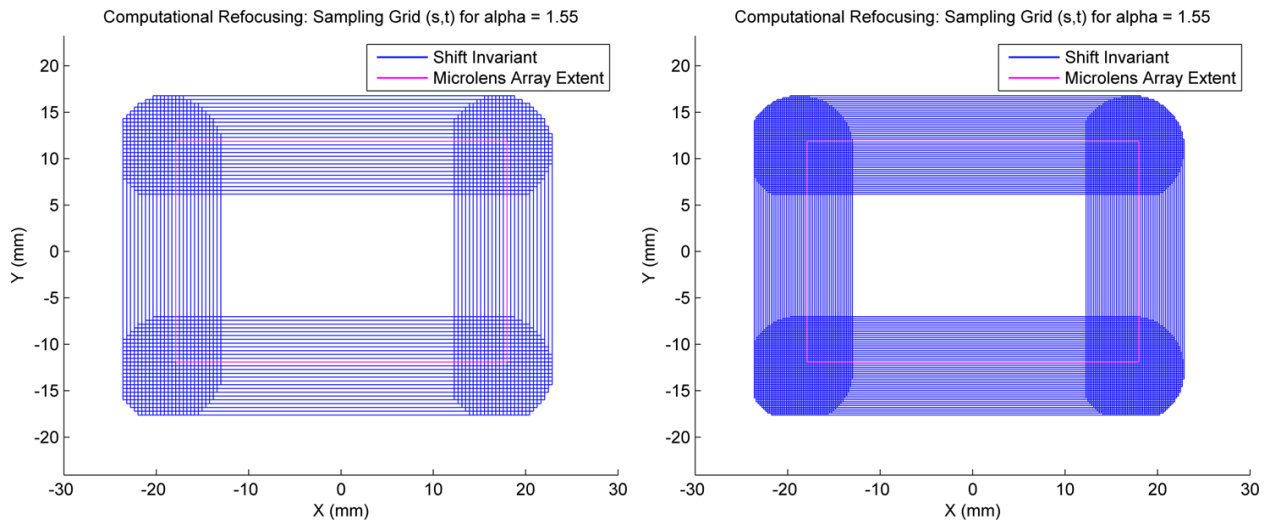


Figure 70: Effect of enforcing a circular aperture on (s,t) sampling grid used in refocusing

Recall that the rectangles represent the extent of the  $(s, t)$  sampling grid for each value of  $(u, v)$ . The magenta rectangle is the size of the microlens array. The edges of the sampling pattern are rounded off as the  $(u, v)$  values outside of the disk are not evaluated. This has the secondary benefit of increasing the speed of the refocusing algorithm in LFIT.

Supersampling in  $(u, v)$  serves to increase the number of locations at which the  $(s, t)$  sampling grid is evaluated in the refocusing algorithm. This can be seen in Figure 71 for two cases of increased  $(u, v)$  supersampling.



**Figure 71: Sampling grid for  $(s, t)$  with supersampling x2 (left) and x4 (right) in  $(u, v)$  with an enforced circular aperture**

On the left is a twice as dense  $(u, v)$  range, while the right plot is four times supersampled. Supersampling in  $(s, t)$  would increase the number of points in the  $(s, t)$  sampling grid. Although not plotted, this would lead to more points in the  $(s, t)$  grid, again whose extent is plotted with rectangles in these figures.

#### D. Further Supersampling Discussion and Examples

In practice, supersampling in  $(s, t)$  is performed on refocused images to reduce aliasing as discussed earlier. This creates a noticeable improvement in refocused images, especially when these images are enlarged or cropped. Supersampling in  $(u, v)$  angular coordinates has a more subtle effect on most images; it becomes most obvious when refocusing to new focal planes far off the nominal focal plane where the reduction in available  $(u, v)$  samples necessitates a higher sampling rate.

To demonstrate the power of supersampling, a sample plenoptic image of a scene in our lab was used for a qualitative comparison. This image was refocused to move the focal plane onto a Timex alarm clock in the foreground. The non-supersampled full image is given below in Figure 72.



**Figure 72: Sample refocused lab scene of clock (without supersampling)**

This image is 286 x 190 pixels in size. Cropping out the lower right portion of the clock and enlarging it, a comparison can be made between different amounts of supersampling. Two upscaled versions of the non-supersampled image are also included for comparison. These results are given in Figure 73.



1x (s,t), 1x (u,v)  
No additional scaling



1x (s,t), 1x (u,v)  
8x Bicubic upsampling (ImageJ)



1x (s,t), 1x (u,v)  
Resized in PowerPoint 2007



8x (s,t), 8x (u,v)  
No additional scaling

**Figure 73: Supersampling and upscaling qualitative comparison**

The non-supersampled case is shown at the top of the above figure where  $(u, v)$  and  $(s, t)$  are given with their native sampling. The next image shows the result of upscaling the image in ImageJ via an 8x Bicubic upsampling. The result is a definite improvement; the Timex logo is now legible, although some aliasing artifacts can be seen in the bend of the black band in the center-right of the clock.

On a whim, the non-supersampled image was simply scaled to a larger size using PowerPoint 2007. Surprisingly, the (unknown) interpolation algorithm in PowerPoint 2007 did an excellent job scaling the image to a larger size. The aliasing artifacts in the black band are no longer seen, and it is difficult to distinguish the scaled up PowerPoint image from a best case 8x

supersampling in  $(s, t)$  and  $(u, v)$  via LFIT. (As an aside, the upscaling algorithm in PowerPoint 2013 appears to have changed, yielding results comparable to the ImageJ based bicubic upsampling.)

The conclusion to draw from this discussion is that, as implemented in LFIT, the supersampling process does not appear to be increasing the spatial resolution of refocused images; rather, by reducing the SFR above Nyquist, aliasing is reduced such that previously corrupted features are now visible.